THESIS FOR THE DEGREE OF DOCTOR OF PHILOSOPHY

Synchrotron Imaging of Synthetic and Lignocellulose-based Packaging Materials

Linnea Björn

Department of Physics

CHALMERS UNIVERSITY OF TECHNOLOGY

Gothenburg, Sweden 2025

Synchrotron Imaging of Synthetic and Lignocellulose-based Packaging Materials
LINNEA BJÖRN
ISBN 978-91-8103-255-0

Doktorsavhandlingar vid Chalmers tekniska högskola
Ny serie 5713
ISSN 0346-718X

Department of Physics
Chalmers University of Technology
SE-412 96 Gothenburg
Sweden
Telephone + 46 (0)31-772 1000

Cover: Scanning small angle X-ray scattering image of paper-based drinking straws

Chalmers Digitaltryck
Gothenburg, Sweden 2025

Synchrotron imaging of synthetic and lignocellulose-based packaging materials

Linnea Björn
Department of Physics
Chalmers University of Technology

Abstract

The widespread success of polymer-based packaging materials is associated with having melt processability, which allows to create products with complex shapes at a low cost. However, the resulting polymer morphology is influenced by a combination of factors, including material properties, processing conditions, and environmental factors such as humidity. These structural variations directly impact the mechanical performance of the packaging material and consequently, understanding the correlation between material, processing parameters, and resulting morphology remains an important challenge. Furthermore, to expand the use of renewable cellulosic materials, intrinsic limitations in cellulose that impede melt processing must be overcome. This can be achieved by chemically modifying the cellulose, however chemical modifications impact the morphology formed during processing.

This thesis applies advanced X-ray based imaging techniques to investigate polymer based packaging materials, aiming to correlate their hierarchical structures with material performance. The thesis covers a diverse range of polymer materials, from conventional synthetic polymers to lignocellulose-based papers and chemically modified cellulose. In injection-molded polyethylene, scanning small and wide-angle X-ray scattering (SAXS/WAXS) combined with computational simulations was used to reveal a complex multilayered morphology with oriented structures near the sample edges. These organized structures were strongly influenced by material composition as well as local shear and cooling rates during the injection process and could be linked to enhanced mechanical strength (Papers I and II). In chemically modified cellulose, dialcohol cellulose is explored as a new path toward sustainable packaging, as it can be melt-processed both by itself and in composites with synthetic polymers. Scanning SAXS and WAXS showed that both degree of modification and processing conditions influenced the cellulose orientation, and that using humidity control during processing helps maintain favorable crystalline structures during processing (Papers III and IV). In non-modified cellulose fibers for drinking straw application, SAXS and WAXS demonstrated how liquid exposure and changes in relative humidity induced multiscale structural changes crucial for understanding the real-world performance of commercially available pulp materials (Paper V). Finally, the potential of using near-edge X-ray absorption fine-structure spectroscopy (NEXAFS) coupled with scanning transmission X-ray microscopy (STXM) was explored as a chemical imaging tool for fiber-based materials. Sample preparation strategies were shown to critically influence the quality of the measurement, influencing sample homogeneity, spectral quality and sensitivity to radiation damage (Paper VI). The combined findings of this work advance structural and chemical characterization of both fossil- and lignocellulose-based polymers, contributing to a deeper understanding of structure–property relationships critical for tailoring material performance in packaging applications.

Keywords: Packaging Materials, X-ray imaging, X-ray scattering, X-ray microscopy, Melt Processing, Polyethylene, Dialcohol cellulose, Pulp

List of Papers

This thesis is based on the following papers:

I Scanning Small-Angle X-ray Scattering of Injection-Molded Polymers: Anisotropic Structure and Mechanical Properties of Low-Density Polyethylene

Linnea Björn, Renan Melhado Mazza, Eskil Andreasson, Fredrik Linell, Viviane Lutz Bueno, Manuel Guizar-Sicairos, Elin Persson Jutemar, and Marianne Liebi
ACS Applied Polymer Materials (2023) 5(8): 6429-6440

II Process induced structures of Injection Molded High Density Polyethylene – combining X-ray Scattering and Finite Element Modeling

Linnea Björn, Elin Persson Jutemar, Renan Melhado Mazza, Eskil Andreasson, Fredrik Linell, Manuel Guizar-Sicairos, Marianne Liebi
ACS Applied Polymer Materials (2024), 6(8): 4852-4864.

III Melt processed materials of exceptionally high cellulose fiber content

Giada Lo Re, Emile R. Engel, Linnea Björn, Manuel Guizar Sicairos, Marianne Liebi, Jan Wahlberg, Katarina Jonasson, Per A. Larsson
Chemical Engineering Journal (2023), 458: 141372.

IV Using scanning small and wide angle X-ray scattering to investigate the effect of water during processing of modified cellulose

Linnea Björn, Katarina Jonasson, Enrica Pellegrino, Linnea Rensmo, Dimitra Athanasiadou, Manuel Guizar-Sicairos, Per Larsson, Giada Lo Re, Anette Larsson, Marianne Liebi
In manuscript

V Investigating the influence of moisture in paper-based materials using SAXS

Linnea Björn, Fredrik Olofsson, Eskil Andreasson, Elin Persson Jutemar, Joachim Kohlbrecher, Christian Appel, Kim Nygård, and Marianne Liebi
In manuscript

VI Sample preparation and measurement strategies for imaging cellulose fibers with carbon K-edge spectro-microscopy

Linnea Björn*, Martina Olsson*, Gunnar Westman, Agnieszka Ziolkowska, Jonathan Avaro, Benjamin Watts, Aleksandar Matic, Marianne Liebi
* Contributed equally
Submitted Manuscript

Contribution Report

I I led the synchrotron experiments and performed mechanical testing. I analyzed the scattering and mechanical testing data and was main responsible for writing the manuscript.

II I led the synchrotron experiments and performed the birefringence measurements. I analyzed the scattering data, and was main responsible for preparing the manuscript together with E.P.J.

III I led the synchrotron experiments, analyzed the data and wrote the corresponding paragraphs in the manuscript.

IV I led the synchrotron experiments, performed all data analysis and was main responsible for writing the manuscript.

V I led the synchrotron experiments performed data analysis together with F.O. I was main responsible for preparing the manuscript.

VI I prepared samples together with A.Z and performed the synchrotron experiments with M.O. Me and M.O performed all data analysis and co-wrote the manuscript.

List of Papers not included in the thesis

I Phase-separated polymer blends for controlled drug delivery by tuning morphology

M. Olsson, R. Storm, L. Björn, V. Lilja, L. Krupnik, Y. Chen, P. Naidjonoka, A. Diaz, M. Holler, B. Watts, A. Larsson, M. Liebi, A. Matic.
Communications Materials 5.1 (2024): 231

II Morphology and molecular mobility of plasticized lignins studied with polarization transfer solid-state NMR and SAXS

Åke Henrik-Klemens, Tobias Sparrman, Linnea Björn, Aleksandar Matic, Anette Larsson.
Polymer Testing 151 (2025): 108942

Table of Contents

Chapter 1– Introduction

Packaging materials are essential for maintaining quality, safety, and shelf life of foods and consumer goods. A widely used packaging material is paper board due to its low cost, printability and recyclability. However, it lacks effective moisture and gas barrier properties which limit its use for many food applications. In contrast, metal cans and glass bottles offer excellent barrier properties and recyclability but are heavy, energy demanding to produce, and costly to transport. As a result, there is a high demand for plastic packaging, driven by the exceptional material properties and versatility of polymer materials. They are lightweight, durable, chemically resistant, and easy to process into diverse shapes and forms[1-3]. Over recent decades, the shift from reusable to single-use packaging has further accelerated plastic consumption worldwide. However, this development comes at a significant environmental cost. Most plastics are derived from fossil fuels, and their production consumes significant resources and contributes to greenhouse gas emissions. At end-of-life, plastic packaging often escapes recycling systems, accumulates in landfills or natural ecosystems where it can persist for hundreds of years. According to estimates by Geyer et al.[4], if current trends in production and waste management continue, approximately 12,000 million metric tons of plastic waste could end up in landfills or the environment by 2050.

The most common polymer used for packaging is polyethylene[5], with an annual global production of approximately 90 million metric tons[6]. The widespread use of polyethylene is largely due to favorable processing characteristics, good barrier properties, high mechanical strength and low cost. However, since polyethylene is derived from non-renewable petroleum resources, it significantly contributes to the long-lived plastic waste and high carbon emissions. Therefore, there is an increasing interest in developing bio-based and biodegradable alternatives to reduce environmental impacts and promote circular material systems.

Cellulose presents a promising candidate to this transformation, since it is the most abundant biopolymer on Earth[7]. However, transforming cellulose into more versatile, three-dimensional packaging materials presents significant technical challenges. Most conventional processing methods of polymer materials such as injection molding or extrusion require the material to exhibit thermoplastic properties. Specifically, the material should become soft and amendable to molding upon heating or shearing and become rigid and retain the molded shape upon cooling. Native cellulose does not fulfill these requirements due to its high crystallinity and strong inter- and intramolecular interactions. In contrast to fossil-based thermoplastics, cellulose decomposes before it reaches a flowable state, as the thermal degradation temperature lies below its glass transition and melting

points. In order for cellulose to exhibit thermoplastic properties, it needs to be chemically modified. Such modifications often destroy the inherent cellulose nanostructure and require energy-demanding procedures and large volumes of chemicals or solvents[8-10].

Both fossil-based and bio-based polymers exhibit complex hierarchical structures, where smaller subunits self-organize across multiple length scales to form larger structural architectures. In conventional polymers such as polyethylene, this hierarchy typically includes both crystalline and amorphous phases, giving rise to a semicrystalline morphology. Crystalline regions are formed by ordered folding and stacking of polymer chains, while the amorphous regions consist of randomly entangled chains without long-range order[11]. These domains can further organize into larger structures such as spherulites and shish-kebabs, which is important for the mechanical properties exhibited. Spherulites are approximately spherical aggregates of crystallites, whereas the shish-kebab structure features an aligned crystalline core surrounded by perpendicular lamellae[12]. In cellulose-based materials the structural complexity is even greater. In lignocellulosic biomass such as wood, cellulose is intertwined with lignin and hemicellulose, which results in a multicomponent hierarchical material. The cellulose chains are organized into microfibrils and microfibril bundles that build up a multilayered cell wall of the fiber[13, 14]. Chemical modification adds further complexity, affecting both the nanoscale arrangement and processability.

Understanding and characterizing the complex structures of polymer materials and their relationship to material properties remain critical challenges for both fossil-based and cellulose-derived materials. The micro- and nanoscale morphology of a polymers is influenced by a wide range of factors including the chemical nature of the polymer as well as processing conditions and storage conditions. Small changes in molecular parameters such as molecular weight distribution, degree of branching, or the presence of additives and fillers can lead to significant differences in the resulting morphology. In the case of chemically modified cellulose, the degree and type of modification play an important role in determining processability and structural organization. Furthermore, the processing conditions, such as temperature, shear rate, and cooling speed influence the polymer structures. For cellulose-based systems, ambient humidity both during and after processing is another critical factor that influences inter-fibril interactions and swelling behavior. The correlation between all these parameters creates a highly complex system, and many fundamental structure–processing–property relationships remain poorly understood.

To address this issue, advanced characterization techniques are essential. Among these, small- and wide-angle X-ray scattering (SAXS and WAXS) are particularly powerful tools as they enable non-destructive investigations of polymer structures across multiple length scales, from molecular arrangements to aggregate structures. In addition, scanning transmission X-ray microscopy (STXM) using near-edge X-ray absorption fine structure (NEXAFS) has high potential since it provides chemical specific contrast with high spatial resolution, making it especially valuable in chemically modified cellulose where small chemical differences can significantly alter the morphology and the material performance.

These methods are most effective when used in combination with complementary techniques. For instance, optical- and birefringence light microscopy can be used to visualize structural domains in the micrometer regime, mechanical testing can be used to link structures to material performance, and computational modeling can be used to simulate structure formation or predict material behavior. By integrating complementary approaches, it becomes possible to construct a more comprehensive understanding of polymer structures and functions.

In this thesis, hierarchical structures from the Angstrom regime to the millimeter scale of fossil- and bio-based polymers have been investigated using advanced X-ray based imaging techniques in combination with complementary techniques. The work includes a systematic study of a commercially used polyethylene, examining how varying densities, molecular weights, and process conditions influence polymer hierarchical structures and mechanical performance. The experimental findings are further compared with computational simulations to explore the underlying mechanisms for the anisotropic morphologies. In future work, these results could be used to calibrate simulation models and predict material performance without the need for physical tests of each prototype with varying complex shapes and materials.

In parallel, chemically modified cellulose, specifically dialcohol cellulose, is explored as a bio-based material that demonstrates thermoplastic properties. Dialcohol cellulose is studied as part of a composite with a synthetic polymer, with a focus on how the degree of chemical modification and material composition influence structural organization throughout the material. Understanding these structure–composition relationships is crucial for tailoring material properties in future bio-based packaging applications. Dialcohol cellulose is further studied as a standalone material to examine the effects of processing, particularly the introduction of controlled humidity during processing. These findings are important for overcoming current limitations in the thermoplastic processing of cellulose.

Finally, this thesis explores the potential of scanning transmission X-ray microscopy (STXM) as a high-resolution tool for chemical characterization of cellulose fibers. The presented study investigates how different sample preparation strategies affect the resulting data quality and interpretability. Establishing reliable and reproducible STXM protocols is key to unlocking STXM's full potential in evaluating chemically heterogeneous fiber materials. Together, these studies contribute to a deeper understanding of polymer structure–property relationships, laying groundwork for the development and implementation of next-generation sustainable packaging materials.

Chapter 2 – Polymers

Polymers are widely used as packaging materials due to their remarkable mechanical, thermal, and solvent-resistant properties as well as easy molding and shaping[15]. A polymer is defined as a large molecule that forms long chains made up of covalently bonded repeating units called monomers, where the degree of polymerization is the number of monomeric units in the polymer. The properties of a polymer material vary greatly with the polymer type, structure and processing

In polymer materials, molecular ordering can occur when sufficiently long polymer chains fold back on themselves, forming crystalline regions known as lamellae[16]. The lamellae are typically embedded in an amorphous matrix, resulting in a two-phase morphology. The lamellae thickness is a characteristic length in polymer materials, and it highly impacts material properties such as stiffness, melting temperature and permeability.

For crystallization of a polymer to take place, the Gibbs free energy, G, must be negative

$$G = H - TS \qquad Equation\ 2.1$$

where H is enthalpy, S is entropy and T is temperature. The crystallization process results in a large negative entropy change since the molecular order of the polymer chains increases. Thereby, for Gibbs free energy to be negative, there must be a matching negative enthalpy change, which implies that strong interactions between polymer chains are necessary for crystallization to take place. Linear polymer chains allow for the polymers to pack closely, which increases the interaction between the chains. Thus, linear polymers are more prone to form crystals, compared to branched polymers with many defects incorporated into the polymer chain.

The folded surface is associated with large interfacial energy, which would thermodynamically favor thick lamellae crystals. However, due to kinetic limitations, polymers are found to form lamellae with a thickness typically in the range of tens of nanometers. The larger number of folds increase the free energy but make crystallization more kinetically accessible[17]. The thickness of the crystalline lamellae is highly dependent on the temperature of the melt at which the crystallization takes place[18]. Individual polymer chains may be involved in several crystalline lamellae as well as the amorphous regions in-between[19]. In a similar way, the crystalline lamellae often consist of multiple polymer chains, resulting in a complex intertwined network structure[20].

In natural sources like wood, polymer crystallization primarily involves cellulose, while lignin typically exists in an amorphous state. Cellulose is a key component to the structural integrity of wood, and the cellulose chains primarily orient themselves in the growing

direction of the tree. For man-made polymers, crystallization can be induced in varying processing conditions. If polymer crystallization takes place in a melt under quiescent conditions, crystallites tend to grow in a random fashion resulting in a state with low degree of molecular orientation, a morphology generally referred to as spherulites. In contrast, if the polymer chains are subjected to either a shear or an elongational flow, alignment of the molecular chains can be achieved[21]. The ordering of crystalline polymers is of high importance, since it imparts high material strength and rigidity with a direction dependent response due to the predominant crystal alignment[22].

2.1 Polyethylene

Polyethylene is one of the most widely used polymers due to its low production cost, ease of modification and relatively low carbon footprint compared to other synthetic plastics[23, 24]. From a chemical point of view, polyethylene is one of the simplest polymers since it consists of repeating units of methylene. However, from a structural point of view the structure is often complex. The most common crystalline state of polyethylene is packing of unbranched parts of the polymer chains into an orthorhombic unit cell, with amorphous regions in-between the crystalline parts[25, 26]. If crystallization occurs in a melt at rest, the lamellae of polyethylene grows around central nucleolus resulting in an isotropic crystal structure called spherulites[27]. If crystallization instead takes place at intermediate shear, the spherulites elongate in the direction of the flow, adapting to more or less elliptical shapes[12, 28]. At high shear, a so called shish-kebab morphology can be formed where polymer chains are stretched out in the direction of the flow creating highly oriented thread-like structures (shish) with crystalline lamellae (kebabs) growing in the perpendicular direction[29, 30]. Figure 2.1 shows schematic representations as well as microscopy images of the spherulite and shish-kebab microstructure. The spherulite structure is associated with isotropic mechanical properties[31], whereas the shish-kebab structure gives highly anisotropic properties where the tensile strength is improved and the elongation at break is decreased in the direction of the oriented shish[32, 33]. The shish-kebab structure is more prone to form when the cooling rates are high[34], and it has been reported to have two different morphologies with twisted and untwisted lamellae[30, 35].

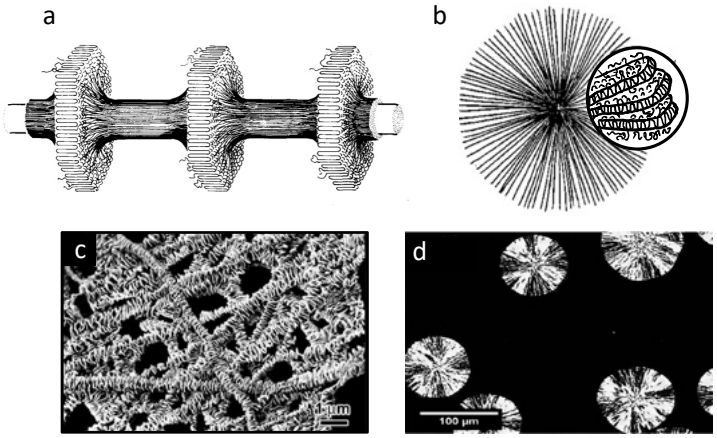

Figure 2.1. Examples of semicrystalline morphologies of polyethylene. Figure 2.1a and 2.1b show schematic representation of the shish-kebab and spherulite microstructure respectively, Figure 2.1c shows micrographs of the shish-kebab structure taken with field-emission scanning emission microscopy, and Figure 2.1d shows polarized optical microscopy images of a spherulite microstructure. Adapted with permission from Katti et al[12] (Copyright 2004, John Wiley & Sons), Somani et al.[36] (Copyright 2005, Elsevier) and Tong et al.[37] (Copyright 2015, Elsevier).

2.2 Lignocellulose-based Polymers

Lignocellulose-based polymers can be derived from numerous sources, such as wood, agricultural waste[38], and oil palm biomass residue[39], making them abundant materials with significant potential for sustainable development.

2.2.1 Wood Fibers

Wood plant cells, also known as wood fibers, make up the structural framework of wood. The length and size of wood fibers varies depending on the plant source, location in the tree and growth cycle. For example, Scandinavian softwood fibers are typically 2–4 mm long and 30 µm wide[40]. The three main components in the wood fiber are cellulose, hemicellulose and lignin. The wood fiber consists of a cell wall that surrounds a hollow center known as a lumen, as shown in Figure 2.2. In the living tree, the lumen is mainly used for transportation of water and nutrients. The cell wall is a multilayered structure which is typically divided into a primary and a secondary cell wall. The secondary cell wall can further be divided into three layers, S1, S2 and S3. The primary wall consists of hemicellulose, pectins, proteins and disordered cellulose microfibrils[31]. This layer is flexible and allows the cell to expand during growth. The secondary cell wall is in contrast much stiffer and gives the wood fiber high mechanical strength and contains more cellulose and lignin compared to the primary cell wall. The S2 layer is the thickest and most important layer in terms of mechanical properties. It consists of cellulose microfibrils that are arranged helically with a 5-30° angle with respect to the fiber axis,

contributing to the high mechanical strength[41, 42]. The fibers are joined together by the middle lamellae, which is a thin lignin rich layer with a thickness of 0.2–1.0 μm[43].

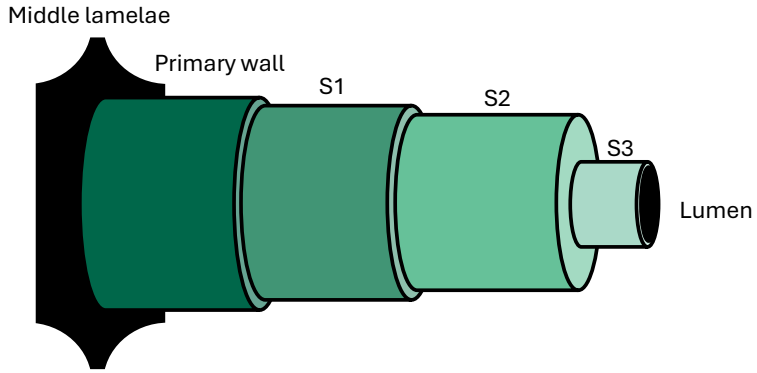

Figure 2.2. Simplified structure of a wood cell, showing the hollow lumen, the primary wall (P), outer (S1), middle (S2) and inner (S3) layer of the secondary wall and the middle lamellae (ML). Adapted from Sjöström et al.[42].

2.2.2 Cellulose

Cellulose is a crucial component in plant cell walls to maintain strength and rigidity. The structure of native cellulose is highly hierarchical and complex, as shown in Figure 2.3, where the sizes and distribution of the components can differ depending on the plant species and environmental influences[44].

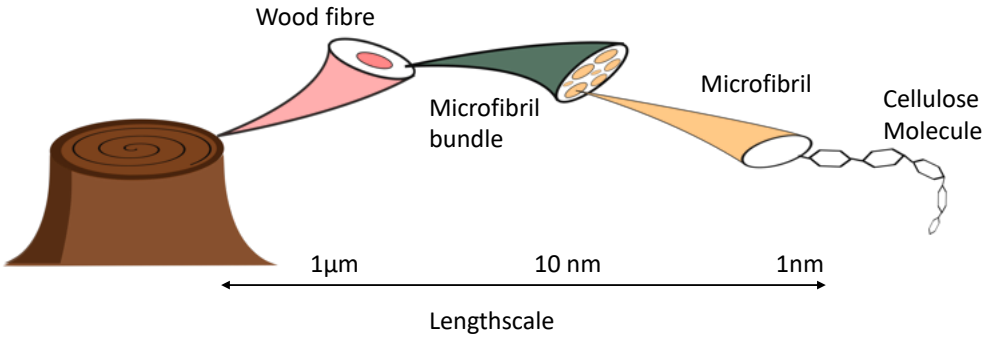

Figure 2.3. The hierarchical structures of wood. Inspiration from Penttilä[45]

On the molecular level, cellulose is a linear polymer composed of glucose[46], where the molecular structure of cellulose can be seen in Figure 2.4 a) (i). Depending on the plant source, the degree of polymerization of cellulose is approximately 14,000 in its native state[41]. In similarity to other polymers, cellulose is a semicrystalline material forming both amorphous and crystalline regions, where the cellulose chains stack together with intramolecular hydrogen and van der Waals bonds to form the crystalline regions. The assembly of cellulose chains form structures called microfibrils, which have an approximate diameter of 2-20 nm and an approximate length of 0.1-40 μm[47]. The fibrils exhibit high

strength and are therefore considered to be reinforcement components of the wood fibers[48]. The microfibrils further aggregate to microfibril bundles, which are parts of the wood fibers.

2.2.3 Pulp

To utilize cellulose or lignocellulosic fibers in material applications, they must first be separated from the surrounding structural environment. This is typically achieved through pulping, where mechanical or chemical treatments are used to extract fibers or cellulose from the lignocellulosic biomass[49]. Pulping can be done in different ways, which can be categorized into either mechanical, chemical and semi-mechanical pulping[50]. Mechanical pulping is in general associated with lower production costs and less pollutants, whereas chemical pulping typically produces pulp with higher strength and requires less energy.
A commonly used mechanical pulping process is thermomechanical pulp (TMP). In the TMP process, wood chips are fed into a large steam-heated refiner where the wood chips are mechanically grinded between two steel disks under elevated temperature and pressure. As its name implies, heat and mechanical energy are used to transform the wood structure into a pulped material[51]. The lignin and hemicellulose are not removed from the pulp in the TMP process, which gives a high yield (up to 95%). On the downside, the harsh mechanical processing often gives reduced fiber lengths, resulting in a pulp with relatively low strength.
A chemical pulping method frequently used is the Kraft process, where wood chips are mixed with sodium hydroxide and sodium sulfite to break the chemical bonds between lignin and cellulose. The lignin is then washed from the cellulose fibers, creating a pulp free from lignin[51].

2.2.4 Dialcohol Cellulose fibers

Cellulose is not intrinsically thermoplastic and in order to use it in conventional processing techniques like injection molding or extrusion, modification of the cellulose structure is needed. A promising cellulose modification is dialcohol cellulose, since this material has been shown to exhibit thermoplastic properties in terms of softening, increased ductility, and melt processability[52]. To produce dialcohol cellulose, a two-step modification is used, where the first step is periodate oxidation and the second step is borohydride reduction (Figure 2.4a). The suggested structure for the heterogeneously modified dialcohol cellulose is a core-shell structure, with amorphous dialcohol cellulose as a shell around a core of more crystalline cellulose as shown in Figure 2.4b. One hypothesis is that thermoplastic properties are achieved from a combination of surface modification enhancing the fiber-fiber interface, and internal modification making the fiber more flexible.

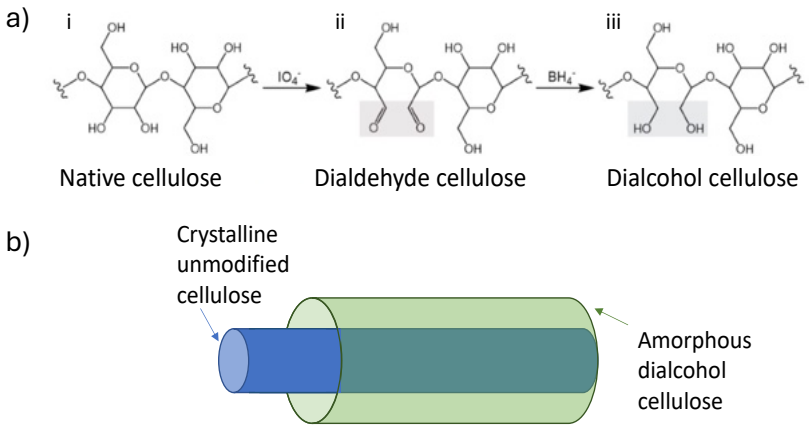

Figure 2.4. Structure of dialcohol cellulose where a) shows the reaction scheme and b) shows schematic representation of the fibril structure of dialcohol cellulose. The core consists of crystalline cellulose and the surface consists of amorphous dialcohol cellulose.

2.3 Polymer Processing

Polymer processing makes it possible to convert raw materials of different polymer compounds, blends or composites into functional products. Polymer processing is a wide term that can refer to a range of techniques including extrusion, injection molding, blow molding, thermoforming and more. In the case of thermoplastic processing, the key steps typically include plasticization of the solid polymer, flow and shaping of the melt, and cooling and solidification of the polymer[53]. In this thesis, samples were produced with micro compounding and injection molding.

2.3.1 Micro Compounding

Micro compounders are widely used in research and development for small-scale polymer processing. These instruments are specialized miniaturized extruders designed for mixing, blending and modification of polymeric materials. In large scale industry, extruders are widely used, however conventional extruders are not suitable for small sample quantities. Micro compounding is based on the same working principle as regular extruders, using two rotating screws within a barrel to mix and process polymer materials[54]. In contrast to a regular extruder, the micro compounder couples the rotating screws with a recirculation channel[55].

This setup allows the material to circulate through the screw zone multiple times, ensuring adequate thermomechanical treatment that is essential for melting, mixing, and homogenization of the material. Therefore, micro compounders are particularly beneficial

when studying shear-sensitive materials, as the continuous flow mimics the processing conditions found in industrial-scale extruders.

2.3.2 Injection Molding

Injection molding is a widely used processing technique for polymers that has been continually developed over almost 150 years[56] and over 30% of all plastic parts are manufactured with injection molding[57]. In the injection molding process, plastic pellets are fed into the injection molding machine and heated until the polymer is soft enough to be injected into a mold under pressure. This creates a complex flow pattern called fountain flow (Figure 2.5) with varying shear and cooling rates in the through-thickness direction, highly influencing the hierarchical semicrystalline structure of the polymer. Several studies have been published investigating how various processing conditions influence the polymer morphologies, such as pressure[58, 59], shear rate[60] cooling rate[61] and stress overshoot[62]. Katti et al[12] described that close to the injection molded gate the flow has a semicircular shape mainly dominated by an elongational flow, whereas further down the plate the flow is laminar instead. Thus, it is expected that the polymer morphology depends both on the position in the thickness direction and the distance from the injection molded gate.

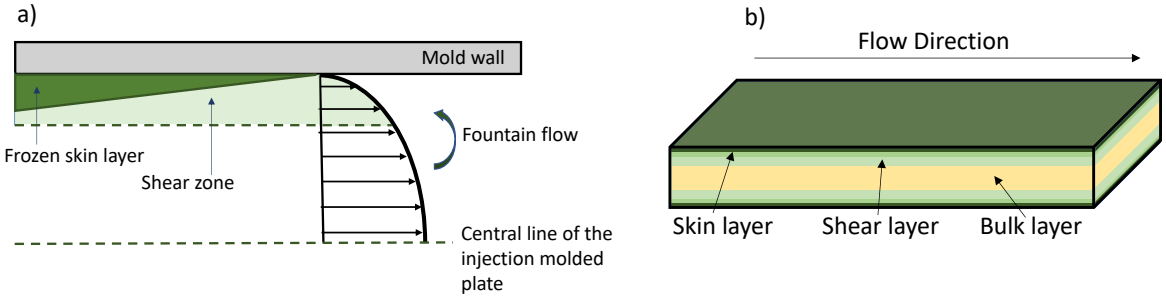

Figure 2.5. Multilayered structure of injection molded polymers, where a) shows the shear rate profile of the fountain flow inspired by Zhou et al. [63], and b) shows the characteristic layers of an injection molded plate.

The injection molded process can be divided into four stages[64]. First is the filling phase where the molten polymer is injected into the cool mold under pressure. Second is the packing phase, where high pressure is maintained and additional melt flows into the cavity to prevent shrinkage under solidification. Third comes the cooling phase where the polymer is allowed to cool down to room temperature. Fourth is the ejection, where the polymer is removed from the injection molding machine. A schematic representation of volume flow rate, pressure, temperature, and crystallization progress can be seen in Figure 2.6.

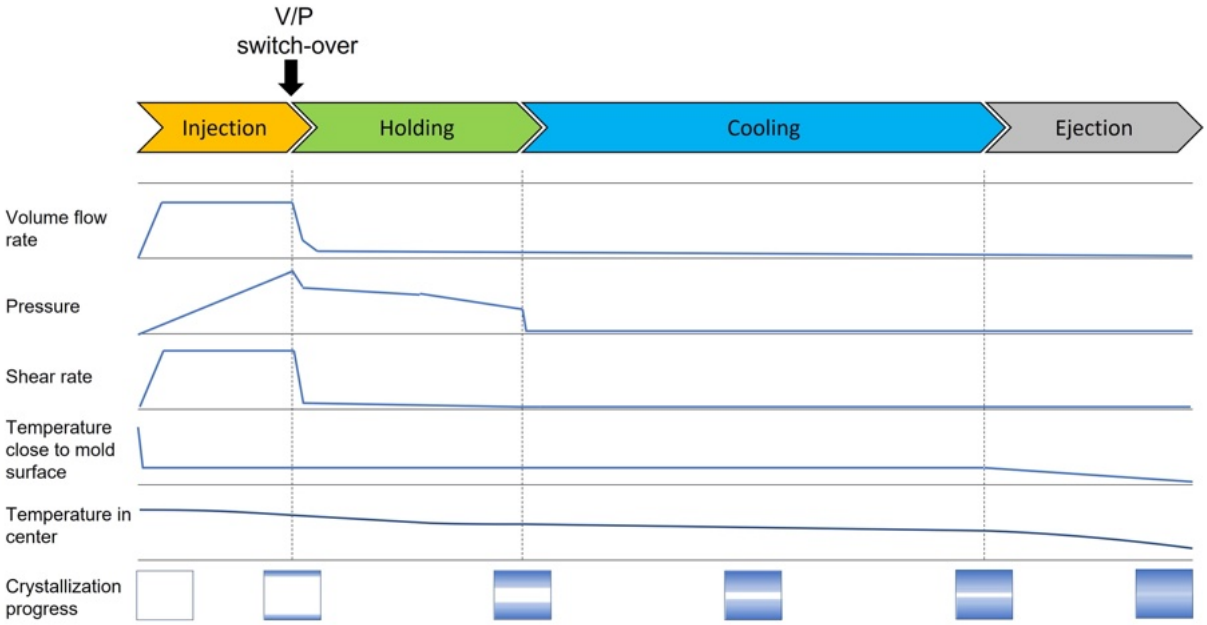

Figure 2.6. Schematic representation of the different phases during injection molding.

2.4 Polymers for packaging applications

In packaging applications, there are many requirements on the material properties. The processability is of high importance, as well as mechanical properties, barrier properties, permeability and recyclability. The overall performance of a packaging product is dictated by a complex interplay between the intrinsic properties of the materials and the conditions under which the product is processed. As a result, accurately predicting the performance of packaging materials remains a significant challenge.

Polymers used in packaging applications are typically derived from either fossil-based sources, such as polyethylene, polypropylene, polyethylene terephthalate (PET), or renewable sources such as cellulose or starch[65]. Fossil-based or synthetic polymers dominate the market today due to their excellent mechanical performance, barrier properties and low price. Furthermore, they exhibit excellent thermoplastic processability, and conventional processing techniques have been used and optimized for synthetic polymers over decades. In particular, injection molding is commonly employed for synthetic polymer materials, since it can produce products with complex 3D shapes with high precision and repeatability. However, the morphology of the resulting polymer structure can vary significantly throughout an injection-molded part due to local differences in shear flow and cooling rates during and after processing. These morphological variations directly impact the mechanical and barrier properties. Therefore, understanding how processing conditions influence microstructure is essential for optimizing product performance.

In recent years, there has been a growing demand for more sustainable and environmentally friendly alternatives for packaging materials. As a response, attention has been directed

toward cellulose-based polymers, which offer the potential for enhanced recyclability, biodegradability, and lower carbon footprint compared to their fossil-based counterparts. In addition, regulatory measures such as the European Commission's ban of fossil-based materials for single use products have further accelerated this trend[66].

Processing of cellulose-based materials is more challenging compared to processing of synthetic polymers since native cellulose does not exhibit thermoplastic properties[67-69]. To overcome this limitation and enable thermal shaping of cellulose, various chemical modifications have been explored including cellulose acetate, ethyl cellulose, methyl cellulose, and dialcohol cellulose[52, 70-73]. This opens new possibilities to explore cellulose-based materials for 3D-products, potentially broaden the application of cellulose in packaging applications. However, cellulose-based materials behave very differently compared to synthetic polymers and many aspects of their processing–structure–property relationships remain underexplored. Conventional processing routes, optimized for synthetic polymers, often lead to suboptimal outcomes when applied directly to cellulose-based materials. This is exemplified in Figure 2.7, where scanning SAXS was used to investigate the hierarchical structures in a paper-based material used for drinking straws. The figure shows two types of paper-based drinking straws produced with different types of corrugation patterns to allow for bending of the straw. The top straw was produced with a traditional corrugation pattern that was developed and optimized for synthetic polymers, whereas the bottom straw was developed with a new type of corrugation pattern with cellulose-based materials in mind. The Figure shows the scattering intensity in the low-q region, where the top straw displays an overall higher intensity across the corrugation pattern compared to the straw on the bottom. In this region, a high scattering intensity can be linked to an increase in the number of internal interfaces inside the material. Thus, a high scattering intensity indicates breakage of fibers, limiting the performance of the drinking straw. The example highlights the importance of adapting the processing routes to fit the new emerging cellulose-based materials. Note that at the edges of the samples, the high scattering stems from cutting effects from the sample preparation.

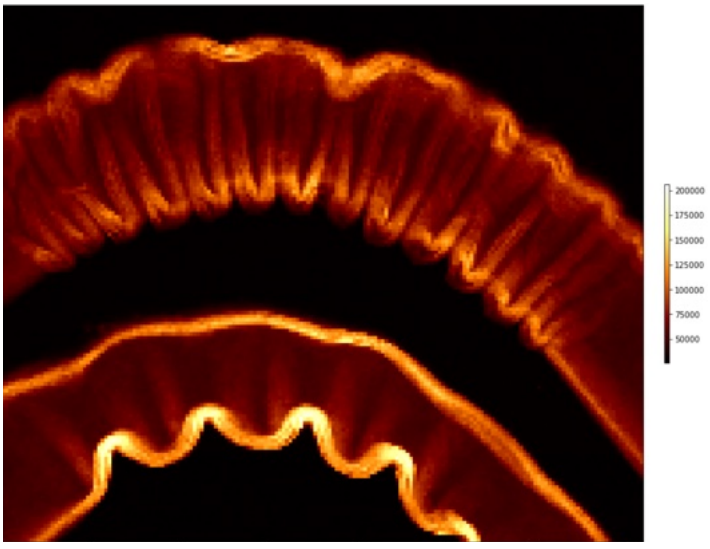

Figure 2.7. Scanning SAXS of commercial drinking straw with different corrugation patterns.

To understand the correlation between polymer morphology, processing and resulting performance, various characterization techniques can be used to probe the polymer material. For instance, optical microscopy can be used to visualize polymer structures in injection molded parts[74, 75]. Several previous studies have also been using small- and wide angle X-ray scattering (SAXS/WAXS)[76], often in combination with other techniques such as scanning electron microscopy (SEM)[77], differential scanning calorimetry (DSC)[78], and mechanical testing[34, 52], or a combination of them[79], in order to get in-depth understanding of the hierarchical structures processed polymer materials.

When investigating the processing–structure–property relationship of polymer materials, one of the most common strategies is to use a trial-and-error approach. In this approach, parameters are systematically varied, and the resulting material morphology or other material properties are tested. However, during processing of polymer materials there is a large amount of parameters that will influence the outcome, such as pressure[58, 59], shear rate [60], cooling rate[61 80], and stress overshoot[62, 81]. Furthermore, material variables also highly influence the outcome, for example small variances in molecular weight and molecular weight distribution[82-84]. Thus, the trial-and-error approach is often demanding and expensive and it is difficult to predict material properties for new packaging products, if the new product requires a different shape, material or processing conditions.

Computational simulation has the potential to predict package performance without the need for physical tests of each prototype, allowing for a prompt implementation of novel materials into the processing pipeline. Various studies have previously used computational models to simulate polymer processing for synthetic polymers, providing a better understanding of how processing conditions influence the resulting material performance[85-88]. For cellulose-based materials, the development of robust simulation tools is still in its early stages. Current modeling efforts focus mainly on material property predictions rather than simulating complex flow conditions. For example, molecular dynamics simulations have been used to evaluate dialcohol cellulose, suggesting that it has high molecular mobility at elevated temperatures, along with excellent stiffness and strength at room temperature[89, 90]. While computational simulations have high potential to predict material performance for packaging applications for both synthetic and cellulose-based polymers, the simulation models rely on accurate assumptions and input values for the material structures. However, most previous work is based on isotropic polymer morphologies, limiting the accuracy and use of the simulation output. Furthermore, linking simulation models to results from experimental characterization remains challenging due to the large quantity of fitting parameters.

Chapter 3 – X-ray based characterization

3.1 X-ray interaction with matter

X-rays are electromagnetic waves with wavelengths between 0.01-10 nanometers, which correspond to photon energies between 100 eV to 100 keV[91]. Due to the high energy, X-rays have high penetration power, making them ideal for non-destructive material characterization techniques. When X-rays interact with matter, they interact with the electrons of atoms in two predominant ways, scattering and absorption. Figure 3.1 illustrates the interactions between X-rays and electrons.

Scattering occurs when the direction of the X-ray beam is changed due to interactions with electrons. If the energy of the scattered X-rays remains unchanged, the process is known as elastic scattering (Thomson or Rayleigh scattering). During elastic scattering, the X-rays cause electrons to oscillate at the frequency of the incident beam. These oscillations cause the electrons to emit photons at the same wavelength, and the interference between the scattered waves can be constructive or destructive depending on their relative phase, see path b in Figure 3.1. This type of scattering is central to techniques like SAXS and WAXS. If there is an energy transfer between the X-ray photons and the electrons the process is known as inelastic scattering (Compton scattering), resulting in a photon with lower energy (path c in Figure 3.1). For most applications using synchrotron radiation at energies below 100 keV, the effects of Compton scattering are small and neglected[91, 92].

X-ray absorption, on the other hand, involves complete absorption of an X-ray photon by an atom, transferring its energy to an inner-shell electron (path a in Figure 3.1). This energy absorption causes the electron to be ejected from the atom, a process known as the photoelectric effect. The vacancy in the electron shell is filled by an electron from a higher energy level, where the excess energy will be released either as a photon with characteristic wavelength, i.e. X-ray fluorescence or transferred to another electron, which is ejected as an Auger electron. This principle is fundamental to techniques such as X-ray fluorescence (XRF) and Near edge x-ray absorption fine structure (NEXAFS)[91].

When X-rays pass through matter, the intensity I of the transmitted X-rays will decrease due to these interactions. The attenuation can be described by the Beer-Lambert law:

$$I = I_0 e^{-\mu x} \qquad Equation\ 3.1$$

Where I_0 is the initial X-ray intensity, μ is the linear attenuation coefficient, and x is the path length through the material. The attenuation coefficient depends on the material composition and X-ray energy and decreases with increasing X-ray energy and atomic number and increases with increasing density of the material[93].

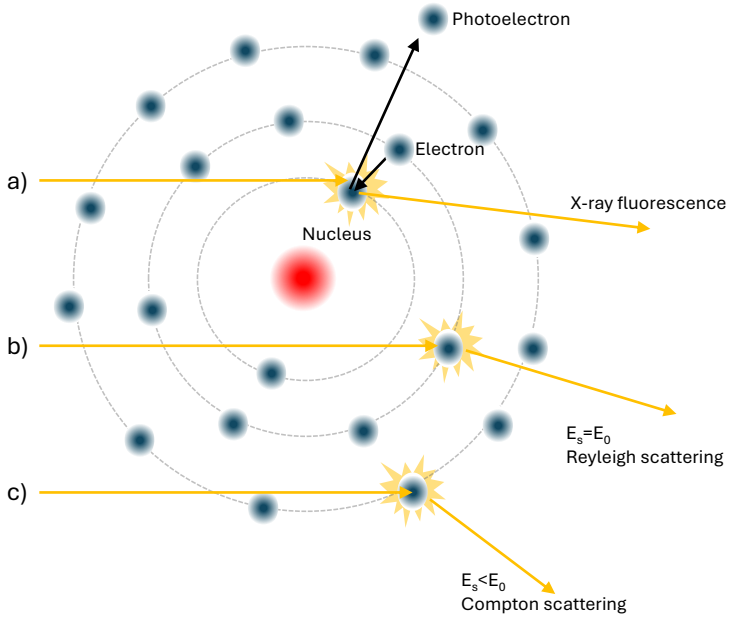

Figure 3.1. Illustration of X-ray interaction with matter, where E_0 corresponds to the energy of the incoming X-ray photon, E_s corresponds to the energy of the scattered X-ray photon. Path a) corresponds to the photoelectric effect path b) to the Rayleigh scattering and path c) to Compton scattering.

3.2 Synchrotron radiation

Synchrotrons are circular particle accelerators that are used to produce high-intensity X-rays and other forms of electromagnetic radiation. This radiation is characterized by extremely high brightness, tunable energy, and naturally narrow collimation. These properties make synchrotron radiation an essential tool for characterizing materials across a broad range of scientific and industrial applications.

In a synchrotron, electrons are first generated by an electron gun and accelerated and focused through a sequence of magnets inside a linear accelerator (LINAC). Depending on the synchrotron design, the accelerated electrons may be injected directly into the storage ring (as at MAX IV) or first into a booster ring, which increases their energy before injection into the storage ring (as at the Swiss Light Source, SLS). In the storage ring, the electrons travel around a curved path at near the speed of light, and different types of insertion devices are used to manipulate the direction of the electron beam to produce radiation with varying properties. Bending magnets are used to steer the electron beam along the curved path of the storage ring and resulting in continuous spectrum of radiation tangentially to the beam's circular path. Wigglers consist of a series of alternating-pole magnets that cause the electrons to oscillate rapidly from side to side. This produces intense, continuous

spectrum radiation with higher brightness compared to bending magnets due to the constructive addition of radiation from multiple oscillations. Undulators have a similar structure to wigglers but have a lower magnetic field strength and smaller angular deviation, which produces monochromatic radiation due to constructive interference. Undulators offer very high brilliance and are ideal for techniques requiring narrow energy bandwidths, such as X-ray absorption spectroscopy[91, 94].

The radiation produced by the insertion devices is directed into beamlines, which serve as the experimental stations of the synchrotron facility. Each beamline is designed for a particular type of measurement or technique and is equipped with optical components such as monochromators, focusing optics, slits, and high-resolution detectors[94]. Figure 3.2 shows examples of beamline layouts from the cSAXS and the PolLux beamline at the Swiss Light Source, Paul Scherrer Institute.

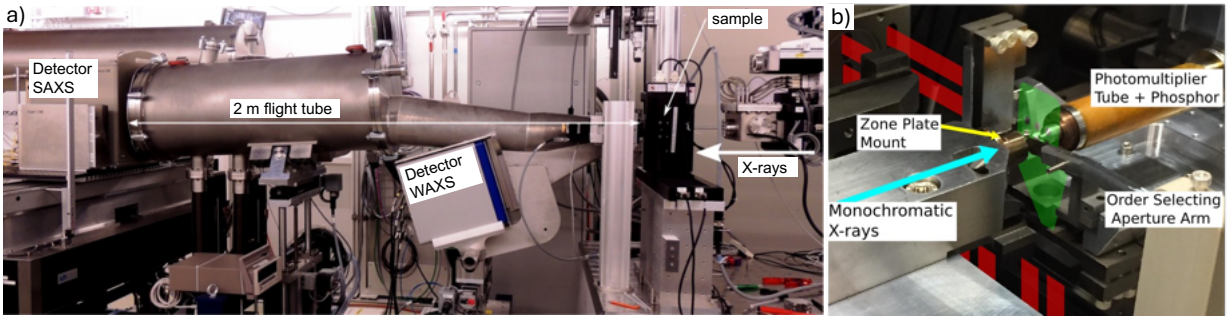

Figure 3.2. Examples of different beamline layouts where a) shows the cSAXS beamline and b) shows the PolLux beamline at SLS, PSI.

Compared to conventional laboratory X-ray sources, there are many advantages to using synchrotron radiation. The high photon flux and brilliance enable extremely fast data acquisition, making time-resolved experiments possible. Furthermore, the synchrotron beam can be highly focused, allowing for spatially resolved measurements. The photon energy can be finely tuned over a wide energy range, which makes it possible to probe specific elements or chemical compounds. Another key advantage is that synchrotron facilities support a wide range of experimental environments, such as mechanical testing stages, humidity control and chemical reactors, allowing for in-situ and operando measurements.

3.3 Near edge X-ray absorption fine structure

Near edge X-ray absorption fine structure (NEXAFS) is a technique to extract chemical information about a sample, where the absorption is detected as a function of energy. During a NEXAFS measurement, a specific atom species is selected, and the X-ray energy is scanned across the corresponding absorption edge with high energy resolution. Due to interactions between core electrons and their local environment, the absorption energy needed to excite the electrons to an unoccupied energy state is slightly shifted[95]. This makes

it possible to detect the presence of specific chemical bonds in molecules, for instance can C-C be distinguished from C=C[96]. Due to having a unique electron structure, each chemical compound has a unique absorption spectrum.

The high energy resolution in NEXAFS can be combined with a high spatial resolution in scanning transmission X-ray microscopy (STXM). In this setup, in particular for soft X-rays, Fresnel zone plates are commonly utilized to focus the x-rays to a point focus on the sample and a detector is placed behind the sample to measure the transmitted intensity[97]. Raster scanning is used to scan the sample through the focal point, and the transmitted intensity is recorded for each measurement point. After the measurement, the transmitted X-ray flux (I) can be transformed into optical density (OD) according to the Beer-Lambert law,

$$OD = -ln\frac{I}{I_0} \qquad Equation\ 3.2$$

Where I_0 is the incident X-ray flux[98]. In order to achieve high quality of the transmitted signal, the sample thickness is of high importance. The sample needs to be thin enough to allow sufficient X-ray transmission for detection, but thick enough to provide a measurable signal. The transparency of a sample varies strongly with the X-ray energy, where an increased X-ray energy in general corresponds to a decreased X-ray absorption. Cellulose-based samples are typically prepared with a thickness of 90-200 nm.

Figure 3.3 shows an example of a NEXAFS spectrum over the carbon K-edge of a thermomechanical pulp fiber. At different X-ray energies, core level electrons are excited to the anti-bonding π^* and σ^* orbitals. The sharp transition seen at 284.9 eV and 286.2 eV are characteristic of the C 1s→1 π^* (C=C) transition of aromatic (C-H) and phenolic carbons (C-O), respectively, and at 288.7 eV a peak corresponding to the C 1s→1 π^*(C=O) transition of carboxylic carbon[99]. These functional groups are present in lignin, as shown in Figure 3.3b. The peak at 290.4 eV is related to the aliphatic C-H carbons, and the broad peak at 293 eV to C 1s→σ^* transitions in aromatic and aliphatic carbons present in both cellulose and lignin. Due to the complexity of lignocellulosic materials, the results obtained when probing such materials using STXM with NEXAFS contrast can be difficult to interpret. A good approach is to compare the data with already known absorption edges of chemical compounds[100] and by including good reference samples to be measured at the same conditions.

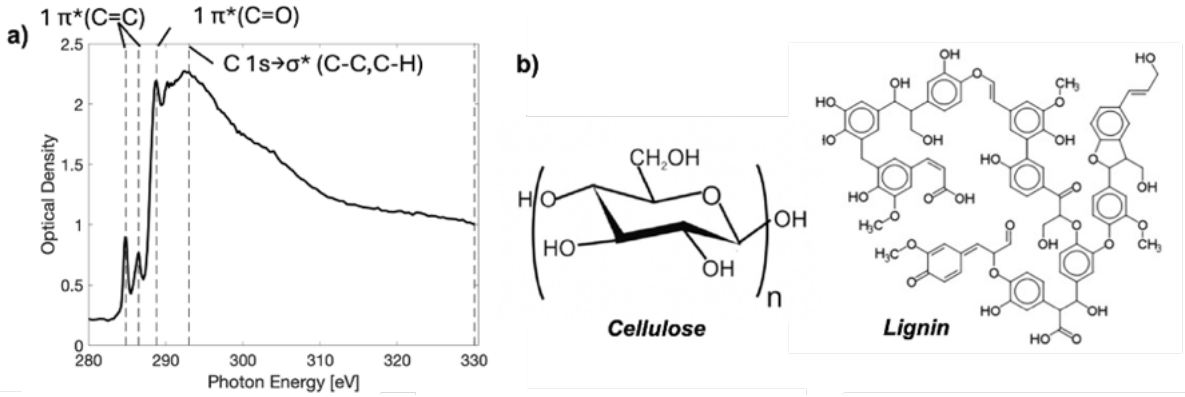

Figure 3.3. a) Characteristic NEXAFS spectrum from a lignocellulose fiber showing resonance energies from both lignin and cellulose components. b) Model structure of cellulose and lignin based on *Adler et al.*[101]

A main advantage of STXM at low X-ray energies is that the setup allows for very high spatial resolution, typically down to around 20 nm[97, 102] depending on the exact setup used. Furthermore, the energy resolution is high, typically around 0.1 eV, which allows for the identification of chemical bonds. Since each measurement point must be measured for each X-ray energy selected, the combination of high spatial and energy resolution can result in high radiation as well as long measurement times. To account for this, different data collection strategies can be taken.

In general, there are three main approaches for collecting STXM data called imaging mode, spectral mode and energy stacking mode[91]. In the imaging mode, the X-ray energy is fixed while the sample is raster scanned over the beam. If the energy is selected to match the absorption of a certain chemical species, this can be used to efficiently map the distribution with high spatial resolution over a large sample area. In the spectral mode, the scan is collected across the sample while the energy is varied over the carbon edge to provide the full NEXAFS spectrum. Using a high energy resolution gives a more comprehensive data set that is easier to interpret. In energy stacking mode, a few X-ray energies are selected that correspond to the resonance energies where absorption is the strongest for certain chemical compounds in the sample. Raster scanning is then used to map out these compounds across the sample, similarly to the imaging mode.

The modes can further be combined in different ways. Figure 3.4 shows an example where an energy stacking approach (left) is combined with a spectral approach (right). In the energy stacking mode, only a few selected energies are measured which allows the sample to be measured at a high spatial resolution. In contrast, the spectral mode is used to collect at a lower spatial resolution but instead allows for detailed spectral analysis across the same sample region. The resulting dataset thus includes both high spatial and high energy resolution over a large sample area, while minimizing the measurement time and radiation dose.

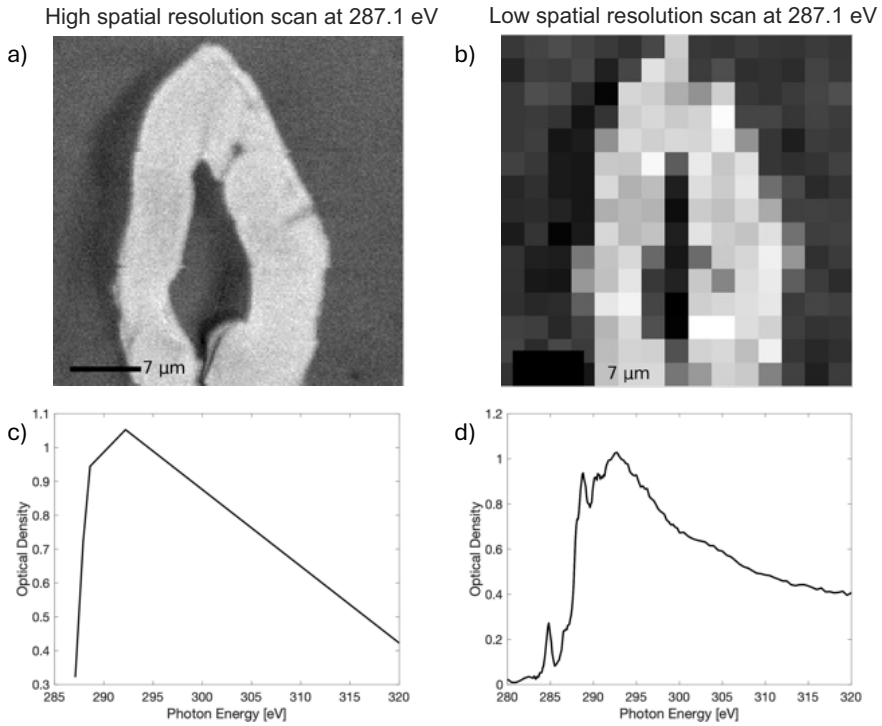

Figure 3.4. STXM images collected at 287.1 eV of a cross section of a fiber (a, b) and corresponding averaged NEXAFS spectra (c, d). The figure illustrates a measurement where the spatial resolution was optimized by a highly focused beam, with the compromise of fewer energy scans (a, c) and a measurement where the energy resolution over the fiber was optimized and instead the spatial resolution was compromised by using a defocused beam to collect the average absorption signal over the fiber providing the entire energy spectra of the cross section of the fiber (b, d).

3.4 Small and Wide angle X-ray scattering

X-ray scattering is a non-invasive technique sensitive to structural variations on length scales ranging from angstroms to hundreds of nanometers. The measured signal represents an average of all structural components over the whole depth of the illuminated sample volume. A typical experimental set up is shown in Figure 3.5, where a monochromatic X-ray beam with wave vector $\overrightarrow{k_i}$ is focused on a sample in transmission mode. Parts of the radiation will be scattered at an angle 2θ as defined by the vector $\overrightarrow{k_s}$ where the scattering intensity is measured by the detector behind the sample.

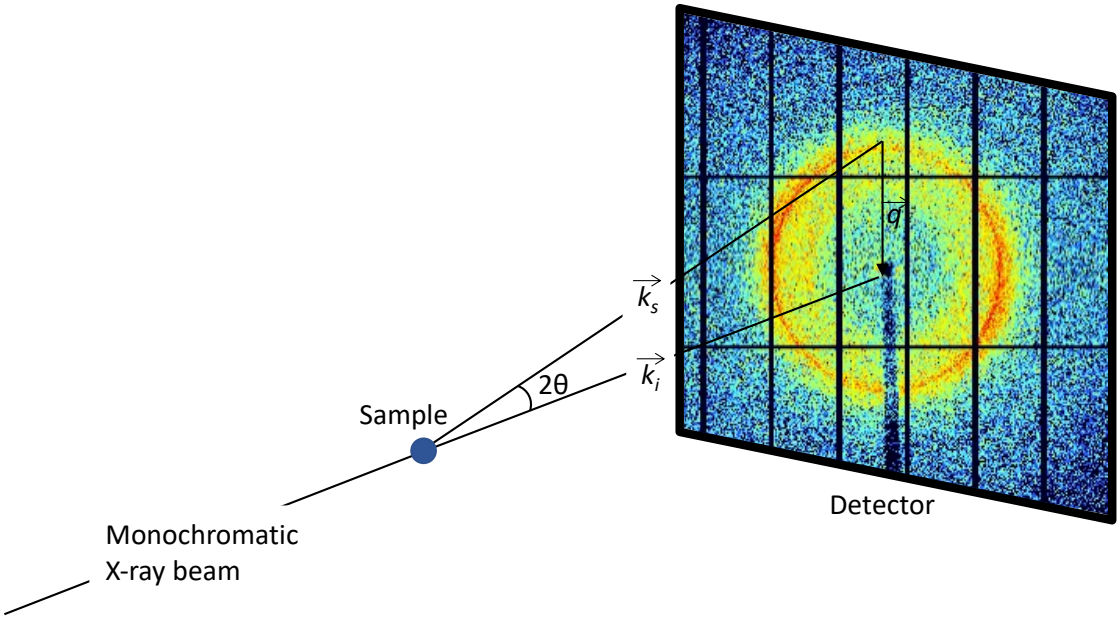

Figure 3.5. Transmission setup of the scattering experiment.

The recorded scattering pattern is the square of the Fourier transform of the electron-density distribution ρ(r) [74] according to

$$I(q) = \left| \int_V \rho(r) e^{-iqr} dr \right|^2 \qquad \textit{Equation } 3.3$$

where V is the sample volume. To resolve different structures, the electron densities in different domains or between scatterer and environment needs to be different enough, where the scattering intensity I(q) depends on the contrast ($\Delta\rho$).

Structures of different sizes can be investigated by resolving either the small- or the wide angles of the X-ray scattering. In practice this is done by changing the sample to detector distance. In SAXS the detector is typically placed meters away from the sample, which provides information on relatively large repeating structures inside the material, generally in the range of a few to hundreds of nanometers. In synthetic polymer materials, the SAXS signal is commonly used to characterize lamellar spacing[103] whereas in cellulose-based materials the SAXS signal can be used to investigate distances between the fibrils[104]. In WAXS the detector is placed centimeters away from the sample, providing information on small repeating structures in the Angstrom regime. In the crystalline regions of polymer materials, the positions of the atoms are well defined, giving rise to sharp WAXS peaks corresponding to the distance between atom planes. In addition, amorphous regions exhibit short-range order due to chemical van der Waals forces between polymer chains, giving rise to a broad WAXS-peak[105, 106]. Depending on the material investigated and research aims, different analysis approaches for SAXS and WAXS are needed. The analysis approaches used in this thesis are described below.

3.4.1 Bragg Peak Analysis

Highly ordered structures will scatter x-rays in specific directions, producing scattering patterns with sharp maxima which are referred to as diffraction peaks[91, 94]. These peaks correspond to the repeating distances within the material. Analyzing the characteristics of Bragg peaks is typically used in WAXS, due to the well-defined peaks arising from the crystalline unit cells. However, in systems that have repeating distances in the nanometer range, a similar analysis can also be used for SAXS.

Diffraction peaks appear according to Bragg's law,

$$n\lambda = 2dsin(\theta) \qquad Equation\ 3.4$$

where n is a positive integer, λ is the wavelength of the X-rays, d is the distance between the repeating structure and θ is the scattering angle. When analyzing the Bragg peaks, it is convenient to define a scattering vector $\vec{q}$ as

$$\vec{q} = \overrightarrow{k_i} - \overrightarrow{k_s} \qquad Equation\ 3.5$$

In case of elastic scattering, the scattering vector $\vec{q}$ fulfills Bragg's law and can thus be described as

$$|\vec{q}| = q = \frac{4\pi}{\lambda} sin\theta \qquad Equation\ 3.6$$

By substituting for $\frac{\sin(\theta)}{\lambda}$ in equation 3.4, a simple relationship between the scattering vector $\vec{q}$ and repeating distance d is obtained, which is independent on the energy of the X-ray beam.

$$q = \frac{2\pi}{d} \qquad Equation\ 3.7$$

Thus, the peak position can directly be linked to repeating distances in the material, providing valuable information of the samples.

3.4.2 Orientation Analysis

To investigate orientation effects of the samples, the scattering data was analyzed according to an approach proposed by Bunk et al.[107] where each 2D scattering pattern is divided into N_θ azimuthal segments. The azimuthal intensity distribution is approximated over the segments with a cosine function, as shown in the inset in Figure 3.6, where the measured values are indicated with black circles and the cosine approximation is shown in red. The baseline of the cosine function a_0 gives the symmetric intensity, which corresponds to the average scattering of the sample whereas the amplitude of the cosine function a_1 gives the asymmetric intensity which corresponds to the oriented part of the scattering. The degree

of orientation can be defined as the ratio a_1/a_0, and the phase of the signal Φ_s corresponds to the angle of orientation.

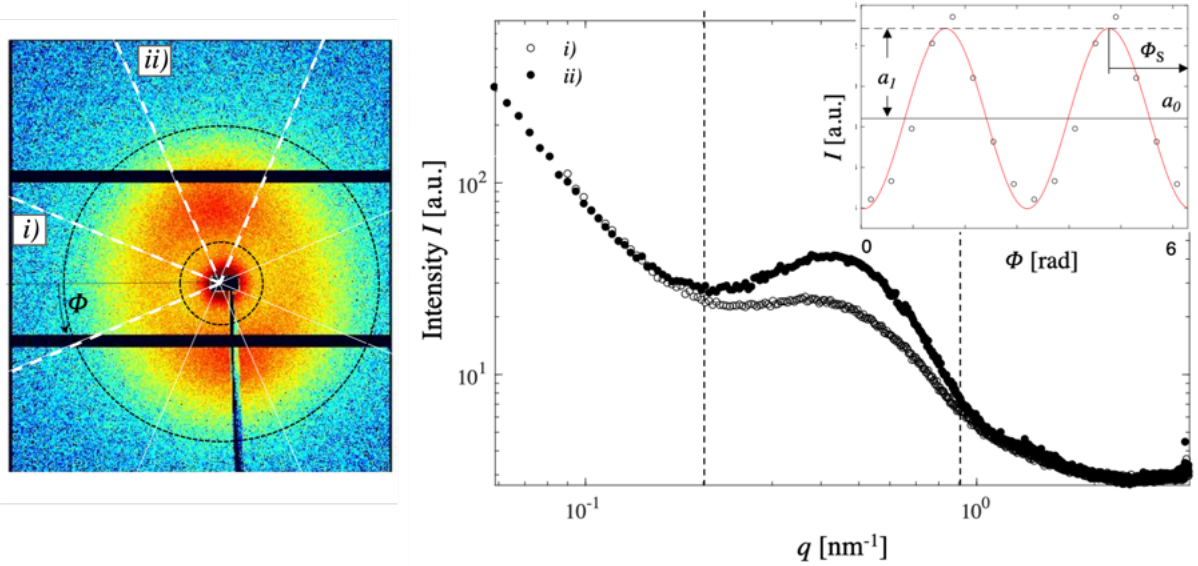

Figure 3.6. SAXS 2D pattern (left) and integrated intensity (right) of the skin layer of medium viscosity LDPE. The radial integration is performed in a horizontal i) and vertical azimuthal segment ii). The inset shows the azimuthal integrated intensity capturing the asymmetry of the scattering pattern in the q-range from 0.26 - 0.94 nm^{-1} as indicated with dashed circles and dashed lines, respectively.

3.4.3 1D correlation function analysis SAXS

The 1D correlation function analysis is a method to get detailed description of the polymer lamellar stack, which is composed of an amorphous phase and a crystalline phase. With this analysis it is possible to determine the lamellae thickness and crystallinity of semicrystalline polymers[108, 109]. The 1D correlation function K(z) is computed by taking the cosine Fourier Transform of the scattering data I(q),

$$K(z) = \frac{1}{Q}\int_0^\infty I(q)q^2\,cos(qz)\,dq \qquad Equation\ 3.8$$

where Q is the Porod invariant, which is independent of the size and shape of the structural heterogeneities. Q is defined as

$$Q = \int_0^\infty I(q)\,q^2 dq. \qquad Equation\ 3.9$$

The term q^2 in equation 3.8 and 3.9 stems from a Lorentz correction, meaning that the intensities are multiplied by q^2, to enhance any peaks in the scattering curve, as shown in Figure 3.7a. The integration requires data between q=0 and q=∞, and the experimental data do not extend to these limits. Consequently, extrapolation of the data is required. In the low q-range, the data can be extrapolated to q=0 by using a Guinier function to fit the data,

$$I(q) = Ae^{Bq^2} \qquad Equation\ 3.10$$

where B is related to the effective radius-of-gyration. In the high q-region, a Porod function can be used to extrapolate the data to q=∞,

$$I(q) = Kq^{-4}e^{-q^2\sigma^2} + Bg \qquad \textit{Equation } 3.11$$

where Bg is the background, K is the Porod constant, and σ describes the width of the electron/neutron scattering length density profile at the interface between the crystalline and amorphous regions. The extrapolation to low q has little impact on the final 1D correlation function due to the q^2 weighting in the integral, whereas accurate extrapolation to high q values is critical[110].

From the analysis, the lamellae thickness can be estimated by the triangle method[108], where the lamellae thickness Lt is taken as the intercept between the minimum value of K(z) and the initial slope, whereas the long period Lp, which is the distance of one crystalline and one amorphous layer, is taken as the position of the first maximum of K(z) as described in Figure 3.7b.

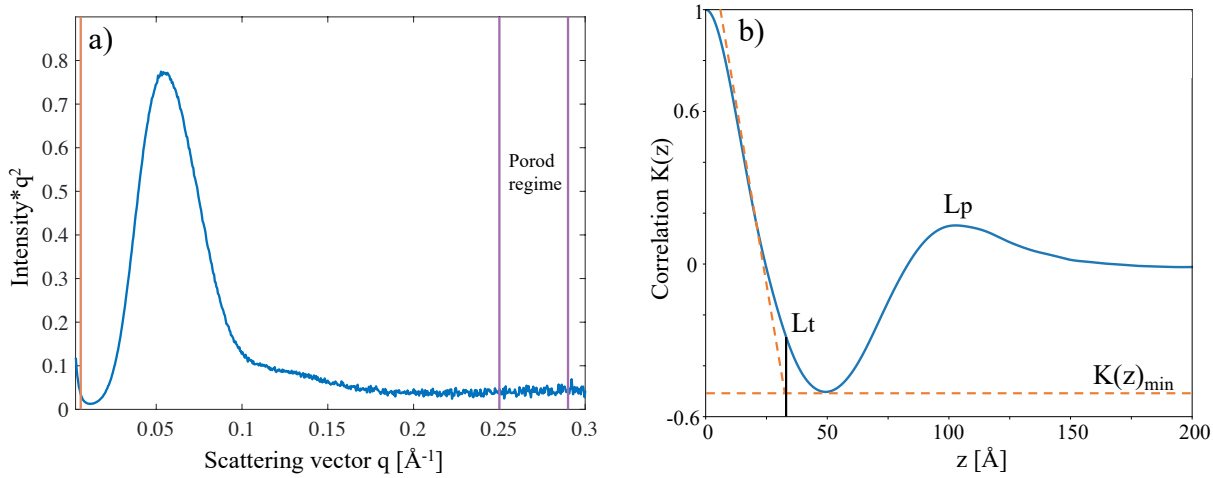

Figure 3.7. Example of Lorentz-corrected SAXS profile (a) and corresponding correlation function analysis (b), from medium viscosity LDPE taken in the shear layer. The data to the left of the orange line in a) was used to fit the Guinier function and extrapolate the data to q=0, whereas the region between the two purple vertical lines in a) were used to fit the Porod function and extrapolate the data to q=∞.

3.4.4 Model-based fitting SAXS

There are many analytical models that can be used to fit experimental SAXS data. To describe the scatterers, several variables are used to typical characteristics such as the shape, size, concentration and size distribution. These characteristics can be divided into a form factor P(q) and a structure factor S(q). The form factor is linked to the shape of the particle and polydispersity whereas the structure factor is linked to the interactions between neighboring particles[111].

For cellulose-based samples, this thesis used a model based on hexagonally packed cylinders[112] which was adapted to wood-based samples by Penttilä et al. and introduced as

the WoodSAS model[113]. To use the model, the full small angle scattering data is fitted with the function

$$I(q) = AI_{cyl}(q, \bar{R}, \Delta R, a, \Delta a) + Bexp\left(\frac{-q^2}{2\sigma^2}\right) + Cq^{-\alpha} \qquad Equation\ 3.12$$

where A, B, σ, C and are constants and $I_{cyl}(q)$ is the intensity from infinitely long cylinders organized in a hexagonal lattice with paracrystalline lattice distortion. R corresponds to the cylinder radius with mean $\bar{R}$ and standard deviation ΔR and a correspond to the distance between the cylinders' center points with standard deviation Δa.

The WoodSAS model is tailored for fitting the equatorial intensity profile from wood samples where the fibrils are aligned to the incident X-ray beam. However, in many paper-based samples the fibrils are close to randomly oriented which will affect the scattering form factor. For the case of randomly oriented fibrils, a Lorentz factor of q^{-1} needs to be multiplied as described by Hashimoto et al[112].

3.4.5 Crystallinity calculations WAXS

Several approaches exist for estimating the degree of crystallinity from WAXS data. One of the most common approaches primarily used for cellulose-based materials is the Segal method[114]. In the Segal method, the degree of crystallinity is calculated as

$$CrI = 100 * \frac{I_{cryst} - I_{non-cryst}}{I_{cryst}} \qquad Equation\ 3.13$$

where I_{cryst} is the height of the crystalline peak and $I_{non\text{-}cryst}$ is the height of the amorphous peak. In the case of cellulose, the (200) peak is often chosen as the crystalline peak whereas the amorphous peak is often taken as the minimum between the (110) and the (102) peaks. The Segal method is simple and widely used, however, it has many drawbacks. First, the measured spectrum always contains contributions from amorphous regions in the position of the crystalline peaks as well, giving an overestimation of the degree of crystallinity. Moreover, overlapping of crystalline peaks has an additional influence on the results[115]. Another difficulty is that the measured peak intensities are affected by the structure's preferred orientation, therefore, the measured intensity ratio and the apparent crystallinity can be strongly influenced by the orientation[116]. A 2D area detector or a rotating stage can be used to study or to minimize the orientation effect.

A more reliable approach to calculate the degree of crystallinity is the peak deconvolution method, where the peak area instead of just the peak height is taken into consideration. In this approach, the degree of crystallinity is calculated according to

$$C = 100 * \frac{A_{cr\ peak\ 1} + A_{cr\ peak\ 2} + \cdots + + A_{cr\ peak\ N}}{A_{cr\ peak\ 1} + A_{cr\ peak\ 2} + \cdots + + A_{cr\ peak\ N} + A_{non-cryst}} \qquad Equation\ 3.14$$

where A is taken as the area under peak[117]. For the deconvolution, a proper background subtraction is essential avoid uncorrected non-sample contributions (e.g., thermal diffuse scattering, Compton scattering, air scattering, diffraction of the sample holder, etc.), which could lead to reduced crystallinity values [118]. In most cases, during deconvolution, four (1-10, 110, 200 and 004)[119] or five crystalline peaks (1-10, 110, 102, 200 and 004)[120, 121] are fitted using Gaussian[120, 122], Lorentzian[119] and Voigt[121, 123] functions.

3.4.6 Crystallite size estimation WAXS

To estimate crystallite size in polymer materials, the Scherrer equation is often applied to diffraction peaks. The Scherrer equation relates the crystallite size D to the full width half maxima (FWHM) of the diffraction peak according to

$$D = \frac{K\lambda}{\beta cos\theta} \qquad Equation\ 3.15$$

where K is a constant, λ is the wavelength of the X-rays, and θ is the Bragg angle. The Scherrer equation is particularly useful for approximating crystallite sizes up to 200 nm[124], making it well suited for analyzing semi-crystalline polymers. A limitation of the Scherrer equation, is that it assumes that peak broadening comes solely from changes of crystallite size. In practice, peak broadening can also stem from several other factors such lattice strain, microstructural disorder, instrumental broadening and thermal motion, which can result in over or underestimation of the crystallite size[125].

3.5 Mechanical testing

In commercial applications, the inherent toughness and fracture resistance of polymer materials are of outermost importance. Mechanical testing is therefore widely used to evaluate both synthetic and cellulose-based polymer materials. For polyethylene, numerous studies have examined their mechanical response, with most studies focusing on isotropic polyethylene[126-130], and with a few studies published on anisotropic polyethylene with flow induced structures[131, 132]. In the case of cellulose-based polymers, mechanical testing is also commonly employed. However, their mechanical properties vary widely between different studies due to cellulose's inherent heterogeneity which arises from differences in raw material[133], growing conditions of the plant[134], potential thermal treatments[135], and chemical modifications[136]

One of the most widely used approaches to study mechanical characteristics of polymer materials is to measure the stress-strain behavior, where a tensile force is applied to the sample and the resulting deformation of the sample is measured. This gives information on

the modulus, brittleness, and strength of the polymer. An example of a stress-strain curve can be seen in Figure 3.8, showing the elastic and plastic regions. In the elastic region, the polymer can go back to its original shape if the tensile force is removed. At a certain threshold called the yield point, the polymer reaches its elastic limit and beyond this point the deformation of the polymer is permanent. This is called the plastic region, and here the elongation of the sample will continue at almost constant stress until the ultimate elongation is reached and the polymer breaks. A polymer is defined as brittle if the polymer fractures before the yield point is reached, whereas the polymer is defined as ductile if the polymer elongates into the plastic region[103].

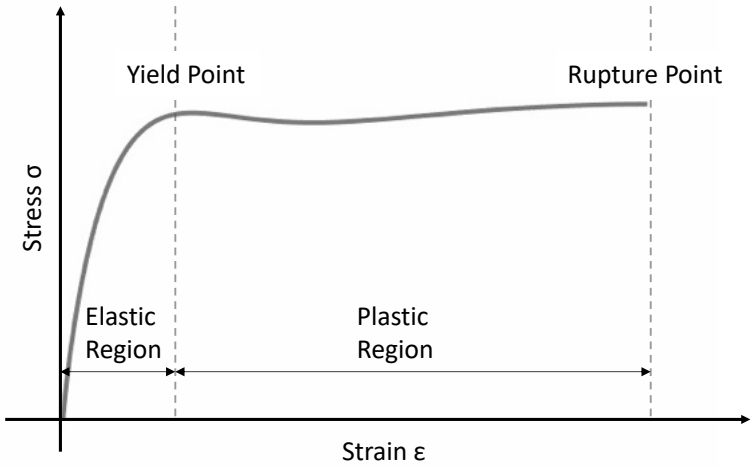

Figure 3.8. Stress-strain response of a typical polymer.

3.6 Birefringence Microscopy

Birefringence is an optical property where a material's refractive index varies depending on the polarization and direction of the incoming light. When light passes through a birefringent material, it is split into two separate rays with orthogonal polarizations. The two rays are referred to as the ordinary ray and the extraordinary ray. The ordinary ray travels at a constant velocity regardless of direction, while the extraordinary ray's velocity depends on its direction of propagation within the internal structures of the material. The difference in refractive indices between these two rays defines the birefringence (B) according to

$$B = |n_e - n_o| \qquad Equation\ 3.16$$

where n_e is the refractive index of the extraordinary ray and n_o is the refractive index of the ordinary ray. To quantify the optical path difference caused by this velocity difference, the retardation (Γ) is used

$$\Gamma = t * B \qquad Equation\ 3.17$$

where t is the thickness of the sample. The retardation reflects the phase difference introduced between the two rays as they propagate through the material. In birefringence microscopy, the birefringent properties of a material are measured by analyzing the change in the polarization state of light after it passes through the sample. In this work, a setup from Hinds instruments was used that consisted of a combination of polarizers and photoelastic modulators (PEMs), allowing for quantitative determination of both the optical fast axis (θ) and the retardance (Γ).

In polymeric materials, birefringence arises from optical anisotropy, which is a direct result of molecular orientation[137]. Ordering of polymer chains induces directional differences in the polarizability of the material. Light traveling parallel to the polymer chain alignment will encounter a different electronic environment compared to light traveling perpendicular to it, resulting in differing refractive indices. Thus, birefringence microscopy can be used to evaluate orientation in polymer materials. The more ordered or oriented the polymer chains, the greater the birefringence. This makes birefringence a powerful tool for assessing molecular orientation and structural anisotropy in polymer materials.

Chapter 4 – Materials and Experimental Methods

4.1 Materials

In this thesis, five types of materials have been studied, low density polyethylene, high density polyethylene, dialcohol cellulose, kraft pulp and thermomechanical pulp.

In Paper I and II, high-density polyethylene (HDPE) and low-density polyethylene (LDPE) were used, with two types of LDPE with varying viscosity and one type of HDPE. The LDPE had a density of 923 kg/m^3 and the HDPE had a density of 953 kg/m^3. The Melt Flow Index (MFI) was 55 g/10 min for the low viscosity LDPE, 22 g/10 min for the medium viscosity LDPE and 26 g/10 min for the HDPE min when measured at 190°C at a load of 2.16 kg.

In Paper III dialcohol cellulose (DALC) was probed together with Ethylene Acrylic Acid Copolymer (EAA) and in Paper IV pure dialcohol cellulose was used. The DALC was derived from bleached softwood kraft fibers by using oxidation and reduction with sodium periodate and sodium borohydride respectively, according to a partly modified version of an earlier described protocol[52, 138]. This resulted in conversion of cellulose to dialcohol cellulose with varying degrees of modification.

Paper V used a commercially available V2, 138 gsm paper derived from kraft pulp, a paper material that consists of 30-50% hardwood, 50-70% softwood and additives. The additives used were kaolin clay as a filler, cationic starch as a dry strength agent, rosin and alkyl ketene dimer as sizing agents and glyoxalated polyacrylamides as wet strength agents.

In Paper VI, Thermomechanical pulp (TMP) was used for the measurement. The TMP fibers were obtained from StoraEnso Hyltebruk, Sweden and were derived from Norway spruce (Picea abies). Fiber analysis of the TMP, performed using a Kajaani FS300, gave a respective mean fiber length, width, and fines distribution of 3.2 mm, 35 μm, and 3% [139], and have been reported to have 50 wt.% of polysaccharides and ca. 30–35 wt.% lignin [140].

4.2 Sample Preparation

In Paper I and II, the samples were injection molded with a hydraulic injection molding machine (Arburg 470 800-70S, Arburg GmbH Germany) to produce plates with a thickness of 0.6 mm according to ISO 294-5. The fixed mold half was made from steel DIN 45 NiCrMo 16, while the moving half plate was made from high-strength aluminum-zinc alloy AlZnMgCU 1,5. In Paper I, the injection temperature was 220 °C, the mold temperature was 40 °C, whereas in Paper II, the injection temperature was 260 °C the mold temperature was 60 °C. The injection volume flow, V/P switch-over points and holding pressures used in Paper I and II are summarized in table 4.1.

Table 4.1. Process settings used during the injection molding process in Paper I and II.

	Set Injection volume flow cm^3/s	V/P switch-over point (%)	Holding pressure (bar)
Paper I (LDPE)			
Medium viscosity	20	99	750 – 0.3 s – 500
Low viscosity	20	99	650 – 0.3 s – 450
Paper II (HDPE)			
High 85%	25	85	1100 – 1 s – 750
High 99%	25	99	1100 – 1 s - 500
Low 85%	20	85	1100 – 1 s – 750
Low 99%	20	99	1100 – 1 s – 500

In Paper III, the materials were melt processed at 80 °C or 120 °C using a DSM Xplore Micro 5cc twin-screw micro-compounder (Heerlen, Netherlands). After compounding, according to the standard ISO 527-2, dumbbell shaped (1BA) specimens and bars (60x10x1 mm3) were prepared by injection molding using a Thermo Scientific HAAKE Mini-Jet Pro (Thermo Fisher Scientific, Waltham, Massachusetts, USA) with the injection pressure of 1000 bar and an oven temperature of 140 °C and mold temperature of 40 °C.

In Paper IV, the initial water content was set to either 30 or 40 wt.%. Melt compounding was performed in an Xplore micro-compounder (Xplore, Maastricht, The Netherlands) at 100 °C. After the compounding step, the samples were either directly injection molded or dried in an oven at 70 °C for 48 hours and rehydrated to 30 wt.%. before the injection molding step. The injection molding was performed in an Xplore micro-injection molding equipment (Xplore, Maastricht, The Netherlands) with the injection pressure 7 bar, injection temperature of 125 °C and mold temperature of 30 °C. In Paper IV, samples were taken from different parts of the processing chain. An overview of the processing steps of Paper IV can be seen in Figure 4.1, where the samples measured are indicated by stars.

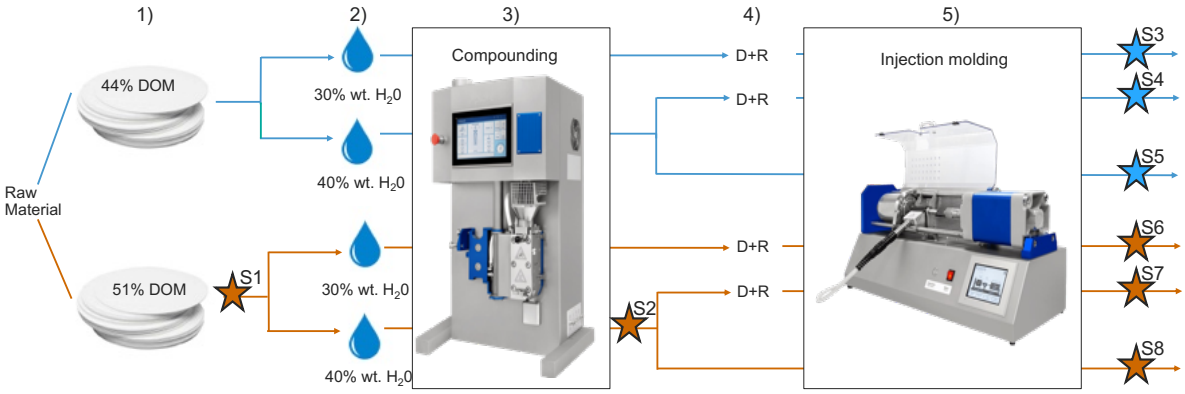

Figure 4.1. Overview of the processing scheme. 1) The raw material is modified to 44% or 51% degree of modification (DOM), 2) The water content is set to 30 or 40 wt.% water, 3) Compounding is performed, 4) The samples are either left untouched or dried and rehydrated (D+R) to 30 wt.% water, 5) Injection molding is performed. The stars indicate where in the process samples S1-S8 were taken.

The sample for scanning SAXS, WAXS and birefringence measured through the thickness in Paper I, II, III and IV were prepared by cutting slices of 50 µm using a Microtome (Leica RM2255 from Triolab for LDPE and HDPE and RMC MT-XL ultramicrotome for cellulose-based samples). LDPE and HDPE were evaluated in two separate directions, cross direction-thickness direction (CD-TD) and machine direction-thickness direction (MD-TD) as described in Figure 4.2.

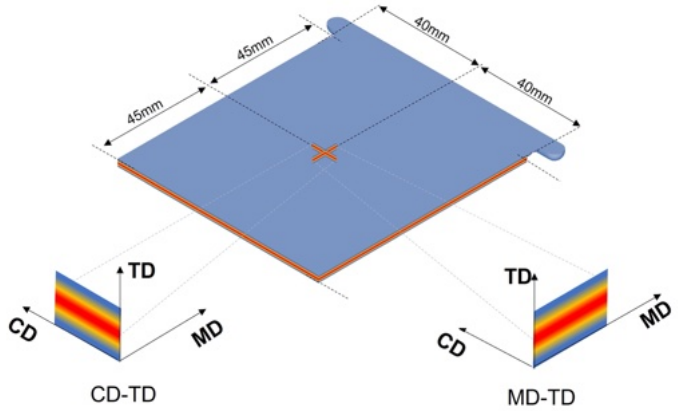

Figure 4.2. Injection-molded test plate with dimensions and positions of the measured samples. The layered structure along the thickness direction (TD) was studied by preparing cross-section in CD-TD, and MD-TD plane, respectively.

In Paper VI, the STXM samples were prepared using five different sample preparation strategies.

1) Spurr epoxy sample preparation protocol: Samples were embedded in Spurr epoxy resin with ERL-4221D formulation. The epoxy was polymerized in an oven at 65 °C overnight before cutting at room temperature.
2) Cycloamine based epoxy sample preparation protocol (CBE): Epoxy resin derived from a 1:1 mixture of 4,4-methylenebis(2-methylcyclohexylamine) and 2-[2,2-bis(oxiran-2-ylmethoxymethyl)butoxymethyl]oxirane was used, following a method adapted Späth et al[141]. As with the Spurr epoxy sample protocol, the epoxy was polymerized at 65 °C overnight before cutting at room temperature[142-144].
3) Sucrose sample preparation protocols: Fibers were immersed in a 2M sucrose solution. After soaking, the fibers were sandwiched between pieces of plastic and filter paper to make handling the fragile material easier. Cryo-sectioning was performed at -160 °C.
4) Water sample preparation protocols: The fibers were immersed in pure MQ water. Similar to the sucrose sample preparation protocol, after immersion, the samples were sandwiched between pieces of plastic and filter paper to make handling the fragile material easier while sectioning in cryogenic conditions at -160 °C.
5) Sulphur sample preparation protocol: Adapted from Lehmann et al.[142] and Noguchi et al.[143], elemental Sulphur was used as embedding material. Sulphur (0.75 g) was placed on a tray of aluminum foil at 170°C for 2 minutes until the Sulphur became viscous and reddish-brown. This temperature was kept below values reported in previous studies to minimize thermal degradation. At temperatures above 159 °C, S_8-rings in elemental Sulphur open and form diradicals, where the radicals then polymerize into long chains which increases the viscosity[144]. The Sulphur was then quenched in liquid nitrogen, where the Sulphur becomes amorphous. The samples were then warmed in ambient conditions for 2-4 minutes until it turned into a viscous state, where cellulose fibers carefully could be pressed into the Sulphur using tweezers. The optimum consistency for this step only lasted for about 10–30 seconds, after which the amorphous Sulphur converts to a microcrystalline but still plastic, state. Once embedded, the samples were cryo-sectioned at –160 °C.

All samples were cut into 150 nm thin sections, using a ultramicrotome Leica EM FC7. The sections were transferred onto 100 nm-thick silicon nitride (Si_3N_4) membranes and stored at room temperature prior to STXM measurements.

4.3 Synchrotron SAXS and WAXS

In Paper I-V, synchrotron based SAXS and/or WAXS was used. The experimental parameters used in each paper are summarized in table 4.2.

Table 4.2. Experimental parameters used in the scanning SAXS/WAXS experiments in Paper I-V

	Paper I	Paper II	Paper III	Paper IV	Paper V
Synchrotron	SLS	SLS	SLS	SLS	MAXIV
Beamline	cSAXS	cSAXS	cSAXS	cSAXS	ForMAX
X-ray Energy	11.2 keV	12.4 keV	12.4 keV	12.4 keV	12.7 keV
Beam Size (μm)	7.5x28 / 40x40	42x4	42x4	6x45	15x56
Scanning step size (μm)	10x25/ 40x40/ 60x60	40x10 / 40x5	40x5	40x6	N/A
SAXS Sample-to-Detector distance (mm)	2183 /2167	2171	N/A	2181	2144.8
WAXS sample-to- detector distance (mm)	N/A	250	250	261	N/A
Exposure time (ms)	100	60	60	100	300

The scattering data was analyzed according to section 3.4.2, where the 2D scattering patterns were azimuthally integrated in N_θ angular segments and the orientation and degree of orientation were analyzed in specific q-ranges according to Bunk et al[107]. The number of azimuthal segments and the q-regions used the analysis is summarized in table 4.3

Table 4.3. Number of azimuthal segments and q-regions used for the analysis in Paper I-V

	Paper I	Paper II	Paper III	Paper IV	Paper V
Azimuthal segments	16	16	16	32	32
q-regions analyzed (nm^{-1})	0.26–0.94 0.01-0.17 0.31-0.84 0.21-0.90 0.22-1.89 0.25-0.29 0.86-0.89 0.17-0.2 1.91-1.94	14.3-16.3 16.3-17.6 0.145-0.623	10.2–10.7 10.2–10.7	0.0446– 0.0991 0.253-1.2 15.1-16.5	N/A

4.4 Synchrotron STXM

In Paper VI, the STXM measurements were performed at the PolLux beamline at the Swiss Light Source synchrotron (SLS). The X-ray beam was focused to ≥30nm by using a Fresnel zone plate and the transmitted signal was detected by a photomultiplier tube (PMT), coupled with a phosphor screen. A higher order suppressor[145] was used to suppress higher order light that distort the spectra. To collect the NEXAFS spectra, the energy was varied from 280-350 eV with a step size of 0.1 eV around the absorption edge and 1 eV in the post-edge region.

To analyze the data, the MATNIS analysis software was used[146], to convert the transmission signal to optical density according to equation 3.2. The incident X-ray flux was measured in an empty region on the sample holder. To correct for thickness variations across the sample, a normalization was performed by dividing with the post-edge measurement, which is sensitive to changes of the electron density.

4.5 Tensile Testing

In this thesis, the mechanical testing of polyethylene materials was conducted using a standard tensile test equipment Zwick Z010 Proline [ZwickRoell, Germany], equipped with a load cell of 1 kN. The tests were performed with a loading rate of 100 mm/min and a gauge length between the grips of 58 mm. Ten samples were measured for each material, and the results were averaged to obtain the stress-strain curve.

The characterization of the cellulose-based materials in Paper III was performed by Giada Lo Re using a single column Instron 5944 (Norwood, Massachusetts, USA) tensile micro

tester with a load cell of 2 kN. The tests were performed with a loading rate of 15 mm/min using a gauge length between the grips of 30 mm. Five samples were measured for each material composition.

4.6 Birefringence Microscopy

The retardance and angle of the optical fast axis was measured with a birefringence imaging microscope (EXICOR MICROIMAGERTM, Hinds Instruments, Inc., OR) to investigate the multilayered structure of injection molded HDPE. The setup used consisted of a linear polarizer at 0°, a photo-elastic modulator (PEM) at 45°, a PEM at 0° and a linear polarizer at 45°. Due to the high level of birefringence, the phase unwrapping technology included in the Hinds software was used, which combined measurements from four stroboscopic light sources (LED, with wavelength 655 nm, 615 nm, 530 nm and 475 nm). The samples were measured with a 10x objective in front of a 2048x2048 pixel 12-bit CCD camera resulting in a spatial resolution of 0.5 μm/pixel and a field of view of 1 mmx1 mm.

Chapter 5 – Results and Discussion

5.1 Small- and Wide-angle X-ray scattering of polymer packaging materials

The results shown in this section demonstrate how SAXS/WAXS can be used to investigate the hierarchical structures of polymer packaging materials over multiple length scales. The data presented is included in Paper I-V and the emphasis here is put on comparison between the different materials and analysis approaches.

5.1.1 Scattering profiles of synthetic and cellulose-based polymers

Examples of a radial integrated SAXS and WAXS curves for synthetic low-density polyethylene (LDPE), high density polyethylene (HDPE) and a cellulose-based dialcohol cellulose (DALC) are shown in Figure 5.1. In the SAXS data of polyethylene (Figure 5.1a, b) a broad peak at 0.3-0.4 nm^{-1} is clearly visible. This peak corresponds to a real space distance of ≈16-21 nm, which is associated to the repeating distance d_{ac} that includes one amorphous and one crystalline layer. In the DALC sample, the SAXS curve has a small shoulder at 0.5 nm^{-1} that is much less pronounced compared to the peak in polyethylene (Figure 5.1b). This peak can be associated with the average distance between cellulose fibrils or microfibril bundles, as well as swelling of the cellulose fibrils [113, 147, 148]

Comparing the scattering of LDPE and HDPE, the SAXS peak position is found at a higher q value around 0.4 nm^{-1} in LDPE compared to HDPE at around 0.3 nm^{-1}. This indicates that lamellae distance d_{ac} is significantly smaller in LDPE, which is expected since increased density of polyethylene is associated with increased lamellae thickness[149 150]. To account for this, different q-regions were used to evaluate the lamellae peak for the different samples, where a q-region of 0.26 - 0.94 nm^{-1} was used for the LDPE, a q-region of 0.145-0.623 nm^{-1} was used for the HDPE. When comparing the peak width, LDPE had a significantly wider peak, which implies that there is a larger variety of d_{ac} present in the sample. This stems from LDPE having more branching along the polymer chains, resulting in more disordered lamellae and more irregular lamellae spacings. For HDPE, the scattering showed a second much weaker peak around 0.8 nm^{-1} which corresponds to a real space distance of ≈ 8 nm. This peak has not been studied further in this thesis, but plausibly the peak stems from thickness contributions from either the crystalline or the amorphous layer.

In the WAXS regime, the peaks correspond to inter-molecular distances, where sharp peaks correspond to molecular distances in the crystalline regions. In polyethylene (Figure 5.1c), the peaks at 15.1 nm^{-1}, 16.6 nm^{-1}, 21.0 nm^{-1}, 25.3 nm^{-1} and 26.6 nm^{-1} corresponds to the (110)-, (200)-, (210)-, (020)- and (120)-planes respectively. Besides the sharp crystalline peaks, a broad peak at ~14.8 nm^{-1} is visible which corresponds to the inter-molecular distances in the amorphous region. In dialcohol cellulose, the crystalline peaks at 1.0 $Å^{-1}$,

1.2 $Å^{-1}$, 1.5 $Å^{-1}$,1.6 $Å^{-1}$ and 2.4 $Å^{-1}$ correspond to the (1-10)-, (110)-, (102)-, (200)-, and (004)-crystalline planes. Similarly to polyethylene, a broad cellulose has a broad peak from the amorphous region, ~1.3 $Å^{-1}$. The differentiation between the crystalline and amorphous peaks is more clearly visible when performing a peak fit analysis, see section 5.1.3. When comparing LDPE and HDPE, the crystalline WAXS peaks are notably more pronounced in HDPE compared to LDPE, indicating a higher degree of crystallinity as expected from the more linear polymer chains.

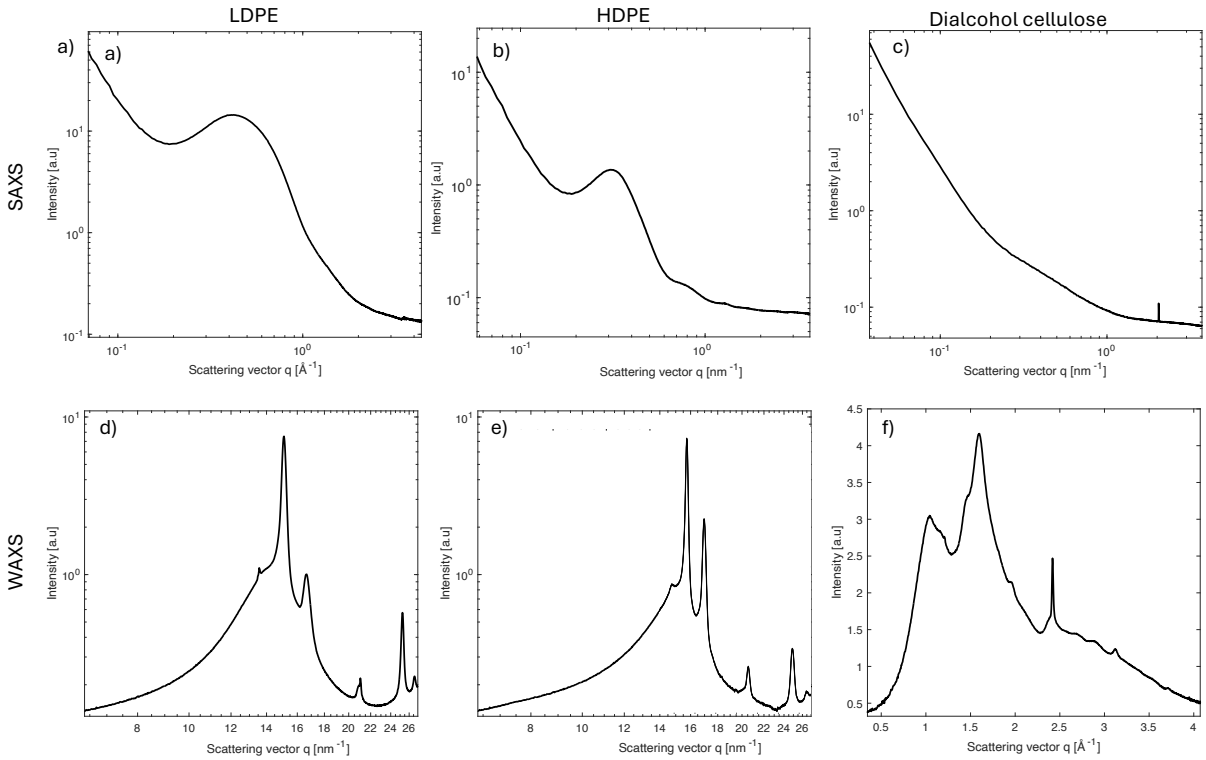

Figure 5.1. Examples of SAXS and WAXS integrated intensities for LDPE (a, d), HDPE (b, e) and dialcohol cellulose (c, f).

In Paper III, the cellulose-based materials investigated were a two-component system consisting of dialcohol cellulose and EAA-polymer matrix. Figure 5.2 shows radially integrated WAXS data from different compositions of fiber and cellulose, where the top curve in light blue corresponds to 100% modified cellulose fibers, and the bottom dark blue curve corresponds to 100% EAA. The samples that contained both dialcohol cellulose and EAA, had scattering profiles that clearly showed contributions from both components. In order to study the two components separately, two regions were identified where only one of the components had scattering signal, q=10.2-10.7 nm^{-1} which was the (110)-peak in cellulose marked in green and q=24.8-25.9 nm^{-1} corresponding to the (020)-peak in EAA marked in blue. These regions were used when analyzing the scanning WAXS-data, see section 5.2.5.

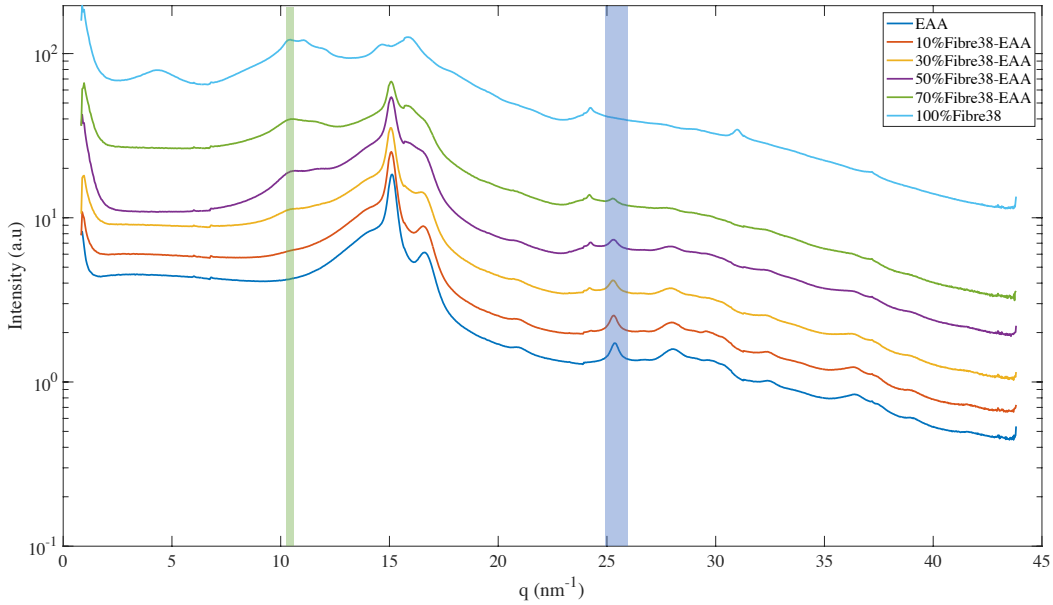

Figure 5.2. WAXS results showing integrated intensity as a function of scattering vector q for EAA, fiber composites and modified cellulose. The integrated data is averaged over all scattering angles. The green region of 10.2-10.7 nm^{-1} and blue region of 24.8-25.9 nm^{-1} indicates the regions that were used to analyze the cellulose (110)-peak and the EAA (020)-peak respectively.

5.1.2 Peak fitting small angle X-ray scattering

To get more information from the small angle scattering data, either a model-free or model-based peak fitting approach can be used. A model-free approach was taken in Paper I, Paper II, and Paper IV. The power law decay before- and after the peak was approximated by a negative exponential and subtracted from the data. The remaining signal was approximated with a Gaussian function, from which the peak position, width, and amplitude were obtained. An example of this peak fitting procedure from low density polyethylene is shown in Figure 5.3.

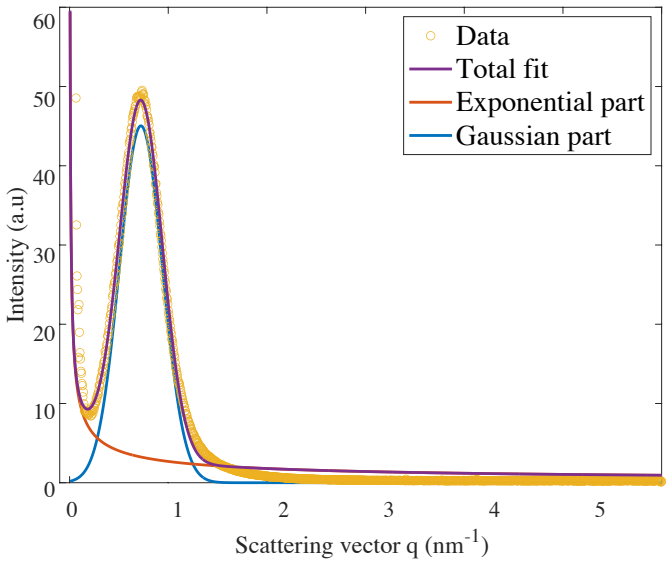

Figure 5.3. Example of peak fitting procedure. The fit consists of a negative exponential and a Gaussian peak.

In Paper V, a model-based approach was used to fit the integrated SAXS curves on a commercial paper-based material. The Wood-SAS model was used, and the results are shown in Figure (5.4). The key fitting parameters extracted from the model include the cylinder scaling factor (A), the fibril diameter (2R), and the center-to-center distance between fibrils. When decreasing the relative humidity, a decrease in the microfibril packing distance and cylinder scaling factor was observed, due to that water withdraws from the space between the microfibrils. This trend aligns with previous reports on natural wood [113]. However, the degree of structural response in the commercial paper material was notably more pronounced than that typically seen in intact wood. In our samples, the fibril diameter decreased by 23% from 2.26 nm at 95% RH to 1.74 nm at 0% RH, while the center-to-center distance between fibrils decreased by 64%, from 6.6 nm to 2.4 nm. For comparison, literature reports on wood indicate corresponding changes of only 2–7.4% in fibril diameter and 22–31% in fibril spacing over similar RH ranges[113]. This amplified response in the paper material likely arises from its inherently reduced structural integrity compared to native wood. Paper fibers, once separated and processed, are less tightly bound and have more accessible internal surfaces. Additionally, the lack of lignin and reduced hemicellulose content in processed paper may increase its susceptibility to moisture-induced changes. Consequently, water can penetrate and leave the interfibrillar regions more easily, resulting in more significant structural rearrangements upon drying.

The benefits of using a model-based approach compared to a model-free approach are that more information can be obtained and that the model parameters have direct physical meaning, which provides more straightforward interpretations. For instance, in the cellulose-based materials, the shoulder seen in SAXS contains information on both the fibril diameter and the distance between fibrils, and just extracting the peak position, width and amplitude is not enough to resolve the two contributions. However, a drawback of model-based analysis is that it relies on assumptions about the sample structure and morphology. If these underlying assumptions are wrong, the resulting parameters may be misleading, even if the fit appears good. Furthermore, in the model-based approach there is a risk of having correlated parameters, and that different fitting parameters provide similar fits. A benefit of using a model-free approach is that it is much simpler, and it can be automated to analyze many scattering patterns. This is particularly useful when performing scanning SAXS where thousands of scattering images can be collected for each sample.

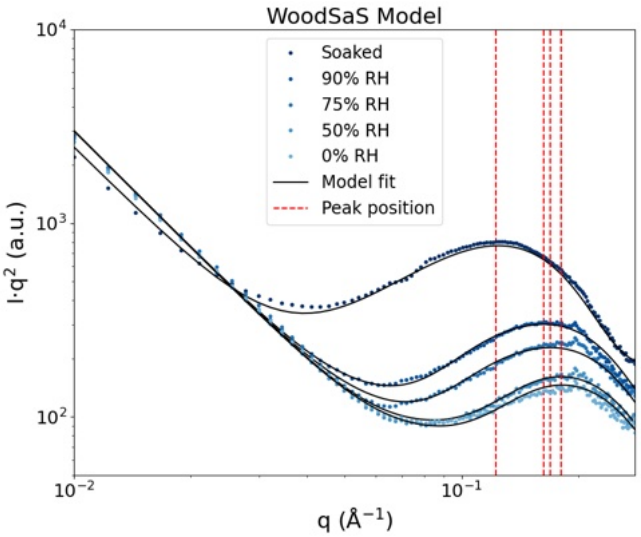

Figure 5.4. Small Angle scattering data as well as fitting results from the WoodSAS model at different levels of equilibrated relative humidity.

5.1.3 Peak fitting WAXS

Peak fitting of the WAXS-data was performed in Paper I, II and IV. An example for peak fitting in WAXS of low-density polyethylene is shown in Figure 5.5 a) and of dialcohol cellulose is shown in Figure 5.5 b). For both polyethylene and dialcohol cellulose, a deconvolution approach was used, where both crystalline and amorphous peaks were fitted individually by Gaussian functions. In the case of polyethylene, there were smaller overlaps of the peaks compared to dialcohol cellulose, making it easier to perform the fitting.

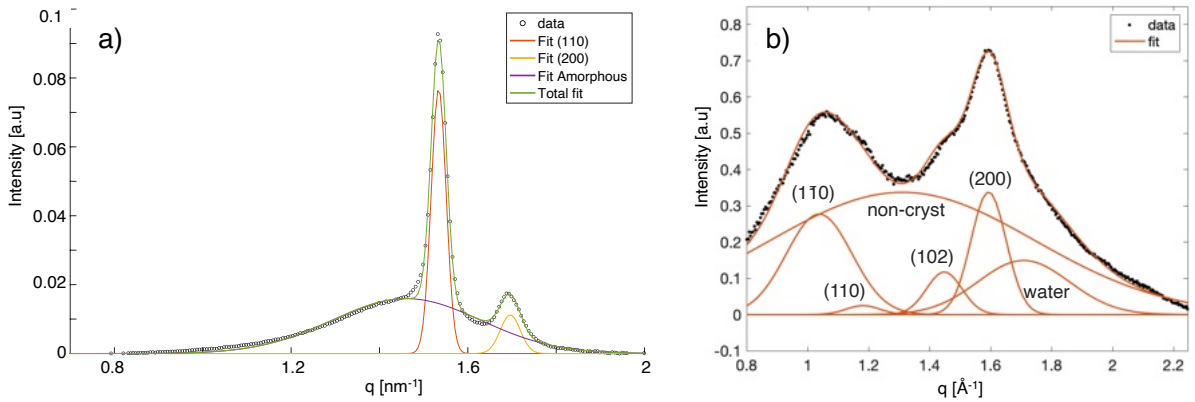

Figure 5.5. Peak fitting of WAXS data for a) polyethylene and b) dialcohol cellulose.

5.1.4 Comparing dialcohol cellulose derived from wheat and wood pulp

In this thesis, the dialcohol cellulose studied in Paper III and IV were derived from wood pulp. However, dialcohol cellulose can be derived from other lignocellulosic sources as well, such as wheat straw. Initial scattering experiments have been performed to evaluate structural differences between dialcohol cellulose derived from wood pulp and wheat, see Figure 5.6. The samples derived from wheat-straw display a noticeably higher scattered intensity in the low q region compared to the wood derived samples. The scattering intensity in this range scales with specific surface area of internal interfaces, and we

hypothesize that the scattering increase at low q observed in the wheat-derived sample stems from fractures, cracks and voids when preparing the samples. Furthermore, in the wheat-derived samples, the SAXS peak that is associated with distance between microfibrils was shifted to higher q-values, indicating a smaller fibril spacing.

From the WAXS, all crystalline peaks were weaker in intensity in the wheat-derived sample compared to the wood pulp reference. This shows that the wheat-derived sample has a lower degree of crystallinity, which affects the mechanical performance of the material. Furthermore, looking closely at the (200)-peak, a slight shift of the peak position is observed towards lower q in the wheat derived sample. This could be an effect from lattice strains, resulting in a slightly larger unit cell.

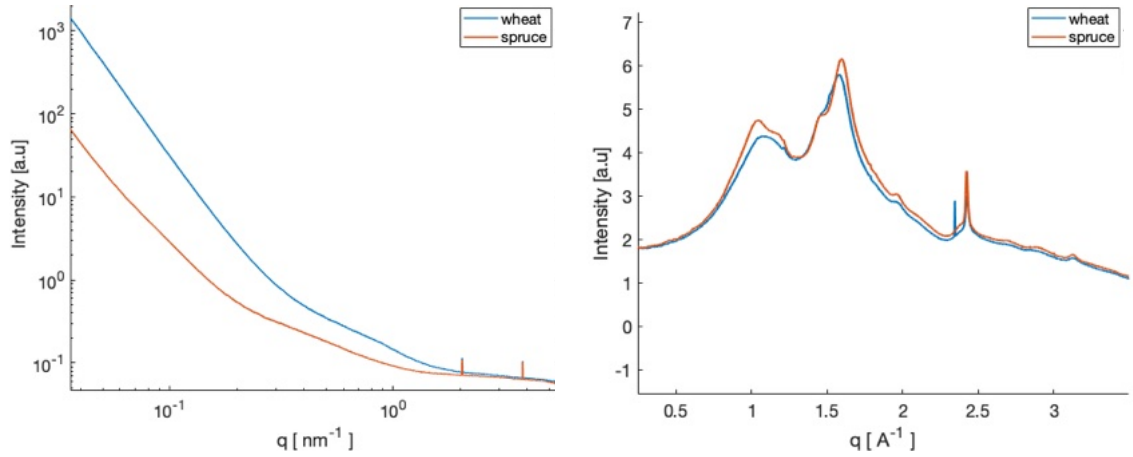

Figure 5.6. SAXS and WAXS results from wheat-derived and wood-pulp derived dialcohol cellulose.

5.2 Using scanning SAXS and WAXS to study process induced polymer morphology

Scanning X-ray scattering techniques were used to evaluate how structures changed across extended areas of the sample in both synthetic and cellulose based packaging materials.

5.2.1 Comparing injection molded polyethylene and cellulose-based samples

In this thesis, the use of scanning-based techniques has been particularly useful for injection molded samples, since they display a similar multilayered morphology both for polyethylene based and cellulose based materials, studied in Paper I, Paper II, Paper III and Paper IV (Figure 5.7). The degree of orientation for all samples was highest close to the edge of the sample, whereas a low degree of orientation could be found close to the center of the sample. The multilayered structure is a consequence of the fountain flow of the injection molding process, where high shear close to the edge induces orientation of the polymer chains and fast cooling from the cold mold freezes the structures in place. Figure 5.7a-b show degree of orientation values of the scattering peak for SAXS of LDPE and HDPE respectively, where the peak corresponds to the center-to-center distance of the crystalline

lamellae. The different materials were prepared with different process settings, making it difficult to compare absolute values of the degree of orientation, both between polyethylene and dialcohol cellulose, as well as between HDPE and LDPE. Thus, only qualitative comparison can be done in between the different materials studied within this thesis. Furthermore, the different materials are composed of different hierarchical structures, where the degree of orientation is highly affected by the form of the structures.

Comparing the degree of orientation in WAXS between HDPE and the dialcohol cellulose materials, HDPE gives rise to significantly higher degree of orientation values and sharper transitions between the different layers (Figure 5.7c-e). This is hypothesized to be a result of the well-defined hierarchical structures polyethylene can form. Above a certain threshold value of shear rate cooling rate and pressure, polyethylene is transitioned from a spherulite to a shish-kebab microstructure causing a drastic change of the scattering signal, as discussed in detail in Paper II. Cellulose, on the other hand, cannot form such structures due to more intrinsic disorder built into the polymer chains, resulting in less long-range order and an overall lower degree of orientation. Crystalline parts of cellulose have been reported to consist of roughly 15-30 cellulose chains which correspond to crystalline regions of 2-4 nm[151-153]. This is considerably smaller than the crystalline regions of polyethylene, where typical sizes of the crystalline lamellae are around 10 nm thick and 1-50 μm long[154, 155].

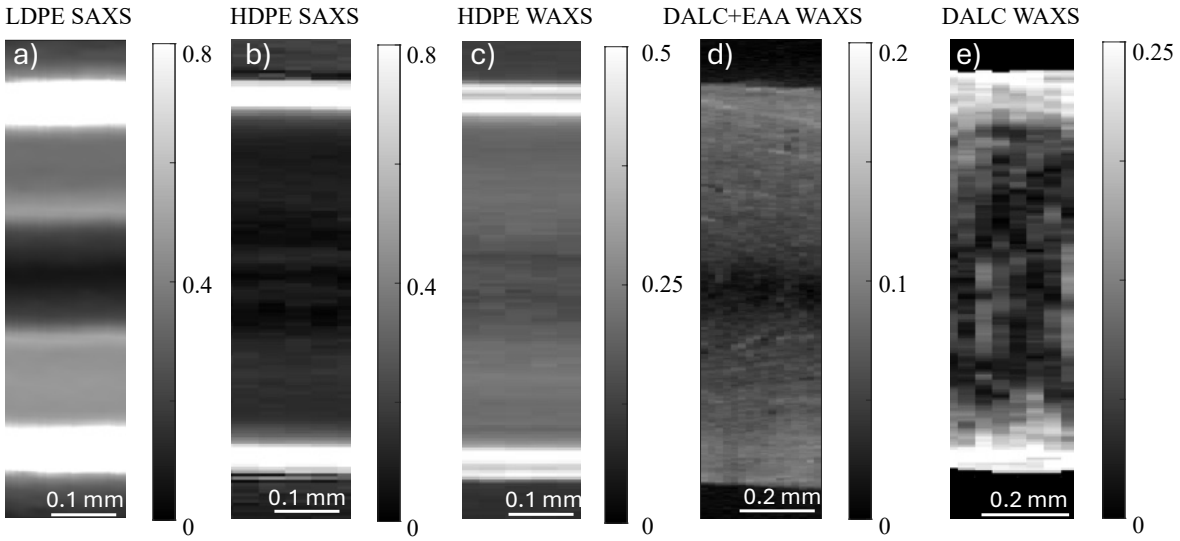

Figure 5.7. Degree of orientation calculated for a-b) SAXS long distance peak of LDPE, c-d) SAXS long distance peak of HDPE, e) WAXS (110)-peak of HDPE and f) WAXS (110)-peak of cellulose in an EAA polymer matrix. The SAXS results are taken from two perpendicular planes, MD-TD and CD-TD respectively.

5.2.2 Injection molded low density polyethylene

The multilayered morphology of injection molded LDPE was investigated in more detail in Paper I. The symmetric intensity, degree of orientation, and long-period spacing profiles

were compared together with selected 2D SAXS patterns, see Figure 5.8. From this analysis, four distinct layers could be identified and characterized according to points A1-4 and B1-4.

In layer 1, located near the mold wall, scattering patterns in both MD–TD and CD–TD planes revealed sharp vertical streaks and in MD-TD, a two-point pattern could be observed in the 2D SAXS pattern. This scattering pattern corresponds to a shish-kebab microstructure. The extracted long-period spacing in this region (from the MD–TD plane) was ~11.3 nm. Layer 2 was distinguishable from Layer 1 by a reduction in the vertical streak intensity and an increase in the lamellar two-point pattern. This indicates a decrease in shish content. The long period in this region was significantly larger compared to layer 1 at ~12.4 nm. Differences between the two layers were evident in low-q data, while the q-range of 0.26–0.94 nm^{-1} showed similar degree of orientation values. Layer 3 exhibited scattering patterns with slight anisotropy in the MD–TD plane and isotropy in the CD–TD plane, consistent with elongated spherulites oriented in the flow direction. The extracted long-period spacing was ~11.1 nm. These features align with microstructural models proposed by Katti and Schultz[12], where lamellae of elongated spherulites are preferentially oriented perpendicular to the flow. Layer 4 displayed nearly isotropic scattering in both the CD-TD and MD-TD planes, and similar long-period spacing (~11.1 nm), indicating randomly oriented, symmetric spherulitic morphology.

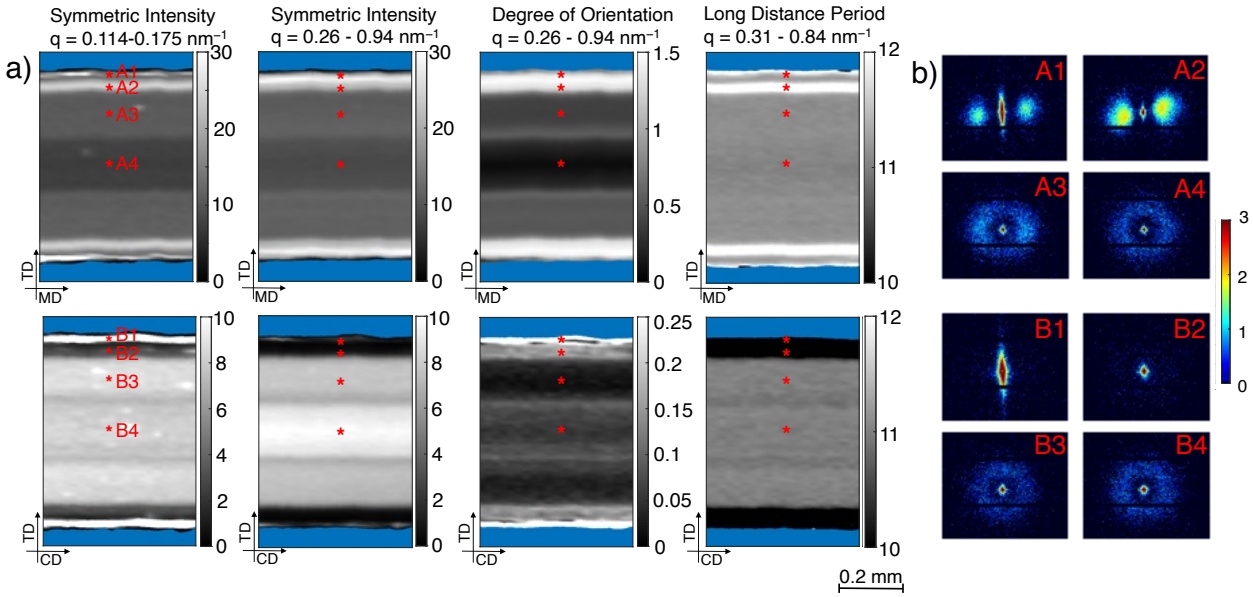

Figure 5.8. Symmetric intensity, degree of orientation and calculated long period from the center of the plate for cross sections of medium viscosity LDPE, perpendicular (CD-TD plane) and parallel (MD-TD plane) to the flow (a), as well as scattering patterns from selected points A1-4 and B1-4 along the plate thickness (b). Note that the scale of the color bar differs between MD-TD and CD-TD, as the intensity and degree of orientation, respectively, differ significantly. Blue represents masked areas outside the sample.

5.2.3 Injection molded high density polyethylene

In Paper II, we show that high density polyethylene has a more complex morphology compared to low density polyethylene, where five distinct layers were present (Figure 5.9).

The more complex morphology in HDPE compared to LDPE is believed to be a consequence of less branching of the chains, making HDPE more prone to form highly ordered crystalline structures. To define the five layers, 2D SAXS patterns were combined with 2D WAXS patterns to obtain more in-depth information on the hierarchical structures. Interestingly, a clear difference in the WAXS 2D scattering patterns was observed between layer 1 and layer 2, closest to the edge of the sample. In layer 1, the WAXS 2D pattern has four maxima scattered as a cross along the horizontal plane in the (110) crystal plane, two maxima along the vertical plane in the (200) crystal plane, and two broad maxima along the horizontal plane in the (020) crystal plane. This is a typical WAXS pattern for shish-kebab with twisted lamellae, as indicated by the structure in Figure 5.9b[30,156]. In layer 2, the vertical streak in the SAXS signal is less pronounced, whereas the two-point pattern is more intense, indicating less shish-structures present in the sample and more growth of the crystalline lamellae. In WAXS, the crystal (110)-, (200)-, and (020)-planes are aligned in the vertical direction. These are typical characteristics for shish-kebab with untwisted lamellae. In order to reveal the type of shish-kebab structure present, a combination of SAXS and WAXS 2D patterns must be used.

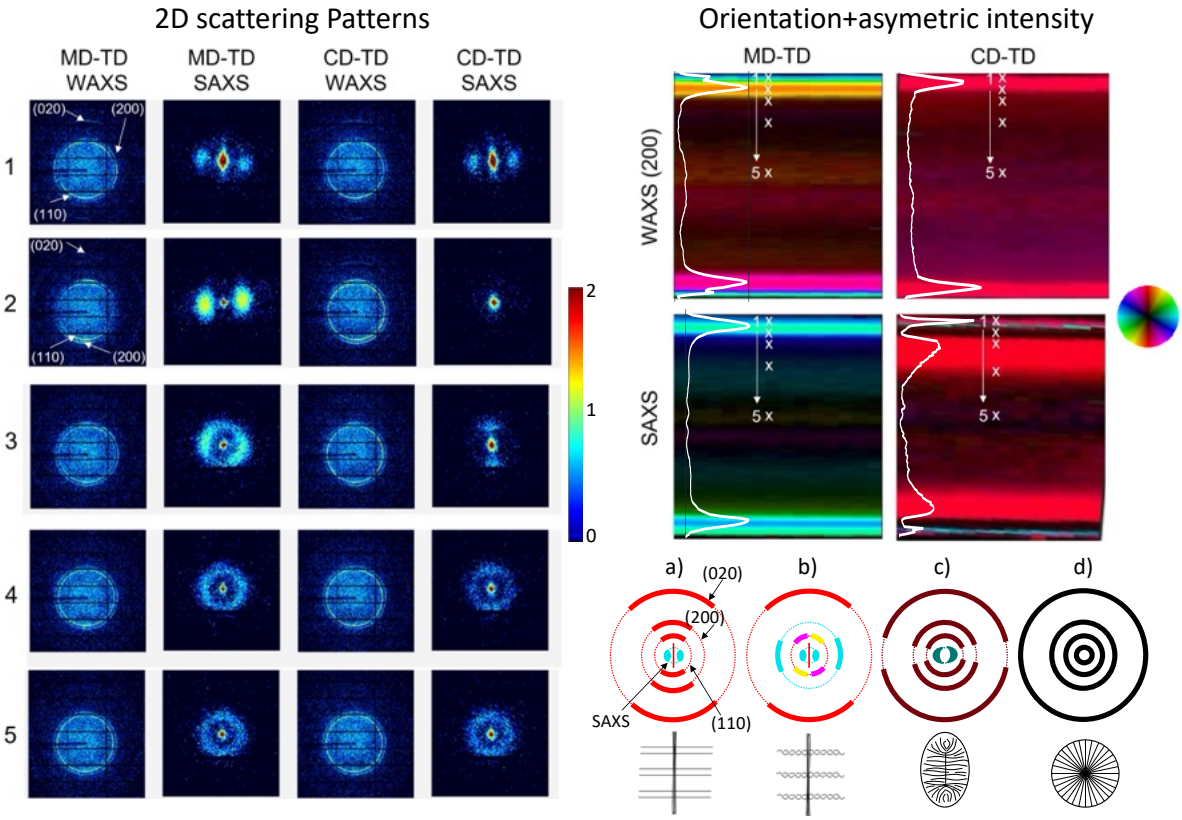

Figure 5.9. Scanning SAXS and WAXS 2D scattering patterns in five different positions (left) and orientation + asymmetric intensity (right top) of cross-sections from samples produced with process settings High 85% as well as idealized scattering patterns of polyethylene in MD-TD direction (right bottom). The idealized scattering patterns correspond from left to right a) shish-kebab with untwisted lamellae b) shish-kebab with twisted lamellae, c) elongated spherulites and d) symmetrical spherulites. In the orientation + asymmetric intensity plots as well as in the idealized scattering patterns, the hue represents the scattering orientation, and the value shows the asymmetric intensity. The white profiles in the orientation + asymmetric intensity plots show the asymmetric intensity through the thickness. The crosses in the orientation + asymmetric intensity plots indicate the position of the 2D scattering patterns (1-5). The scattering patterns reveal shish-kebab with twisted lamellae (Keller-Machine Type I) in layer 1, shish-kebab with untwisted lamellae (Keller-Machine Type II) in layer 2, a highly oriented crystalline morphology in layer 3, elongated spherulites in layer 4, and symmetrical spherulites in layer 5.Type I) in layer 1, shish-kebab with untwisted lamellae (Keller-Machine Type II) in layer 2, a highly oriented crystalline morphology in layer 3, elongated spherulites in layer 4, and symmetrical spherulites in layer 5.

5.2.4 Correlating structures with material and processing in polyethylene

To further evaluate and compare how choice of material, distance to injection gate and process settings impacts the multilayered morphology, the scattering signal of scanning SAXS and WAXS was evaluated throughout the thickness of injection molded plates (Figure 5.10). By utilizing the highly focused beam and high flux provided at the synchrotron, small differences of the layered morphology could be evaluated.

In LDPE, the focus was evaluating differences of varying viscosities of the polymer, and in position of the plate. Figure 5.10a shows that medium viscosity LDPE on average exhibit a higher degree of orientation than low viscosity LDPE. It was also seen that the distance between the injection gate and the measuring point had high impact on the structures formed, where a higher degree of orientation was found closest to the inlet of the mold (position 1).

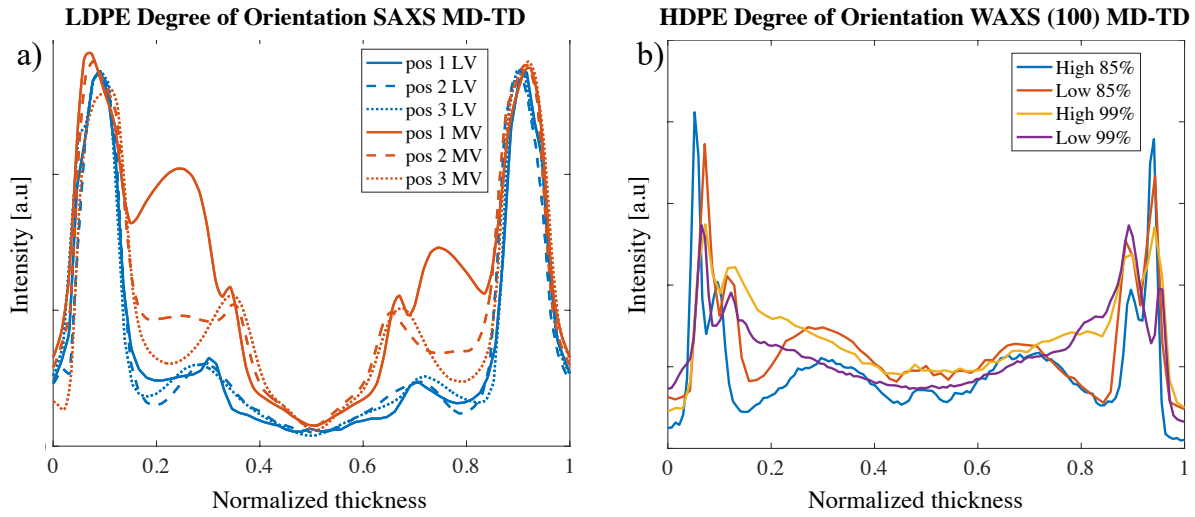

Figure 5.10. Degree of orientation calculated along a line through the thickness of a) SAXS of LDPE with varying viscosities and positions of the injection molded plate and b) HDPEs produces with different process settings.

For HDPE the influence of different processing settings was evaluated, where both difference in injection speed (high and low) and difference in the volume/pressure (V/P) switchover point was varied. The V/P switchover point is defined as the transition between the injection- and packing phase according to Figure 2.6, and in this study, we investigate samples where the switchover point occurred at either 85% or 99% filing of the cavity volume. Figure 5.10b shows that the V/P switchover point has a more significant influence on the layered morphology than the injection speed, in particular in the highly oriented layers close to the injection mold.

The difference between low and medium viscosity LDPE was further compared by using the 1D correlation function analysis described in section 3.4.3, to calculate the crystallinity and lamellae thickness (Figure 5.11). The results showed that the skin layers consisting of shish-kebab structures had a significantly higher degree of crystallinity as well as a higher lamellae thickness compared to the shear- and bulk layers, for both low and medium viscosity LDPE. Overall, the medium viscosity LDPE had slightly thicker lamellae compared to low viscosity LDPE. When investigating the effect of the positions within the injection molded plate, no statistically significant difference could be found in lamellae thickness between the different positions, despite the differences observed in the degree of orientation (Figure 5.10 a).

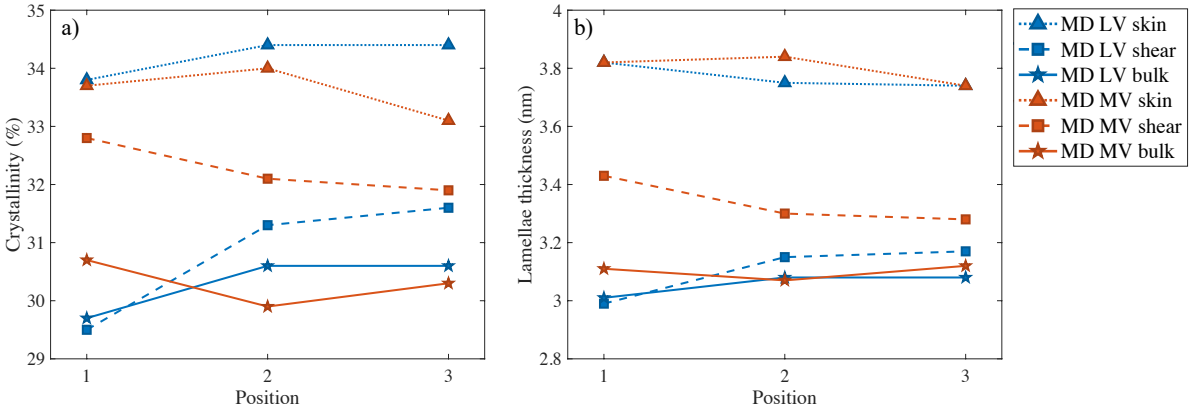

Figure 5.11. Crystallinity (a) and lamellae thickness (b) calculated for low and medium viscosity polyethylene for different layers across the thickness as well as different positions of the injection molded plate.

In the case of HDPE, the different processing settings were further compared by spatially resolving the *d*-spacing obtained from peak fitting of Lorentz corrected SAXS radially integrated curves, according to Figure 5.3. The peak position corresponds to the average lamellae spacing, which is the distance d_{ac} that includes one crystalline and one amorphous layer and the results are shown in Figure 5.12. The peak fit revealed that in layer 2, consisting of shish-kebab with untwisted lamellae, as well as in layer 5, consisting of symmetric spherulites, the lamellae spacing was significantly larger for low injection speed compared to the high injection speed. Furthermore, the lamellae spacing was larger for samples prepared with the 99% V/P switch-over point compared to the 85% V/P-switch-over point.

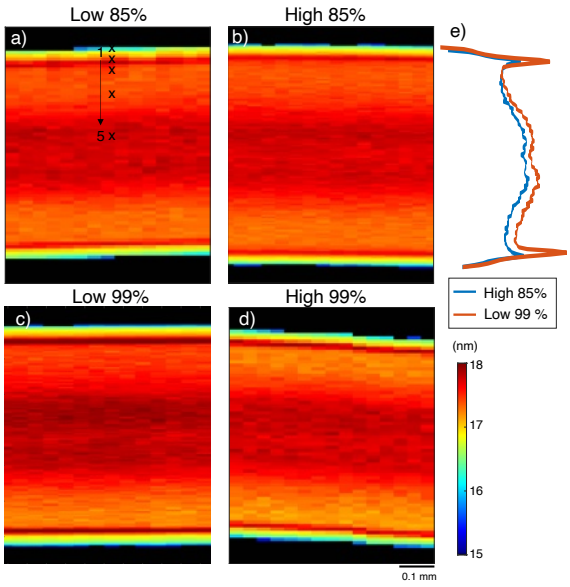

Figure 5.12. Peak fitting from SAXS data in MD-TD plane of a sample produced with process setting High 85% (a), Low 85% (b), High 99% (c), and Low 99% (d), where the d-spacing from the 2π/peak position is shown. Figure 5.12 e) show how the peak position that was found through peak fitting varied through the thickness for the process settings High 85% and Low 99%.

5.2.5 Correlating structures with material and processing in dialcohol cellulose

Dialcohol cellulose was studied either as a part of a composite with EAA (Paper III) or as a pure material (Paper IV). Figure 5.13 shows the spatially resolved WAXS symmetric scattering intensity and degree of orientation of the dialcohol cellulose and EAA composites containing 10 wt.%, 30 wt.% and 50 wt.% DALC fibers. The scattering intensity of the (020) diffraction peak of EAA and the (110) diffraction peak of cellulose, (Figure 5.13a-f), were used to analyze the distribution of cellulose fibers across the injection molded samples, according to Figure 5.2. For all fiber compositions, the symmetric intensity shows a homogeneous profile across the sample cross-section, with no indication of a layered structure. This suggests that the cellulose is well dispersed and uniformly distributed in the EAA matrix.

In contrast, the degree of orientation plots (Figure 5.13g–l) show a layered structure with increased degree of orientation close to the edges, in particular for the EAA peak, as expected from the injection molding process. Analysis of the EAA (020) peak (Figure 5.13a–c) shows that samples with lower cellulose content exhibit a higher degree of orientation. This trend is consistent with a strong interaction between EAA and the modified cellulose, which restricts EAA chain mobility and hinders its ability to form oriented structures. Notably, the oriented shear layers near the sample edges are broader when the fiber concentration is low, further indicating that cellulose disrupts the EAA ordering.

The degree of orientation calculations for the cellulose (110)-peak (Figure 5.13d–f) show the opposite trend where the cellulose has a higher degree of orientation in samples with high amounts of cellulose. This suggests that cellulose can more easily form ordered structures at high concentration, likely due to increased viscosity and stronger shear forces during molding. This result is also in line with a strong interaction between EAA and modified cellulose, which on one hand hinders the EAA orientation, on the other hand at low EAA concentration it serves just as a plasticizer, allowing the modified cellulose to align more easily in the direction of the flow (under stronger shear forces). Figure 5.13l shows that at high fiber concentrations, there is a high degree of orientation of the cellulose through most of the sample, except for a thin unoriented core layer.

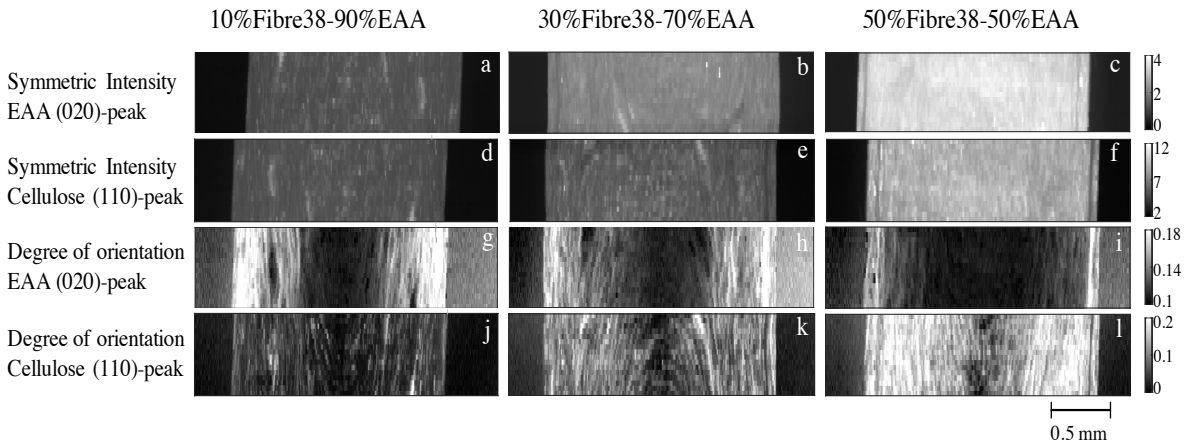

Figure 5.13. Scanning WAXS intensities of 10% Fiber 38-90% EAA, 30% Fiber 38-70% EAA and 50% Fiber 38-50% EAA, a–c) symmetric intensity of the EAA (020)-peak, d–f) symmetric intensity of the cellulose (110)-peak, g–i) degree of orientation calculated for the EAA (020)-peak, j–l) degree of orientation calculated for the cellulose (110)-peak

In addition, fiber composites with 30% EAA and 70% fiber were measured with scanning WAXS for fibers with three different degrees of modifications (DOM) (Fiber 32, Fiber 46 and Fiber 55) to investigate how the degree of modification influences homogeneity and degree of orientation, as shown in Figure 5.14. For all samples, the intensity showed a homogeneous distribution of cellulose across each sample cross-section (Figure 5.14a–f), indicating that the mixing is not affected by the degree of modification of the cellulose. The degree of orientation calculations for EAA peak (Figure 5.14g–i) show a similar degree of orientation profile across the set of samples investigated. This indicates that the modification of cellulose has a little influence of the degree of orientation of the EAA. The right side of the 70% Fiber 32-30% EAA sample was deformed during the sample preparation, causing deviating results. Degree of orientation plots for the cellulose peak (Figure 5.14j–l) show that the degree of orientation of cellulose is higher when the degree of modification is low. This implies that the orientation of the cellulose is lost as the material is modified.

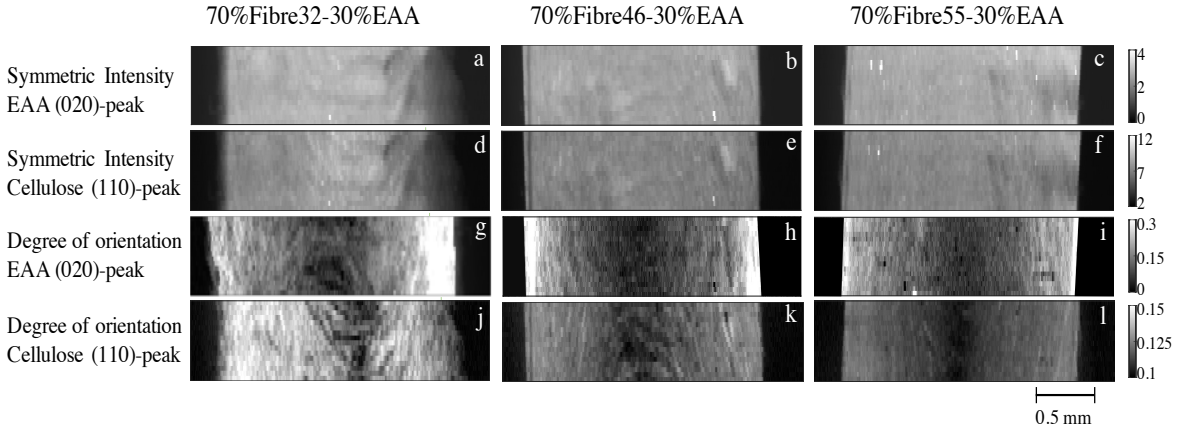

Figure 5.14. Results from scanning WAXS measurements of 70% Fiber 32-30% EAA, 70% Fiber 46-30% EAA and 70% Fiber 55-30% EAA showing a–c) symmetric intensity of the EAA (020)-peak, d-f) symmetric intensity calculated for the cellulose (110)-peak, g-i) degree of orientation calculated for the EAA (020)-peak, j-l) degree of orientation calculated for the cellulose (110)-peak

In injection molded pure dialcohol cellulose, similar profiles of the degree of orientation are found. Results for two different degrees of modifications (44% and 51%) are shown in Figure 5.15. Similar to the composite material, a higher degree of orientation is found in samples where the degree of modification is low. To investigate the role of water during processing, samples were prepared with two different initial water contents (30 wt.% and 40 wt.%) prior to compounding, which correspond to samples S3, S4, S6 and S7 according to Figure 4.1. For 44% DOM, the shear layer observed was thicker and the bulk layer had a higher degree of orientation when having 40 wt.% water content (Figure 5.15a, b) compared to 30 wt.% water content (Figure 5.15e, f). The higher initial water content is expected to lower the viscosity of the material, which will allow for an increased alignment within the flow direction during the injection molding.

The orientation effects observed as a function of both the degree of modification and initial water content prior to compounding can further be attributed to the effect of fiber breakage. Cellulose fibers are susceptible to breakage both during chemical modification to DALC and during processing steps such as compounding and injection molding. In samples with longer intact fibers, it is expected that the material responds more effectively to shear forces by aligning with the flow, while shorter fragments are expected to be more randomly oriented. Our results indicate that a low degree of modification, as well as having a high initial water content, plays a crucial role in mitigating damage to the fibers. This is also indicated by having the sample with the lowest degree of modification and highest water content resulting in the highest fibril alignment with the flow (Figure 5.15a-b).

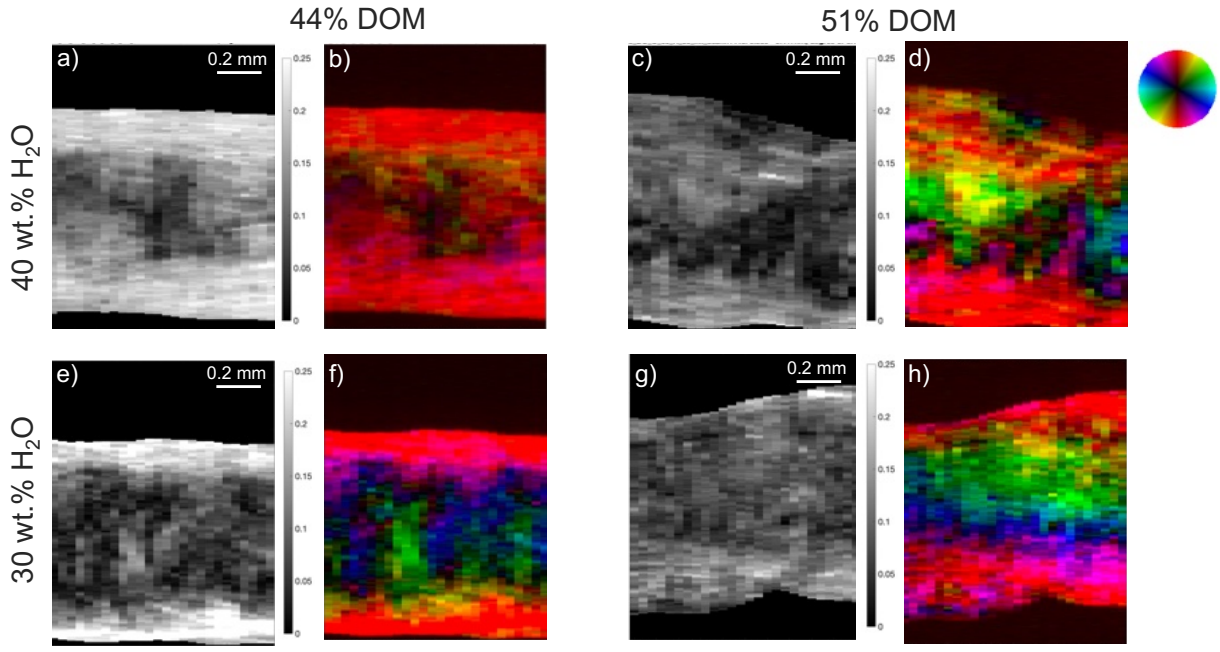

Figure 5.15 Scanning WAXS of the 200-peak showing degree of orientation and asymmetric scattering maps of samples with different initial water contents (30 wt.% and 40 wt.%) and different degrees of modification (41% and 51%) corresponding to samples S3, S4, S6 and S7.

By using SAXS data, the effect of initial water content was further evaluated. Examples of radially integrated SAXS curves taken from the center of each sample are shown in Figure 5.16. The results show that the SAXS peak around 0.05 $Å^{-1}$ is more pronounced in the 51% degree of modification compared to 44% degree of modification. This could be due to the core-shell structure visualized in Figure 2.4, since previous work has shown that core-shell structure can lead to increased moisture sorption[157, 158], which typically gives a more pronounced peak in SAXS[113]. By using the peak fitting approach described in section 5.1.2, it was further revealed that for 51% DOM samples prepared with a higher water content of 40 wt.% water prior to compounding exhibited a SAXS peak that was shifted to lower q compared to the 30 wt.% water. The shift corresponded in real space to an average distance of 12.3 nm for 40 wt.% water compared to 12.0 nm for 30 wt.% water. This indicates that the presence of additional water during early processing stages causes irreversible swelling of the fibril network. This structural effect remained visible even after the final injection molding step, demonstrating that small differences in water content at the start of processing can have lasting consequences on the final material structure.

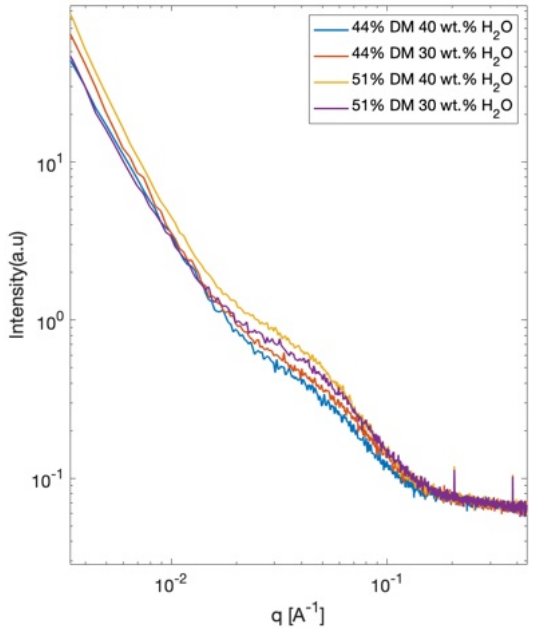

Figure 5.16. SAXS curves from the center of the samples with 44% and 51% degree of modification and 30 wt.% and 40 wt.% initial water content.

In a similar way, the influence of a drying and rehydration step prior to injection molding was investigated for pure dialcohol cellulose, corresponding to samples S4, S5, S7 and S8 according to Figure 4.1. Figure 5.17 show that samples processed without this intermediate drying step had more homogeneous fibril orientation profiles without a clear difference between the shear and bulk regions and where the main orientation was in the direction of the injection flow (Figure 5.17a-d). In contrast, the inclusion of a drying and rehydration step resulted in more random fibril orientations, in particular in the center of the injection molded plate. The results show that the inclusion of a drying and rehydration step significantly changes the fibril alignment during the following injection molding process. Furthermore, it was found that the degree of orientation and fibril center-to-center distance were decreased for samples with the additional drying and rehydration. One plausible

explanation is that the drying step causes partial compaction of fibrils. This can lead to a denser packing that is not fully reversed upon rehydration, which suggests irreversible structural rearrangements at the nanoscale.

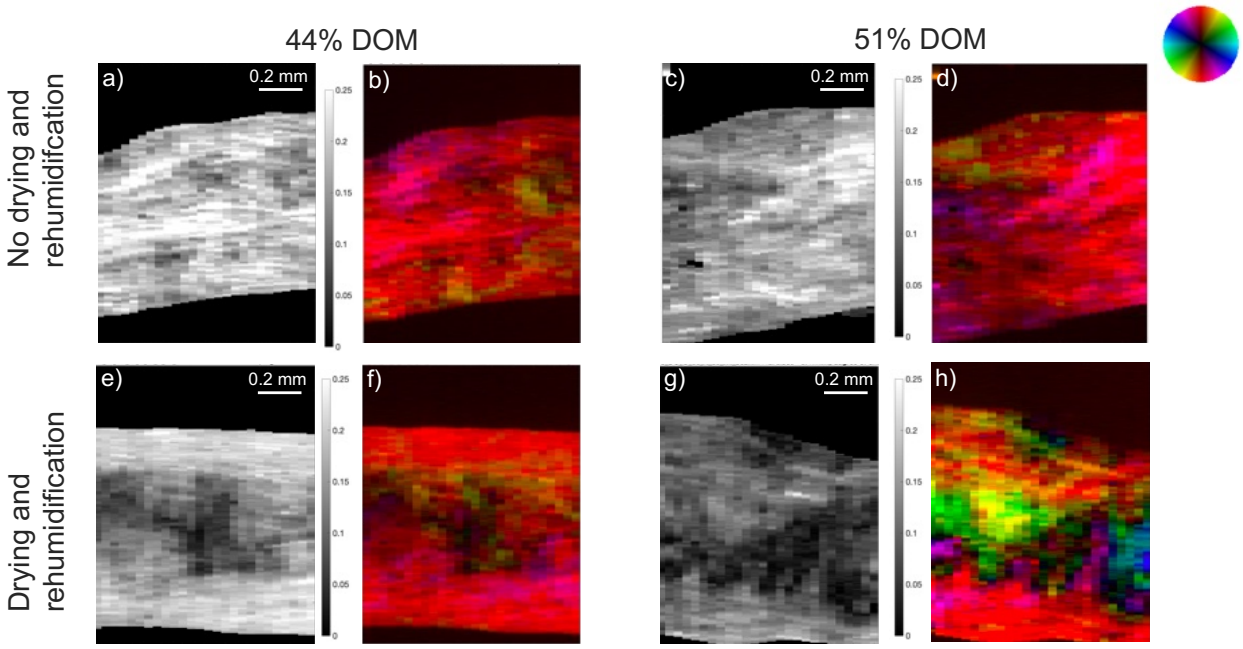

Figure 5.17. Scanning WAXS of the 200-peak showing degree of orientation and asymmetric scattering maps of samples with different initial water contents (30 wt.% and 40 wt.%) and different degrees of modification (41% and 51%) corresponding to samples S3, S4, S6 and S7.

5.2.6 Using scanning SAXS for commercially available packaging products

The injection molded samples produced for papers I-IV had a relatively simple geometry. However, in real packaging applications the products often have far more complex shapes, resulting in varying local processing conditions. Figure 5.18 shows results from a scanning SAXS measurement of a commercially available opening device made from medium viscosity LDPE studied in Paper I. Figure 5.18a shows an image of the opening device, where the red square indicates the sampling position. From the larger sample, a thin section was taken according to the red dashed line and measured in the through-thickness direction.

Figure 5.18b shows the average scattering orientation through the thickness over a larger area. It was determined that the average scattering direction varied from the top left corner (blue) to the bottom right corner (red), indicating a shifting orientation of the polymer structures. Furthermore, a region with deviating orientation was observed next to the screw thread (cyan). This is most likely a consequence of the screw thread changing the flow pattern, and consequently the average orientation of the polymer. In the through-thickness direction, Figure 5.18c, a layered structure was observed with the main scattering orientation in the vertical direction. In some parts of the sample, a skin layer was observed with main scattering in the horizontal orientation (red), where the scattering 2D patterns confirmed a shish-kebab microstructure.

Overall, the results highlight local polymer structures and orientations formed due to the intricate flow profile during injection molding in more complex shapes. Identifying regions with deviating orientations is of importance since it can be used to identify regions with varying mechanical performance that are more prone to breakage. Furthermore, the scattering can be used to identify if shish-kebab structures are present which has been reported to highly increase the mechanical performance in the direction of the fibril-like shish[33, 159, 160]

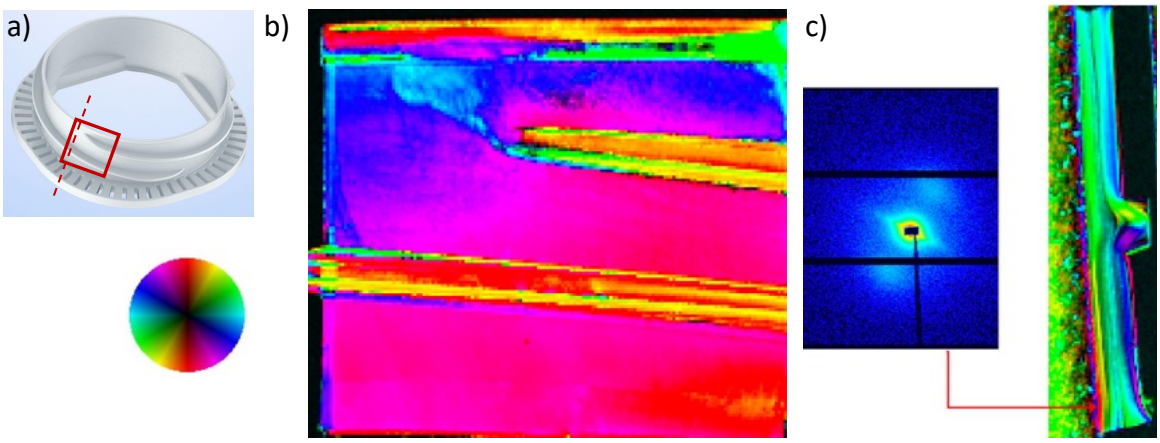

Figure 5.18. Scanning SAXS of a commercially available opening device made from pigmented medium viscosity LDPE.

5.2.7 Correlating structures with changing environment in commercial paper of drinking straw

In Paper V, scanning SAXS was employed to investigate how exposure to different liquid compositions influences the nanostructure of a commercial paper-based material used for paper drinking straws. Spatially resolved measurements were conducted across the soaking front after partial immersion of the samples in either water or orange juice (Figure 5.19). The SAXS data revealed that the degree of fibrillar swelling varied markedly depending on the liquid. When exposed to water, the scattering peak exhibited a pronounced shift, indicating a rapid and significant increase in the center-to-center distance between microfibrils. This behavior is consistent with strong water absorption and fibrillar separation. In contrast, immersion in orange juice led to a smaller peak shift and a more gradual change in intensity, suggesting a more limited and slower swelling process. These results highlight the sensitivity of cellulose nanostructures to the surrounding liquid environment, which is key in the paper straw application.

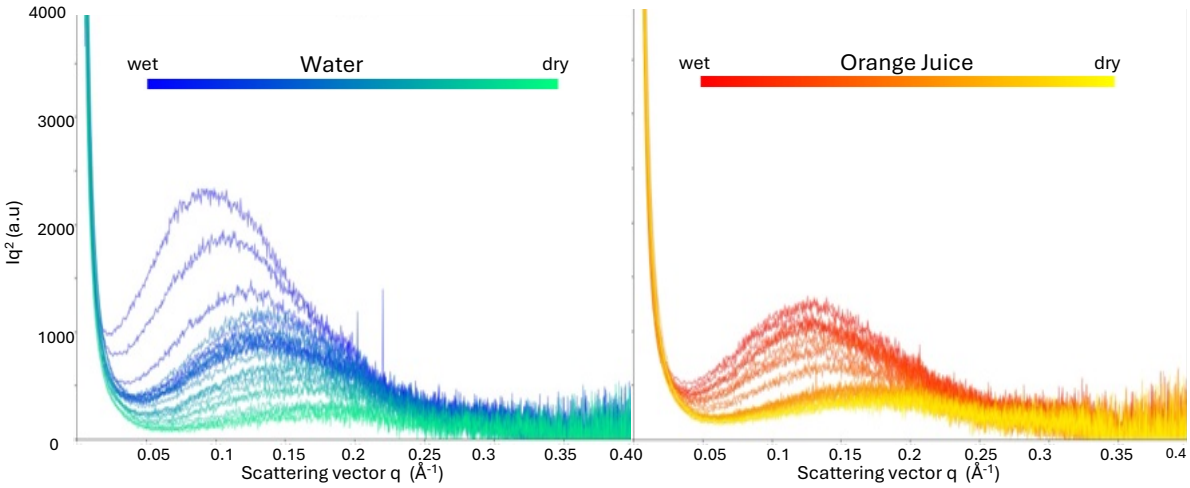

Figure 5.19. Spatially resolved SAXS measurements over the soaking front for samples immersed in either water or orange juice.

5.3 Combining scattering data with complementary methods

In the thesis, emphasis was put on how scanning SAXS and WAXS can be combined with complementary techniques to further understand the hierarchical structures of injection molded polymers. A summary with a few selected examples will be described in the section below, where more examples can be found in Paper I, Paper II, Paper III and Paper V including mechanical testing (Paper I and Paper III), birefringence measurements (Paper II), light optical microscopy (Paper II), DSC (Paper I and III), computational simulations (Paper I and II) and DVS (Paper V).

5.3.1 Mechanical Testing

Tensile testing was used to correlate the morphology to mechanical performance of the material. Stress-strain curves from the different viscosities of LDPE are shown in Figure 5.20, where orange curves correspond to low viscosity LDPE, blue curves correspond to medium viscosity LDPE and dots and crosses indicate the breakpoints for the 10 samples measured. Both low- and medium viscosity LDPE showed a higher ultimate strength in the machine direction (MD) compared to the cross direction (CD). The difference in material strength between MD and CD originates from the orientation of the highly oriented shish-kebab and elongated spherulite microstructures in the skin and shear layers of the sample, which were identified using scanning SAXS (Figure 5.8). The shish-kebab structure improves the tensile strength in the direction of the fibril-like shish structure[33, 159, 160], which explains the higher ultimate strength measured in MD. Compared to low viscosity LDPE, medium viscosity LDPE had a thicker skin layer as well as a more oriented and thicker shear layers, as shown in Figure 5.10a. The increased tensile strength and stiffness observed in medium viscosity LDPE compared to low viscosity LDPE can be explained by the difference in thickness of highly oriented layers.

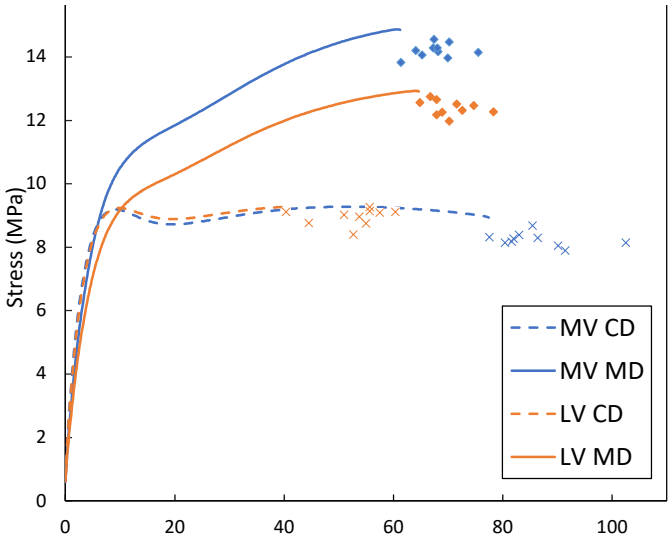

Figure 5.20 Stress Strain curves of LDPE with low (LV)- and medium viscosity (MV).

The structural morphology was further connected to the mechanical performance by measuring the deformed samples after tensile testing post-mortem with scanning SAXS (Figure 5.21). Measurements were performed for samples deformed in CD (Figure 5.21a-c) and MD (Figure 5.21d-f) both in top view where the average structure through all layers was measured and with side view where the structure of each layer was evaluated separately. The colors in the Figure 5.21 correspond to the preferred scattering direction where blue color indicates horizontally aligned scattering and red indicates vertically aligned scattering. In the CD direction, the dogbone sample showed clear necking, unlike the MD-deformed sample (Figure 5.21g). As a result, a larger region was selected for SAXS analysis in CD than in MD.

In the CD deformed sample, the undeformed region at the top shows horizontally aligned patterns (blue hue), indicating orientation along the flow direction. In contrast, after deformation, the lower part of the sample exhibits vertically aligned scattering patterns (red hue), which indicates that fibrillar structures reoriented along the tensile direction. In side view, the CD deformed samples further show that the orientation of the skin layer that consists of shish-kebab structures remains intact upon deformation, whereas the shear and bulk layers change their orientation upon deformation (Figure 5.21b). Furthermore, in the deformed region, the degree of orientation increases in the shear and bulk layers and the contrast between them decreases (Figure 5.21c). Thus, after deformation, the two layers have a similar microstructure, presumably consisting of fibrillar structures in the direction of the stress applied. These observations agree well with the results published by Guo et al[161] where crystalline segments, formed by slip of lamellae, beyond the yield point, reorient into the direction of the deformation. This is in agreement with previous work by Dashan et al[33] where it was hypothesized that the strong shish-kebab structure sustains most of the tensile forces, until cracks are formed in the skin layer, breaking the structure promptly.

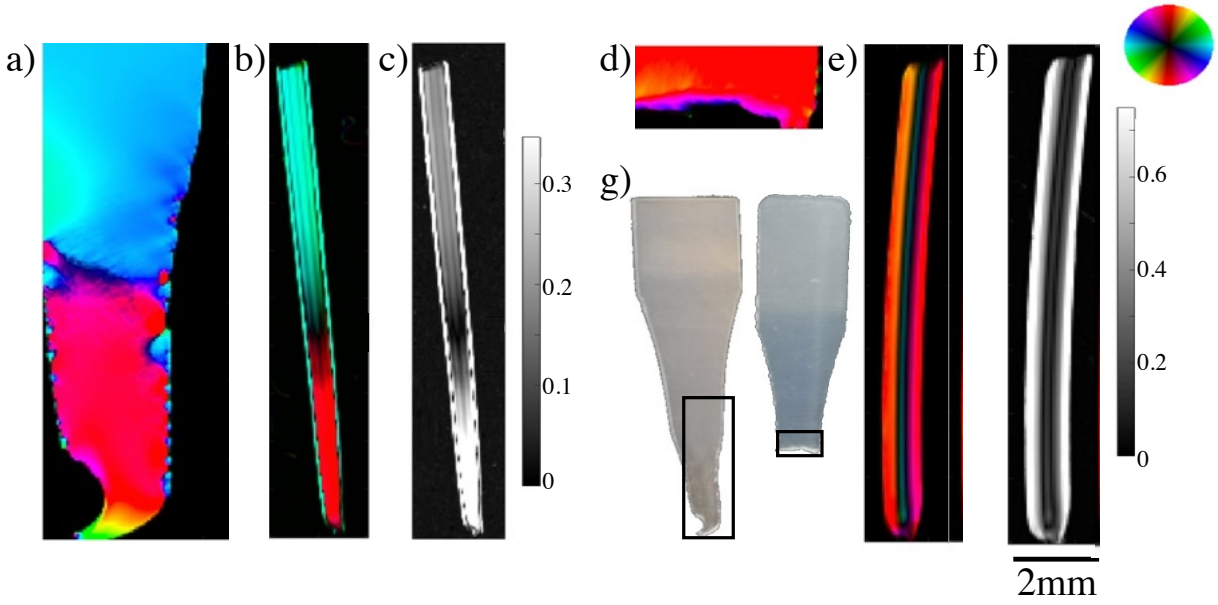

Figure 5.21. Scanning SAXS of a medium viscosity LDPE dogbone deformed in CD (a-c) and in MD (d-f), respectively. Asymmetric intensity plot in top view (a, d) and in side view (b, e) as well as degree of orientation in side view (c, f). Note the different scaling in the degree of orientation maps. For asymmetric intensity plots the hue corresponds to the orientation angle of the scattering, whereas the asymmetric scattering corresponds to the value of the color. Figure 5.21g shows photographs of the dogbone shaped samples deformed in CD (left) and MD (right). The black rectangles (g) indicate the regions that were measured with scanning SAXS top view (a, d).

A peak fitting analysis of the main SAXS peak was performed on the deformed sample in CD direction to evaluate how the distance d_{ac} of one crystalline and one amorphous layer varied across the samples (Figure 5.22). The undeformed part of the sample at the top (blue position) had a narrower peak width, indicating a low dispersity, and a larger distance d_{ac} compared to the deformed parts of the sample.

Moving towards the fracture surface, a combination of decreased peak intensity, broadening of the peak and decrease of the distance d_{ac} was observed. This suggests that when deformation starts, large structures are first disrupted to create new smaller structures. Even closer to the fracture position (yellow and purple position) the peak width starts to decrease again, and the long period further decreases. This indicates that increasing amounts of the large structures are disrupted, giving rise to structures with smaller relatively defined long-distance spacing.

In addition, the radially integrated data (Figure 5.22e) shows that the peak intensity consistently decreases closer to the fracture position, consistent with having a decreasing amount of crystalline structures present. Thus, our results suggest that when the sample is being deformed in CD, large structures break apart into smaller structures simultaneously as they reorient in the direction of the applied stress.

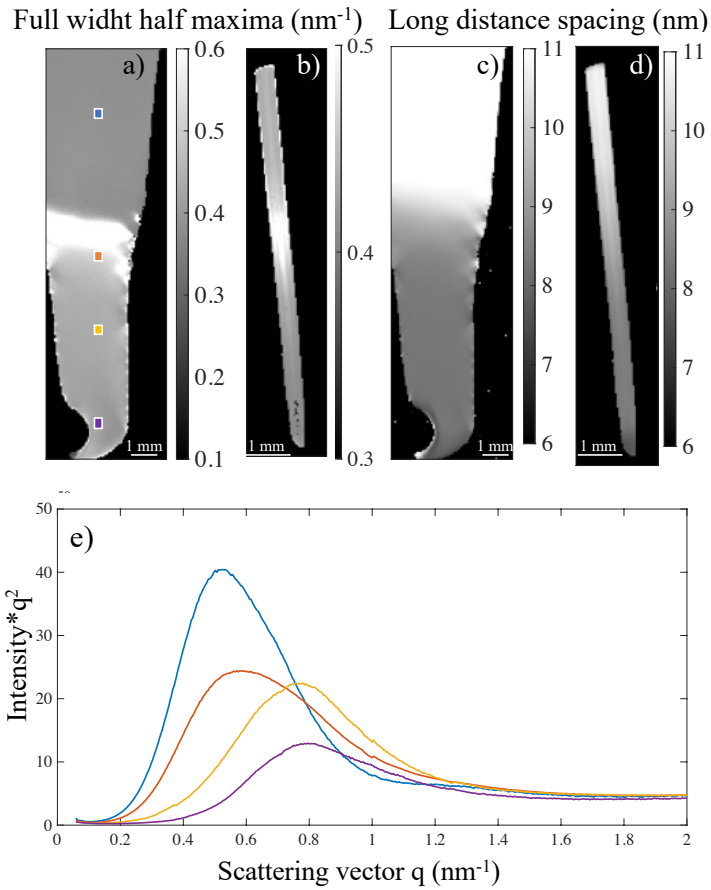

Figure 5.22. Results from peak fitting of scanning SAXS data of medium viscosity dogbones deformed in CD (a-d) as well as azimuthally integrated data for some selected points (e). (a) and (b) show the calculated full width at half maximum of the peak across the top view and side view sample respectively, whereas (c) and (d) show the 2*π/(peak position), corresponding to the length of the full-period d-spacing.

5.3.2 Birefringence Microscopy

High density polyethylene produced with different process settings was studied using both birefringence microscopy (Figure 5.23) and scanning SAXS/WAXS (Figure 5.24) to further evaluate how process conditions influence the layered morphology. Differences between the process settings were observed both in the skin and in the shear layers.

As previously described, the skin layers consist of shish-kebab structures. In contrast to the birefringence and SAXS data, WAXS data is needed to resolve if the shish-kebab structures have twisted or untwisted lamellae. By having access to the WAXS data, an indication of thicker shish-kebab layer with untwisted lamellae (layer 2) was observed for the settings using a V/P switch-over point of Low 85% compared to 99%, seen with the yellow/orange (upper) and purple (lower) color in the WAXS (200) asymmetric intensity in MD-TD (Figure 5.24a, e in comparison with Figure 5.24c, g).

The main difference observed between process settings was the presence of the thick layer of highly oriented crystalline morphology, which can be seen as red layers both in the birefringence and in the SAXS CD-TD data. This layer was present in the samples produced

with 85% V/P switch-over point (Figure 5.23a, c and 5.24 b, f), while not being present at all in the samples produced with 99% switch-over point (Figure 5.23b, d and 5.24d, h). The thickness of this highly oriented crystalline morphology layer was different in the upper- and lower part of the sample, which most likely originated from the different mold materials in the two mold halves, giving rise to different cooling rates on the two sides of the cavity.

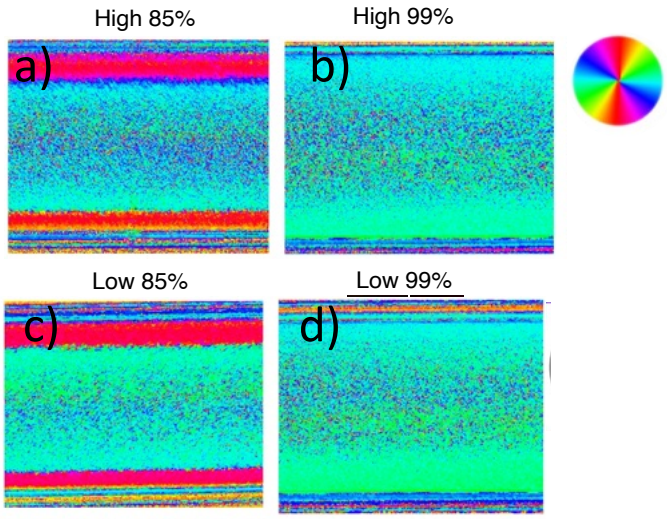

Figure 5.23. The angle of fast axis measured with birefringence microscopy for a) HDPE High 85%, b) HDPE High 99%, c) HDPE Low 85%, and d) HDPE Low 99%.

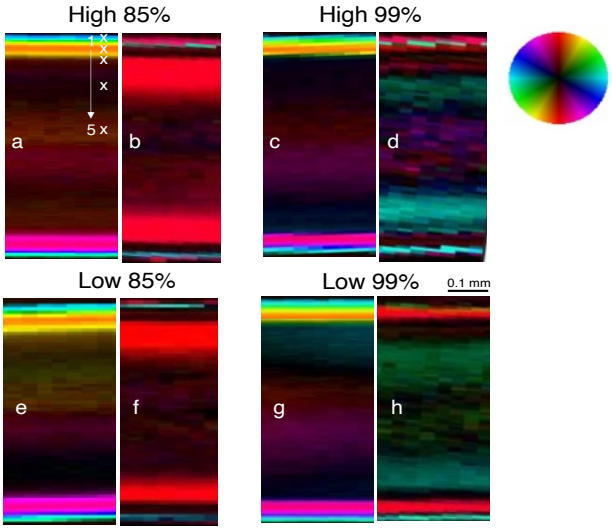

Figure 5.24. Scanning SAXS and WAXS (200) orientation + asymmetric intensity through the thickness of cross-sections from samples produced with varying process settings. Cross-sections to the left of each pair (a, c, e, and g) represent WAXS (200) MD-TD and cross-sections to the right of each pair (b, d, f, and h) represent SAXS CD-TD.

Overall, a good agreement was found between SAXS and birefringence results. Correlating scattering results with birefringence is of importance from an industrial point of view since birefringence microscopy is more available and requires less data analysis compared to scanning SAXS and WAXS. Furthermore, birefringence measurements provide higher

spatial resolution, allowing resolution of finer layers. However, the birefringence measurements by themselves do not provide enough information to define the hierarchical structures present, making the two techniques complementary to each other.

5.3.3 Computational simulations

In Paper I-II, computational simulations were combined with the scattering data to gain insights on the formation of hierarchical structures in polyethylene. The simulations presented in this chapter were performed by Renan Melhado Mazza. My contributions were to be deeply involved in the interpretation of the simulation results and linking the computational results to the experimental data.

In Paper I, the scattering data from LDPE was compared to finite element simulations, where the temperature- and shear profiles over time were simulated for low- and medium viscosity LDPE (Figure 5.25). The formation of different hierarchical structures through the thickness can be correlated to the shear and temperature profiles in different steps of the injection process. The blue temperature region represents polymer temperatures below 120 °C, allowing for comparison between crystallization under quiescent conditions at 100 °C and flow-induced crystallization at higher temperatures under shear[162].

As shown by the temperature profiles, the skin layers (corresponding to positions A1, A2, B1, and B2 in Figure 5.8) are formed almost immediately when the flow reaches the cold mold. The cooling rate is very high, causing the polymers to solidify almost instantaneously while having high shear stresses. This induces high orientation in the polymer, providing the right conditions to form the fiber-like core in the shish-kebab structures, as identified by the scattering data. Furthermore, the induced orientation is believed to contribute to the higher crystallinity and thicker lamellae observed in the 1D correlation function analysis (Figure 5.11).

In the shear layer, (Figure 5.8 positions A3 and B3), the temperature is increased due to friction from increased shear forces in the injection phase. Thus, this layer will not crystallize until the packing phase, where the shear rate is lower. Consequently, a lower degree of orientation is expected compared to skin layers 1 and 2. This agrees with the scattering data, which shows that these layers consist of elongated spherulites.

Comparing low and medium viscosity LDPE, the temperature when entering the holding pressure phase is higher in the medium viscosity LDPE due to more shear-induced heat during the injection phase. However, the medium viscosity LDPE has a lower specific heat, resulting in a faster cooling rate. Combined with a higher shear rate and a longer relaxation time for the longer molecules, the induced orientation during the high shear injection phase is more prone to remain before crystallization occurs, resulting in a more anisotropic microstructure. This agrees with the scattering data, that showed a thicker shear layer with a higher degree of orientation in medium viscosity LDPE compared to low viscosity LDPE.

In the bulk layer, the crystallization is slower in the low viscosity LDPE than in the medium viscosity LDPE due to the difference in specific heat. This gives more time to the polymer chains to relax, which gives a thicker layer of symmetric spherulites.

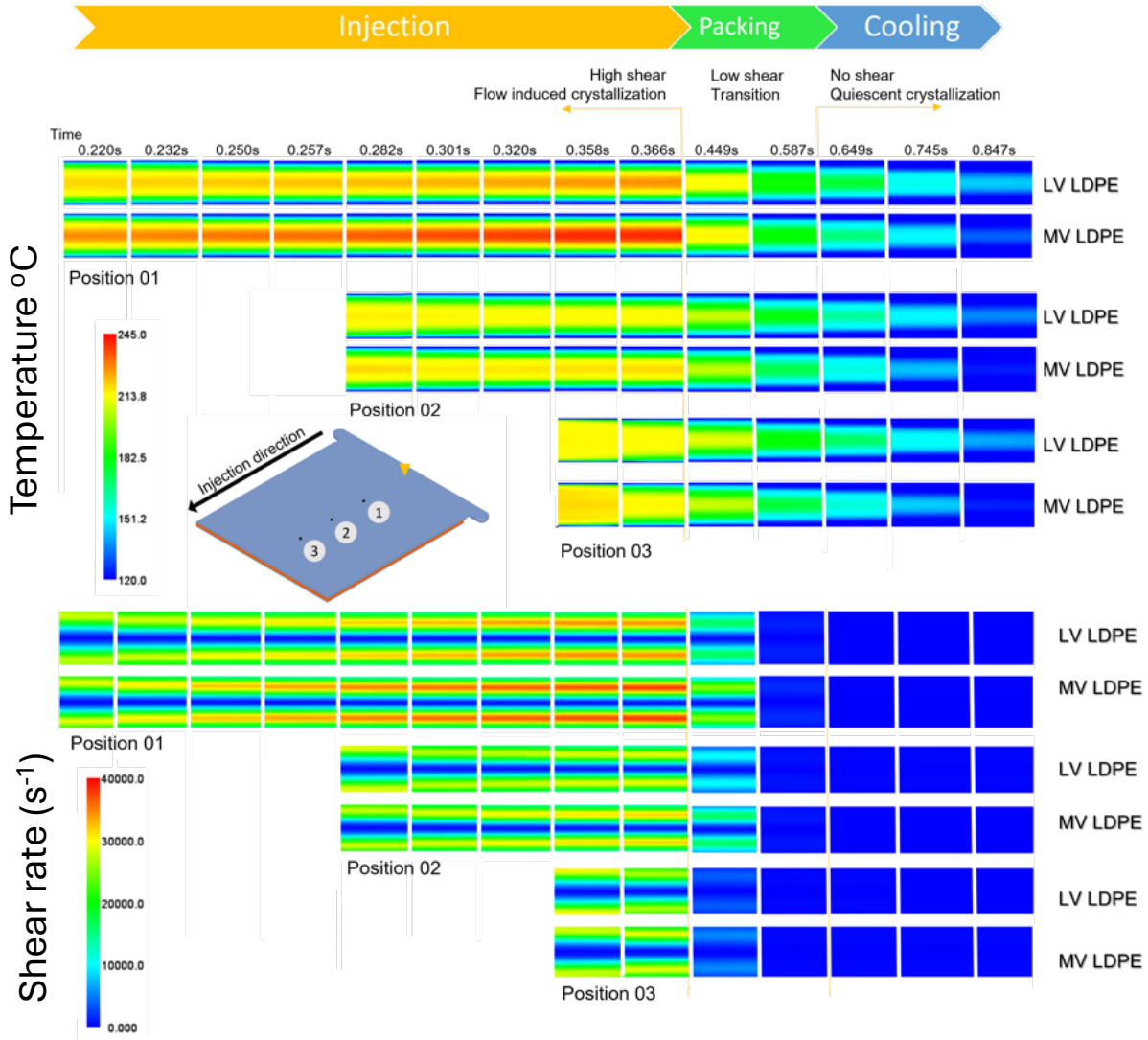

Figure 5.25. Simulation results of temperature- (top) and shear rate profiles (bottom) of low- and medium viscosity LDPE during injection, packing and cooling. Observe that the time scale is non-linear.

In a similar way to low density polyethylene, shear rate and temperature profiles were simulated for high density polyethylene in Paper II, see Figure 5.26. The simulations were performed in each of the layers defined in Figure 5.9 and were used to understand the structural differences observed when comparing the morphology profiles of the different process settings shown in Figure 5.10b and 5.12.

The simulation shows that the shear rate drops in the holding phase and occurs under significantly different pressure in samples with 99% compared to 85% V/P switch-over. As reported by Zhang et al. an increased pressure during processing is linked to a higher formation of the shish-kebab morphology[163]. The pressure history can thereby be a main

contributor to the thicker layer 2 observed in samples produced with the 85% V/P switch-over point in comparison with 99% V/P switch-over point, as shown in orientation + asymmetric intensity in SAXS and WAXS (Figure 5.9).

The simulations further show that the shear rate is lower and the time duration under shear is longer for low injection speed in comparison with high speed. This could possibly give fewer nucleation sites for kebabs on the shish precursors, which could explain the longer d-spacing between the kebabs for samples produced with low injection speed in comparison with high speed, as shown in Figure 5.12.

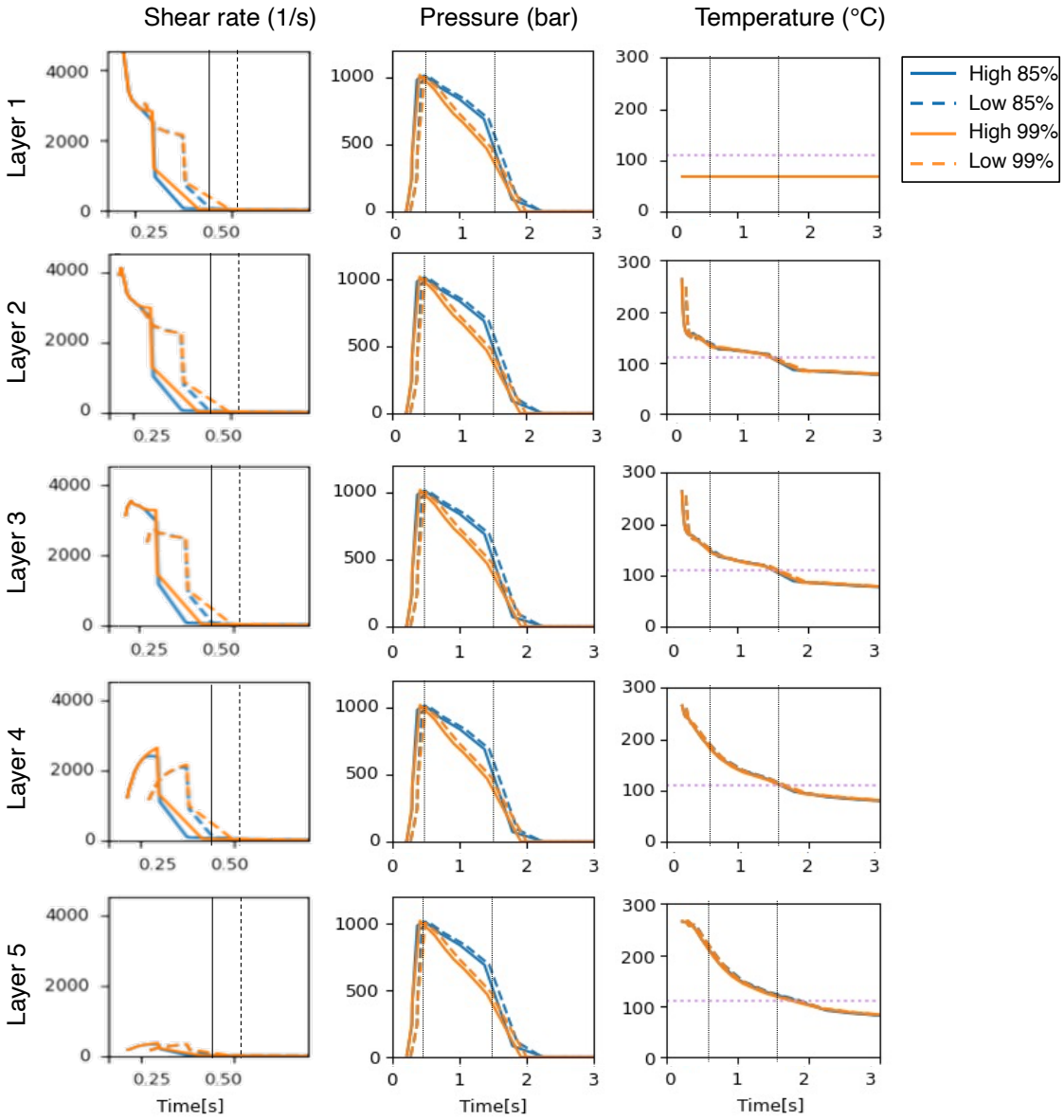

Figure 5.26. Selected results from finite element simulations: shear rate (left), pressure (center), and temperature (right), in five different layers through the thickness, where layers 1 to 5 represent different depth from the mold wall, i.e., 0.00, 0.03, 0.06, 0.15, and 0.27 mm. These depths were chosen to represent the same layers reported in Figure 5.9. Note that the x-axis, i.e., the time, was chosen differently for the three parameters. Horizontal purple dotted lines represent the quiescent crystallization temperature of 117 °C. The vertical black lines indicate the transition between injection phase and the hold phase (~0.5 s) and the transition between the hold phase and cooling phase (~1.5 s).

Comparing the different V/P switch-over points, the simulations revealed that the 99% setting had a significantly lower pressure compared to the 85%. Thus, the crystallization was expected to occur under higher pressure for the samples produced with the 85% switch-over point. This result agrees with the differences identified in SAXS/WAXS (Figure 5.24) and birefringence (Figure 5.23), where the highly oriented crystalline morphology was present only when using the 85% V/P switch-over point. Furthermore, the lower pressure in the 99% V/P switch-over point could be a possible explanation for the longer d-spacing between the kebabs observed in Figure 5.9.

Furthermore, in Paper II computational simulations were used to analyze the crystallization process of HDPE from an energy perspective by using specific work (Figure 5.27). The specific work w is defined according to Janeschitz-Kriegl et al.[164]

$$w = \int_0^{t_s} \eta\,[\dot{\gamma}(t)]\dot{\gamma}^2(t)dt \qquad \textit{Equation } 5.1$$

where t_s is the shearing time, η is the viscosity, $\dot{\gamma}$ is the shear rate. By using the specific work, a clear difference was observed between the 85% and 99% V/P switch-over points. In layer 1 and 2 consisting of shish-kebab structure, which corresponds to ranges 0-0.1 and 0.9-1.0 nominal thickness, the specific work was significantly higher for the samples with 85% V/P switch-over point, than in those with 99% V/P switch-over point. The higher specific work could explain the difference in layer thickness of shish-kebab identified by birefringence and SAXS/WAXS (Figure 5.23 and 5.24). The highest levels of specific work were identified for High 85% and Low 85% in the approximate ranges of the thickness where highly oriented crystalline morphology were identified by SAXS/WAXS for the samples produced with these process settings.

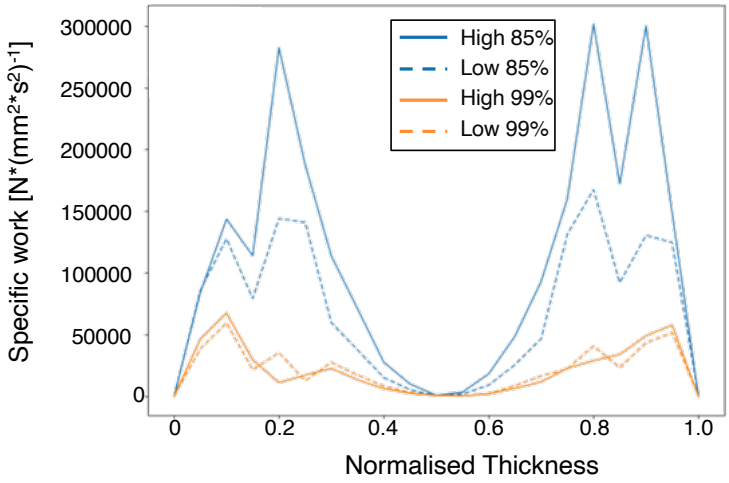

Figure 5.27. The calculated specific work as a function of the nominal thickness for four different process settings, i.e. high and low flow rate and V/P switch over at 85% and 99%, respectively.

5.3.4 Dynamic Vapor sorption

SAXS data of the commercial paper material used for drinking straws in Paper V was combined with dynamic vapor sorption (DVS) analysis to gain insights of the drying mechanisms of the material (Figure 5.28). The samples used for the SAXS measurements were initially preconditioned at high relative humidity (95% RH) and then allowed to dry under ambient conditions within the beamline hutch.

The DVS data revealed that water loss followed a typical exponential decay, where most of the moisture was released within the first few minutes after exposure to the low relative humidity environment. Similarly, the SAXS data showed an immediate and pronounced shift in the main scattering peak within the first three minutes of drying. This rapid shift corresponds to a significant decrease in the center-to-center distance between microfibrils, indicating rapid structural contraction in response to moisture loss. After the initial phase, the SAXS peak position gradually stabilized. The intensity of the SAXS peak exponentially decreased with time, which closely resembled the moisture loss profiles observed in the DVS measurements. This strong correlation suggests that the fibrillar network responds almost instantaneously to changes in moisture content, and that the structural evolution is tightly coupled to water removal kinetics.

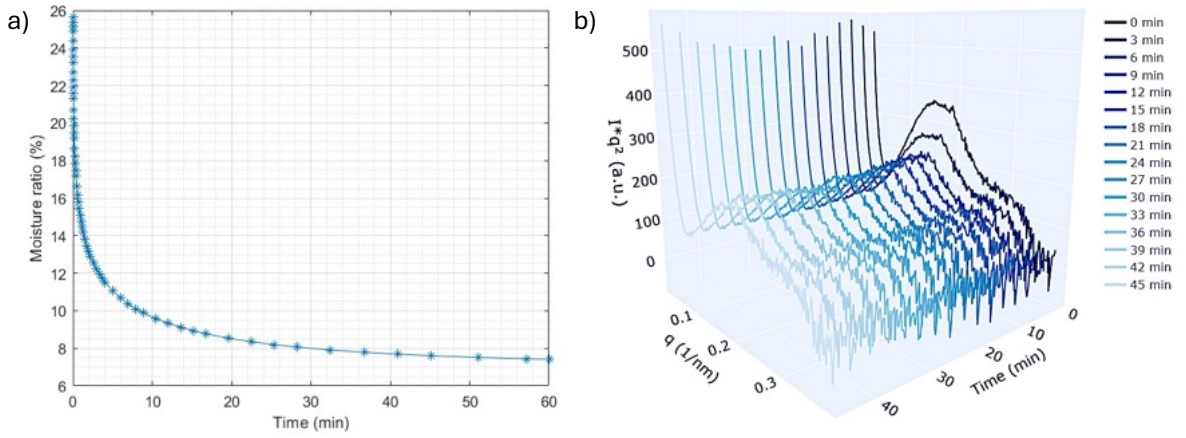

Figure 5.28. (a) Moisture loss calculated from the dynamic vapor sorption model, demonstrating correlation between microstructural reorganization and exponential desorption behavior. (b) Time-resolved SAXS patterns showing structural evolution of the base paper material during drying from 95% RH to ambient conditions.

5.4 Using STXM with NEXAFS contrast to study cellulose-based materials

In Paper VI, STXM with NEXAFS contrast around the carbon K-edge was used to probe the chemical content of cellulose fibers. Figure 5.29 shows an example of a STXM image of a single thermomechanical pulp fiber taken at 284.9, 286.2 and 330 eV. The sample was probed with a focused 30 nm beam with a step size of 30 nm. The first two energies correspond to the absorption of aromatic and phenolic carbons found in lignin, as described by Figure 3.3. For these energies, regions with high optical density values correspond to high lignin content. Consequently, the measurement can be used to map out the lignin distribution across the fiber. By comparing the two energies, it was found that there was a difference in the spatial intensity distribution between the two lignin peaks over the fiber. This can be related to a variation in the relative fraction of the monomers p-coumaryl, coniferyl, or sinapyl monomers which have different amounts of phenolic groups[99]. The image at 330 eV corresponds to the post edge of the NEXAFS spectra. At this energy, variations in optical density values are related to thickness variations across the fiber, as it is sensitive to the overall electron density.

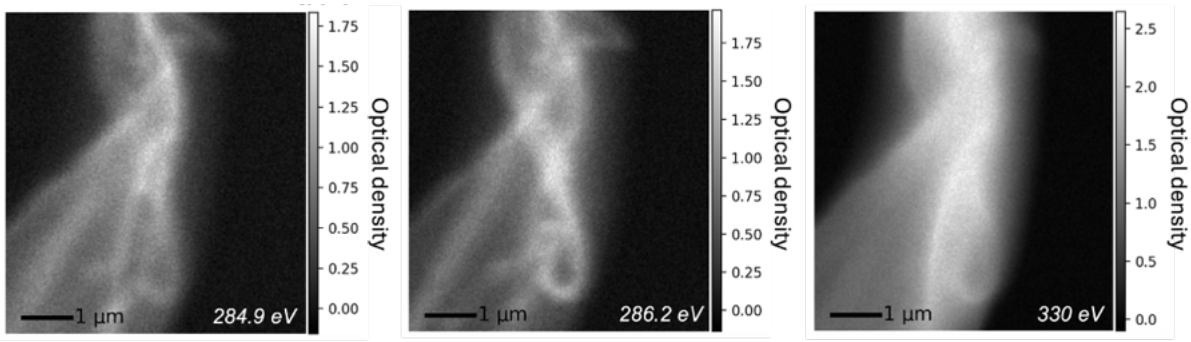

Figure 5.29. Images collected at the resonance energies for lignin (284.9 eV, 286.2 eV), and at the post-edge (330eV) which is sensitive to the electron density of the section and highlights the entire fiber.

As showcased in Figure 5.29, STXM coupled with NEXAFS contrast has high potential for chemical characterizations of a lignocellulosic fibers, due to the high chemical sensitivity and high spatial resolution. However, the technique currently presents many challenges. One key challenge is the demanding sample preparation of thin slices, which is required to ensure sufficient X-ray transmission through the sample. Cellulose-based samples typically require a sample thickness of 90-200 nm to provide optimal X-ray transmission. At this thickness, about 30-60% of the incident X-ray intensity is maintained, which gives high quality spectral data[98, 99]. In Paper VI, five different sample preparation approaches were tested for thermomechanical pulp and were tested in terms quality of the NEXAFS spectra, sensitivity to radiation dose and quality of the sample sectioning.

The resulting NEXAFS spectra for each of the sample preparation approaches are shown in Figure 5.30. When possible, NEXAFS spectra were collected both for the embedded sample (black) and for the embedding matrix (grey). The samples prepared by immersing fibers in

pure water and cutting in cryogenic conditions (Figure 5.30d) and by embedding fibers in Sulphur (Figure 5.30e), had embedding materials that do not contain any carbon atoms. Thereby, these spectra reflect the chemical composition of the thermomechanical pulp fiber, without any potential spectral contaminations from the embedding. The two aromatic peaks from the lignin at 284.9 eV and 286.2 eV are clearly visible and are comparably pronounced in the two samples. Similarly, the peak at 288.7 eV and the shape of the broad transition at 293 eV for C 1s→σ* transitions of aromatic and aliphatic carbons remained consistent.

In contrast, the resulting spectra from the other sample preparation approaches showed clear differences, which indicates spectral contaminations. This can arise if embedding material is partly present in the measured regions, since the resulting NEXAFS spectrum are a linear combination of the different components present. In the sucrose embedded fibers (Figure 5.30c), a lower relative intensity between the aromatic lignin peaks compared to the broad peak at 293 eV was found. The sucrose contributions give an indistinguishable contribution from the cellulose, explaining the stronger signal from saccharides relative to the lignin. A similar phenomenon was observed for fibers with the cycloamine based epoxy embedding (Figure 5.30b), where the spectrum also showed a lower relative signal from lignin. This can be explained by the contribution from the aliphatic carbon species in the embedding material. The highest spectral contamination was found for samples embedded in Spurr epoxy (Figure 5.30a), where the entire shape of the NEXAFS spectrum was modified due to the superposition of epoxy resonance peaks at ~284.8 and ~288 eV.

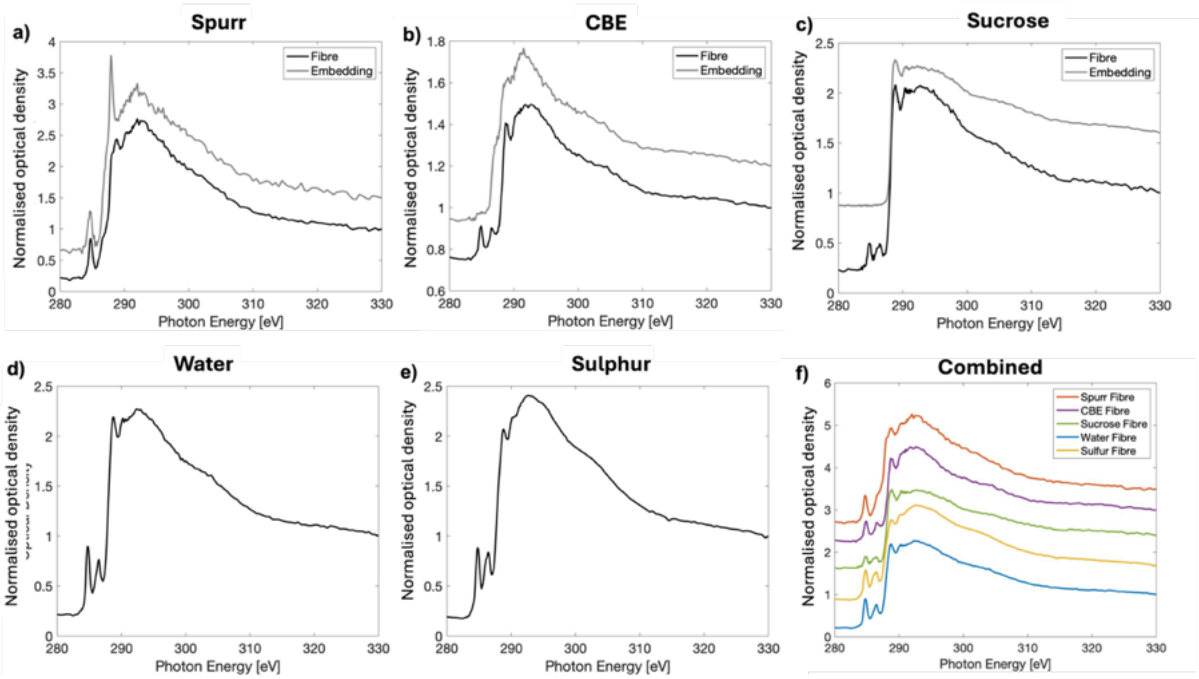

Figure 5.30. Spectra from embedded fibers and embedding materials prepared through the different sample preparation protocols (a-e). Spectra acquired from fibers (black) together with the reference of each embedding material (grey), offset for clarity. f) Normalized spectra from the fibers prepared through each preparation protocol. The spectra are offset for clarity.

Another key challenge when using STXM to characterize lignocellulosic fibers is radiation damage. The severity of radiation damage is increased by the radiation dose on the sample which is related to a high photon flux, long exposure times and a focused X-ray beam. The radiation damage is particularly severe around the carbon K-edge since the X-ray absorption is so high. The sensitivity for radiation damage may be affected by the sample preparation approach, as different embedding materials may react under the beam energy. Conductivity of the embedding material may also reduce static build-up which can help mitigate reactions in the samples after dose exposure.

Figure 5.31 shows radiation damage tests for each sample preparation approach, where the samples were repeatedly measured along a line of 50 points with an exposure time of 20 ms. In the case of epoxy-based sample preparation protocols, pure epoxy without any embedded fibers was also measured, shown as insets in Fig. 5.31b and 5.31e. The post edge energy at 330 eV, was used to evaluate mass loss or gain of carbon, where the water, cycloamine- and Spurr-based epoxy showed significant reduction. A small positive mass change of carbon was found in the Sulphur embedded samples, which indicates deposition of carbon-containing species from the surrounding atmosphere onto the sample. In the high-vacuum chamber outgassing can occur from both sample and material in the chamber which may lead to redeposition of evaporated material by the incident beam.

In addition, changes of relative intensity of different spectral peaks were observed because of radiation damage. These spectral changes can be linked to breakage or formation of different covalent bonds in the material. The results showed that three different covalent bonds were particularly sensitive to radiation damage, (1) the C 1s→1 π^* transition of the phenolic carbons at 286.5 eV, (2) the C 1s→1 π^* transition of carboxylic carbon at 288.7 eV and (3) the broad C 1s→σ^* transition of aromatic and aliphatic carbons at 293 eV.

At 286.5 eV, the peak intensity increases with exposure time across all sample preparation methods, except for the Spurr epoxy, where the peak could not be resolved due to spectral overlap. In contrast, peak intensities at 288.7 eV decrease for all samples, consistent with previous findings showing that radiation exposure leads to chain scissoring of the C=O bonds and formation of C=C bonds[165]. The Spurr-embedded sample showed a significant decrease in peak intensity at both 288.7 eV and 283 eV. The spectral changes are likely due to a combination of damage to the fiber as well as damage to the embedding material as the neat Spurr embedding (Fig. 5.31e, inset) have a strong peak at 288.7 eV from its carboxylic carbon groups that disappears between the first and second 20 ms exposure. The cycloamine-based epoxy shows smaller spectral changes compared to other approaches, suggesting a greater radiation resistance. Tests on the pure cycloamine epoxy confirm its relative stability compared to Spurr. The spectral changes in the sucrose sample protocol of the peaks at 288.7 and 293 eV are relatively small while a clear decrease in the peak at 286.5 eV is seen. We believe that this is due to that sucrose has a large spectral overlap with the fibers at these energies and that sucrose is less sensitive to radiation damage compared to the fibers.

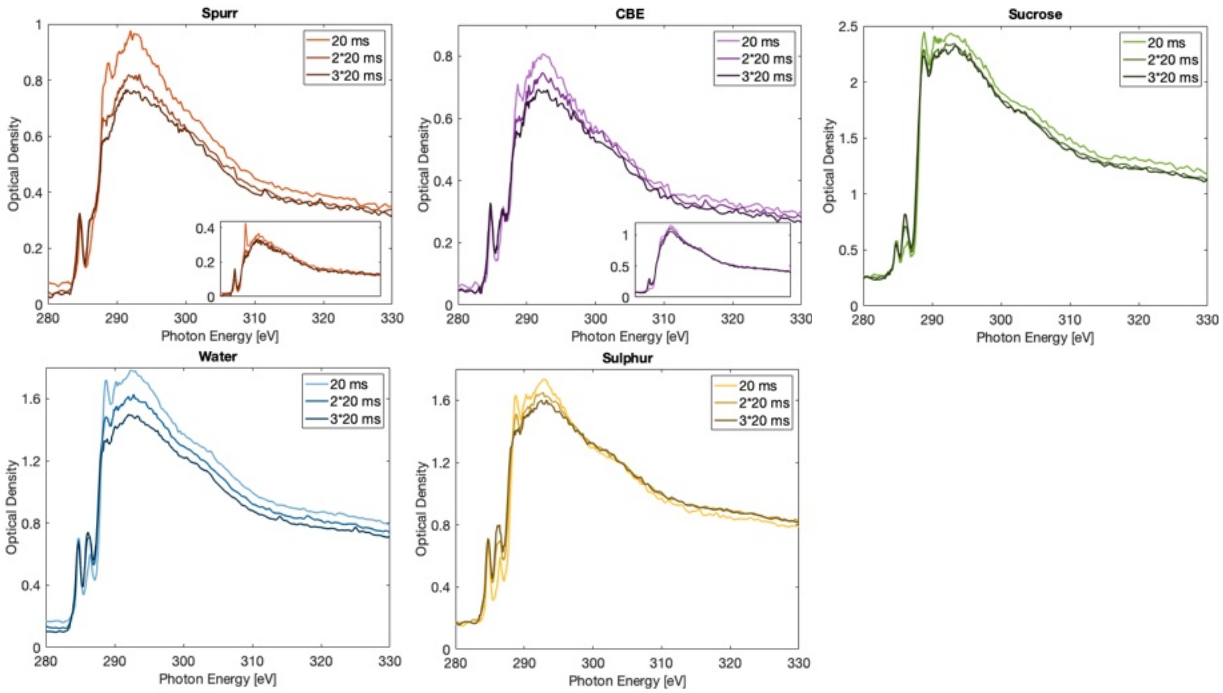

Figure 5.31. Radiation damage test of the samples with different embedding. Each time increment is 20 ms, the insets show radiation damage tests for the pure epoxies without any fibers

To further evaluate the sample preparation approaches, the quality of the sample sectioning was evaluated by optical microscopy (Figure 5.32) and STXM measurements taken at the carbon post-edge (Figure 5.33). The thickness variation is important to evaluate since it is directly linked to the signal quality. If the sample is too thick the incident beam is mainly absorbed by the sample which results in poor data quality. If the sample is too thin the spectrum can appear noisy due to weak signal-to-noise ratio, making it difficult to extract meaningful chemical information[98].

The epoxy-based sample protocols (Spurr and cycloamine based epoxy) performed best from a sectioning perspective, providing the easiest sectioning process and resulting in large, uniform sections with well-dispersed fibers (Fig. 5.32a). Furthermore, the post edge STXM images showed that epoxy-based methods gave the most homogeneous sample thicknesses (Figure 5.33). This is emphasized when plotted with the same scalebar as the other embeddings (Fig. 5.33c and 5.33d).

The sample preparation approaches that involved immersion of the fibers in a liquid, like water or sucrose, and sectioning at cryogenic conditions caused issues with fiber clustering (Fig. 5.32c-d). This made it difficult to characterize individual fibers. The sucrose embedding protocol allowed for easy sectioning, whereas the water-embedded samples were more challenging due to the sample being brittle under cryogenic conditions. The post edge STXM images showed large thickness variations across the samples (Figure 5.33e-f), where the largest variations were found for the sucrose embedded sample.

The Sulphur embedding protocol posed the greatest challenges during the embedding phase, as the success of embedding was highly sensitive to temperature and timing of each embedding step. Once the embedding was successful, the sectioning was straightforward, creating sectioning ribbons of intermediate sizes (Fig. 5.32e). The Sulphur embedded sample also showed large variations in thickness when probed with STXM at the post edge (5.33g).

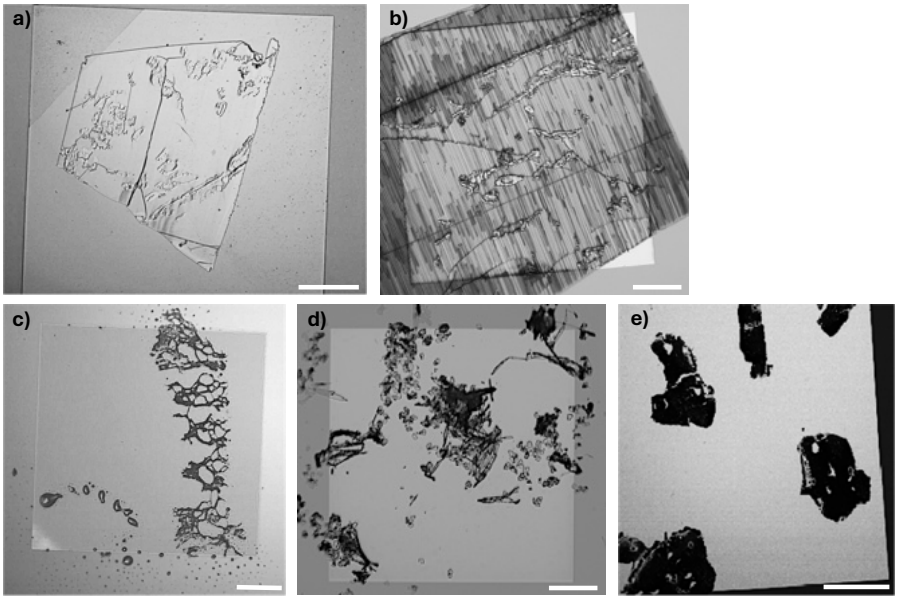

Figure 5.32. Microscopy images of sectioned samples. a) Spurr epoxy embedding b) Cycloamine based epoxy embedding c) Cryo-embedding with sucrose, d) Cryo-embedding with water d) Sulphur embedding. The scale bar corresponds to 0.2 mm.

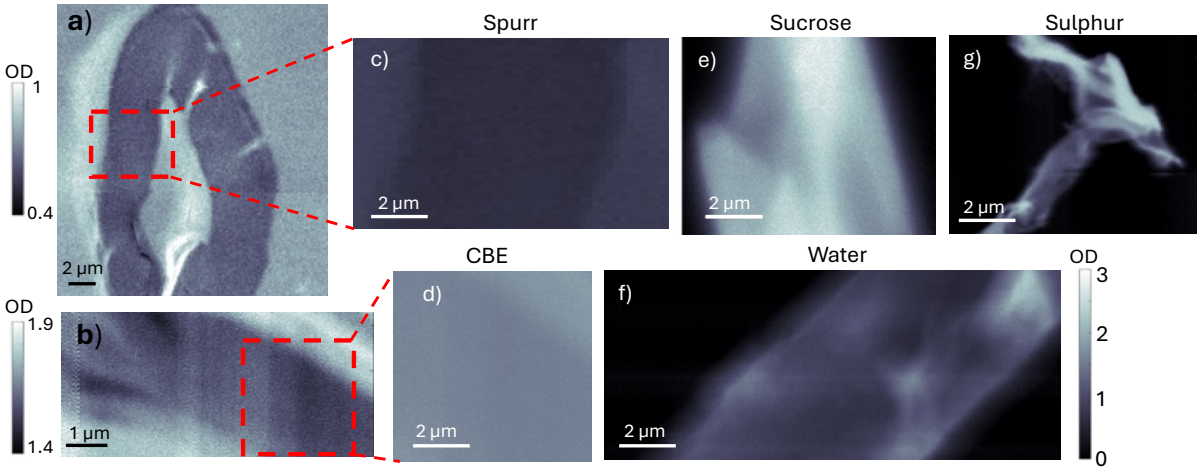

Figure 5.33. Images taken at the carbon post edge of fibers using Spurr epoxy (a, c), Cycloamine based epoxy (b, d), Sucrose (e), Water (f), and Sulphur (g) sample preparation protocols. The figure shows larger areas of epoxy embedded samples (Fig. 5.33 a-b) and plotted with a different scale bar of the optical density (OD) compared to Fig. 5.33 c-d.

In conclusion, the results from Paper VI show that each sample preparation approach investigated have different advantages and disadvantages when performing STXM measurements. The choice of sample preparation strategy for a certain experiment therefore needs to be determined based on the nature of the sample and the goal of the measurement.

Chapter 6 – Conclusions and Outlook

Understanding the complex structures of synthetic and cellulose-based packaging materials, and connecting structural changes with varied material-, processing- and environmental parameters, requires characterization techniques that offer structural and chemical insights with high spatial resolution. In this thesis, synchrotron based small- and wide-angle X-ray scattering (SAXS/WAXS) and scanning transmission X-ray microscopy (STXM) are used as primary techniques to image both synthetic and cellulose-derived polymer materials. The overall contributions from this thesis can be summarized into the following points:

- **New material insights:** Structural information from SAXS and WAXS has been used to explore the hierarchical structures of both synthetic and cellulose-derived packaging material. This has provided new insights into how structural morphology is linked to material, processing and environmental influences.
- **New applications of advanced characterization methods:** Synchrotron-based techniques have been used in new contexts and for new types of materials. For example, various analysis approaches of scanning SAXS/WAXS data have been explored and adapted to address different material systems and research questions. In addition, sample preparation protocols and measurement strategies have been developed and refined for STXM experiments.
- **Integration of complementary methods:** By combining structural characterization with complementary techniques such as mechanical testing, dynamic vapor sorption (DVS), and computational simulations, the thesis demonstrates varied approaches for material analysis.
- **Towards sustainable materials:** Cellulose-based materials require modifications to achieve thermoplastic behavior. This thesis contributes to understanding how such chemical modifications affect the resulting material structure, providing insight critical for the design of renewable, functional packaging materials.

The thesis consists of 6 research papers. Paper I and II focus on a synthetic polyethylene, Paper III and IV focus on dialcohol cellulose, Paper V focus on a commercial paper material used in drinking straw applications, and Paper VI focus on sample preparation strategies for STXM.

In Paper I, the relationship between processing conditions, hierarchical morphology, and mechanical performance in injection-molded low-density polyethylene (LDPE) with different molecular weights were investigated. Scanning SAXS was used to reveal distinct microstructural features across different layers. The results were combined with computational simulations to evaluate the shear- and temperature profiles in the through-thickness direction, and tensile testing to link the structures to the mechanical properties. The results showed that oriented shish-kebab and elongated spherulite microstructures contribute to high tensile strength when deformed in the direction of the flow. Moreover, it was shown that the molecular weight of the polymer and the position on the injection

molded plate highly influenced the hierarchical structure formed, where higher degree of orientation was found in higher molecular weight samples close to the injection mold gate. The deformation mechanisms were further studied by measuring scanning SAXS on deformed samples post mortem. It could be concluded that when samples are deformed perpendicularly to the flow, the orientation of the highly oriented shish-kebab structures close to the mold wall stays intact upon deformation whereas layers consisting of elongated spherulites and randomly oriented spherulites change their orientation in the direction of the applied stress.

In Paper II, a combination of scanning SAXS, WAXS, birefringence and light optical microscopy was used to get a more in-depth understanding of the layered morphology of high-density polyethylene (HDPE). Compared to LDPE, a more complex structure with more distinct layers were identified. HDPE samples produced with different process settings were characterized to further evaluate how process conditions influence the hierarchical structures, and it was found that the pressure during the holding phase of injection molding had a higher influence on the molecular structures than the injection speed. Furthermore, the crystallization process was evaluated from an energy perspective, where the specific work of flow was identified as the main parameter to capture the changes in morphology induced by varying process settings.

In Paper III, scanning WAXS was used to visualize the distribution and orientation of dialcohol cellulose within an EAA polymer matrix. Since there was little overlap between the cellulose (110)- peak and the EAA (020)- peak in WAXS, these peaks were used to separately evaluate orientation effects of the polymer and the cellulose. A homogeneous distribution of cellulose was found within all samples measured, indicating a good mixing between the cellulose and EAA. Furthermore, a loss in degree of orientation was found for cellulose with higher degree of modification whereas the degree of orientation of the EAA was unaffected by the degree of orientation of the cellulose.

In Paper IV, scanning SAXS and scanning WAXS were combined to study dialcohol cellulose, focusing on how addition of water during processing influences the structural morphology. Our findings show that processing without careful control can lead to irreversible structural degradation, including a decrease in crystallinity, disruption of fibers and alteration of fibril orientations, which is closely linked to the mechanical performance of the material.

In Paper V, a commercial paper-based material was probed with SAXS and WAXS to investigate how the material responds to changes in humidity. The study shows that a decrease in relative humidity causes both the fibril diameter and the center-to-center distance between fibrils to shrink significantly. We further investigate how the material responds when being soaked in a liquid, and we show that the liquid type significantly influences the swelling behavior.

In Paper VI, we explore different sample preparation strategies for STXM with NEXFS contrast, to achieve spatially resolved images with chemical contrast of cellulose fibers. We find that epoxy-based embeddings are beneficial for homogeneous sectioning, providing advantages during imaging, while embedding strategies without carbon species, such as elemental Sulphur or cryo-embedding with water, are more beneficial when evaluating the chemical content of the fiber. Furthermore, we show that one can spatially resolve different lignin compositions over a single thermomechanical pulp fiber.

The combined findings of this thesis show that synchrotron-based scanning SAXS/WAXS are powerful techniques with high potential to understand the complex morphology of both synthetic and cellulose-based packaging materials. As more materials are being developed to aid the transformation from fossil-based to bio-based packaging materials, the demand for detailed structural characterization will grow. Therefore, future effort must be put to continuously develop and adapt the advanced characterization techniques to fit new challenges. For instance, to gain more insights on the structural morphology of the materials studied, SAXS and WAXS measurements can be extended to in-situ studies, including mechanical deformation, rheology, or water-assisted processing. Such experiments would allow real-time observation of structural evolution that is critical for the material performance.

One of the main materials investigated in this thesis was partly modified dialcohol cellulose. Despite recent progress, some research questions remain that could be further addressed using advanced synchrotron techniques. For instance, there is still much to explore when it comes to processing, for example how the morphological changes observed vary with pH, shear rate and temperature. Such data could further be used as input to computational simulations, increasing the understanding of how modification and processing influence the material properties. Additionally, it is currently not known if the suggested core-shell structure in Figure 2.4 is correct. By implementing more advanced SAXS models, it may be possible to resolve the structural features of modified cellulose with greater precision.

Furthermore, the thesis has shown that STXM with NEXAFS contrast has high potential for chemical imaging of cellulose-based materials, providing both high energy and high spatial resolution. With the proper sample preparation approach, this can be used in future work to determine the localization of chemical modifications. This is a key consideration when modifying fiber-based materials. It is in particular important to understand if the modifications are mainly situated on the fiber surfaces or distributed within the fiber walls, since this insight may help to define the minimal degree of modification required to achieve thermoplasticity. Minimizing the degree of modification helps preserve the native fiber structures which supports biodegradability, as well as providing a more sustainable production by reducing the amounts of chemicals needed.

Acknowledgements

First and foremost, I would like to thank my supervisor, Marianne Liebi. I am deeply grateful for everything you have taught me, both in research and in life. Thank you for trusting me to explore my own ideas, for always being enthusiastic and present, and for lifting me up when thing have been tough. Thank you, Aleksandar, for being a great manager and examiner. You have always made sure I felt included in the division, especially after my research group relocated to Switzerland.

A huge thank you everyone in FibRe. Through the center, I got to meet and collaborate with a lot of fantastic people. Thank you, Anette, for always having time for me, and thank you, Giada, Katarina, and Enrica, for your collaboration during the beamtime experiments. I would also like to thank Åke, Adrian and Åsa for working with me on fun side projects.

To the team at Tetra Pak - Elin, Renan, Eskil, Fredrik L and Fredrik O. Thank you for the countless hours of scientific discussions during "Snillen spekulerar" and for bringing so much joy to my PhD journey. Elin, you are a true role model, thank you for all your support both in and outside our scientific discussions.

The biggest thank go to my current and former colleagues at the MF division. Thank you for making every day work so enjoyable. A special thanks to Filippa for being my first work bestie and now close friend, to Adrian for making our office the best office, to Mirna for always having my back and to Martina for being my number one choice for a beamtime partner. I would also like to thank the Swiss Liebi group, even if we are physically in different locations, you make it feel like we are close by. Thank you for making my trips to Switzerland so fun. A special thanks to Linnea Rensmo for trusting me to be your supervisor during you master's thesis project.

Thank you to the people working at the synchrotron beamlines where I conducted my experiments. Manuel, Ben and Viviane, Christian and Kim, thank you for sharing your expertise and making the experiments possible. I would also like to thank everyone who joined one of my beamtimes and helped keep spirits high during long night shifts.

To my friends and family, thank you for all the love and support. John, I would never have managed this without you, thank you for always being my rock. Vidar, thank you for coming into my life, you mean the world to me.

Finally, I gratefully acknowledge the Swedish Innovation Agency VINNOVA and the competence center FibRe for providing funding for this work

Bibliography

(1) Escursell, S.; Llorach-Massana, P.; Roncero, M. B. Sustainability in e-commerce packaging: A review. *J Clean Prod* 2021, *280*, 124314. DOI: 10.1016/j.jclepro.2020.124314 From NLM.

(2) Parameswaranpillai, J.; Gopi, J. A.; Radoor, S.; C. D., M. D.; Krishnasamy, S.; Deshmukh, K.; Hameed, N.; Salim, N. V.; Sienkiewicz, N. Turning waste plant fibers into advanced plant fiber reinforced polymer composites: A comprehensive review. *Composites Part C: Open Access* 2023, *10*, 100333. DOI: https://doi.org/10.1016/j.jcomc.2022.100333.

(3) Vasile, C.; Sivertsvik, M. *Food Packaging: Materials and Technologies*; MDPI - Multidisciplinary Digital Publishing Institute, 2019.

(4) Geyer, R.; Jambeck, J.; Law, K. Production, use, and fate of all plastics ever made. *Science Advances* 2017, *3*, e1700782. DOI: 10.1126/sciadv.1700782.

(5) PlasticsEurope. *Plastics-the Facts* 2021. https://plasticseurope.org/wp-content/uploads/2021/12/Plastics-the-Facts-2021-web-final.pdf.

(6) Demirors, M. The History of Polyethylene. In *100+ Years of Plastics*, ACS Symposium Series, Vol. 1080; American Chemical Society, 2011; pp 115-145.

(7) Ganie, S. A.; Ali, A.; Mir, T. A.; Li, Q. 5 - Fabrication and characterization of cellulose-based green materials. In *Advanced Green Materials*, Ahmed, S. Ed.; Woodhead Publishing, 2021; pp 61-73.

(8) Fox, S. C.; Li, B.; Xu, D.; Edgar, K. J. Regioselective Esterification and Etherification of Cellulose: A Review. *Biomacromolecules* 2011, *12* (6), 1956-1972. DOI: 10.1021/bm200260d.

(9) Sescousse, R.; Gavillon, R.; Budtova, T. Aerocellulose from cellulose–ionic liquid solutions: Preparation, properties and comparison with cellulose–NaOH and cellulose–NMMO routes. *Carbohydrate polymers* 2011, *83* (4), 1766-1774. DOI: 10.1016/j.carbpol.2010.10.043.

(10) Jedvert, K.; Heinze, T. Cellulose modification and shaping – a review. 2017, *37*(9), 845-860. DOI: doi:10.1515/polyeng-2016-0272 (accessed 2024-04-15).

(11) Shrivastava, A. 1 - Introduction to Plastics Engineering. In *Introduction to Plastics Engineering*, Shrivastava, A. Ed.; William Andrew Publishing, 2018; pp 1-16.

(12) Schultz, S. S. K. a. J. M. The Microstructure of Injection-Molded Semicrystalline Polymers: A Review. *POLYMER ENGINEERING AND SCIENCE* 1982.

(13) Young, R. A.; Rowell, R. M. *Cellulose: Structure, Modification, and Hydrolysis*; Wiley, 1986.

(14) Heinze, T. Cellulose: Structure and Properties. *Advances in Polymer Science* 2015, *271*, 1-52. DOI: 10.1007/12_2015_319.

(15) Tajeddin, B.; Arabkhedri, M. Chapter 16 - Polymers and food packaging. In *Polymer Science and Innovative Applications*, AlMaadeed, M. A. A., Ponnamma, D., Carignano, M. A. Eds.; Elsevier, 2020; pp 525-543.

(16) Keller, A.; Mackley, M. Chain orientation and crystallization. *Pure and Applied Chemistry - PURE APPL CHEM* 1974, *39*, 195-224. DOI: 10.1351/pac197439010195.

(17) Verho, T.; Paajanen, A.; Vaari, J.; Laukkanen, A. Crystal Growth in Polyethylene by Molecular Dynamics: The Crystal Edge and Lamellar Thickness. *Macromolecules* 2018, *51* (13), 4865-4873. DOI: 10.1021/acs.macromol.8b00857.

(18) Albrecht, T.; Strobl, G. Temperature-Dependent Crystalline-Amorphous Structures in Linear Polyethylene: Surface Melting and the Thickness of the Amorphous Layers. *Macromolecules* 1995, *28* (17), 5827-5833. DOI: 10.1021/ma00121a020.

(19) Jones, R. A. L. *Soft Condensed Matter*; Oxford University Press, 2002.

(20) Zhang, M. C.; Guo, B.-H.; Xu, J. A Review on Polymer Crystallization Theories. *Crystals* 2017, *7* (1), 4.

(21) Pantani, R.; Sorrentino, A.; Speranza, V.; Titomanlio, G. Molecular orientation in injection molding: Experiments and analysis. *Rheologica Acta* 2004, *43*, 109-118. DOI: 10.1007/s00397-003-0325-8.

(22) Leary, M. Design for Additive Manufacturing
A volume in Additive Manufacturing Materials and Technologies In *Design for Additive Manufacturing*, Leary, M. Ed.; Elsevier, 2020; pp 223-268.

(23) Tiago, G. A. O.; Mariquito, A.; Martins-Dias, S.; Marques, A. C. The problem of polyethylene waste – recent attempts for its mitigation. *Science of The Total Environment* 2023, *892*, 164629. DOI: https://doi.org/10.1016/j.scitotenv.2023.164629.

(24) Schwab, S. T.; Baur, M.; Nelson, T. F.; Mecking, S. Synthesis and Deconstruction of Polyethylene-type Materials. *Chemical Reviews* 2024, *124* (5), 2327-2351. DOI: 10.1021/acs.chemrev.3c00587.

(25) SWAN, P. R. Polyethylene -Unit Cell Variations with Temperature. *JOURNAL OF POLYMER SCIENCE* 1962, *56*, 403-407.

(26) Miao, M.; Zhang, M. L.; Doren, V.; Van Alsenoy, C.; Martins, J. Density functional calculations on the structure of crystalline polyethylene under high pressures. *The Journal of Chemical Physics* 2001, *115*. DOI: 10.1063/1.1420404.

(27) Padden, F. J.; Keith, H. D. Spherulitic Crystallization in Polypropylene. *Journal of Applied Physics* 1959, *30* (10), 1479-1484. DOI: 10.1063/1.1734985 (accessed 2022/05/10).

(28) Butler, M. F.; Donald, A. M. A Real-Time Simultaneous Small- and Wide-Angle X-ray Scattering Study of in Situ Polyethylene Deformation at Elevated Temperatures. *Macromolecules* 1998, *31* (18), 6234-6249. DOI: 10.1021/ma970681r.

(29) Hobbs, J. K.; Miles, M. J. Direct Observation of Polyethylene Shish-Kebab Crystallization Using in-Situ Atomic Force Microscopy. *Macromolecules* 2001, *34* (3), 353-355. DOI: 10.1021/ma001697b.

(30) Keller, A.; Machin, M. J. Oriented crystallization in polymers. *Journal of Macromolecular Science, Part B* 1967, *1* (1), 41-91. DOI: 10.1080/00222346708212739.

(31) Regrain, C.; Laiarinandrasana, L.; Toillon, S.; Saï, K. Multi-mechanism models for semi-crystalline polymer: Constitutive relations and finite element implementation. *International Journal of Plasticity* 2009, *25* (7), 1253-1279. DOI: https://doi.org/10.1016/j.ijplas.2008.09.010.

(32) Liu, Z.; Liu, X.; Li, L.; Zheng, G.; Liu, C.; Qin, Q.; Mi, L. Crystalline structure and remarkably enhanced tensile property of β-isotactic polypropylene via overflow microinjection molding. *Polymer Testing* 2019, *76*. DOI: 10.1016/j.polymertesting.2019.04.002.

(33) Dashan Mi, M. Z., Jie Zhang. Quantification of shish–kebab and b-crystal on the mechanicalproperties of polypropylene. 2017.

(34) Schrauwen, B. A. G.; Breemen, L. C. A. v.; Spoelstra, A. B.; Govaert, L. E.; Peters, G. W. M.; Meijer, H. E. H. Structure, Deformation, and Failure of Flow-Oriented Semicrystalline Polymers. *Macromolecules* 2004, *37* (23), 8618-8633. DOI: 10.1021/ma048884k.

(35) Schrauwen, B. A. G.; Janssen, R. P. M.; Govaert, L. E.; Meijer, H. E. H. Intrinsic Deformation Behavior of Semicrystalline Polymers. *Macromolecules* 2004, *37* (16), 6069-6078. DOI: 10.1021/ma035279t.

(36) Somani, R. H.; Yang, L.; Zhu, L.; Hsiao, B. S. Flow-induced shish-kebab precursor structures in entangled polymer melts. *Polymer* 2005, *46* (20), 8587-8623. DOI: https://doi.org/10.1016/j.polymer.2005.06.034.

(37) Tong, Y.; Lin, Y.; Wang, S.; Song, M. A study of crystallisation of poly (ethylene oxide) and polypropylene on graphene surface. *Polymer* 2015, *73*, 52-61. DOI: https://doi.org/10.1016/j.polymer.2015.07.025.

(38) Ejikeme, P. Investigation of The Physicochemical Properties of Microcrystalline Cellulose From Agricultural Wastes I: Orange Mesocarp. *Cellulose* 2008, *15*, 141-147. DOI: 10.1007/s10570-007-9147-7.

(39) Mohamad Haafiz, M. K.; Eichhorn, S. J.; Hassan, A.; Jawaid, M. Isolation and characterization of microcrystalline cellulose from oil palm biomass residue. *Carbohydrate Polymers* 2013, *93* (2), 628-634. DOI: https://doi.org/10.1016/j.carbpol.2013.01.035.

(40) De Assis, T.; Pawlak, J.; Pal, L.; Venditti, R.; Reisinger, L.; Kavalew, D.; Gonzalez, R. Comparison of Wood and Non-Wood Market Pulps for Tissue Paper Application. *Bioresources* 2019, *14*, 6781-6810. DOI: 10.15376/biores.14.3.6781-6810.

(41) Elfaleh, I.; Abbassi, F.; Habibi, M.; Ahmad, F.; Guedri, M.; Nasri, M.; Garnier, C. A comprehensive review of natural fibers and their composites: An eco-friendly alternative to conventional materials. *Results in Engineering* 2023, *19*, 101271. DOI: https://doi.org/10.1016/j.rineng.2023.101271.

(42) Sjostrom, E. Chapter 1 - THE STRUCTURE OF WOOD. In *Wood Chemistry (Second Edition)*, SjÖStrÖM, E. Ed.; Academic Press, 1993; pp 1-20.

(43) Sjostrom, E. *Wood chemistry: fundamentals and applications*; Gulf professional publishing, 1993.

(44) Fengel, D.; Wegener, G. *Wood*; De Gruyter, 1983. DOI: 10.1515/9783110839654.

(45) Penttilä, P. Structural characterization of cellulosic materials using x-ray and neutron scattering. 2013.

(46) Huber, T.; Müssig, J.; Curnow, O.; Pang, S.; Bickerton, S.; Staiger, M. P. A critical review of all-cellulose composites. *Journal of Materials Science* 2012, *47* (3), 1171-1186. DOI: 10.1007/s10853-011-5774-3.

(47) Müssig, J. Industrial Applications of Natural Fibres: Structure, Properties and Technical Applications. 2010, 14-20. DOI: 10.1002/9780470660324.

(48) Saito, T.; Kuramae, R.; Wohlert, J.; Berglund, L. A.; Isogai, A. An Ultrastrong Nanofibrillar Biomaterial: The Strength of Single Cellulose Nanofibrils Revealed via Sonication-Induced Fragmentation. *Biomacromolecules* 2013, *14* (1), 248-253. DOI: 10.1021/bm301674e.

(49) Rullifank, K.; Roefinal, M.; Kostanti, M.; Sartika, L.; Evelyn, E. Pulp and paper industry: An overview on pulping technologies, factors, and challenges. *IOP Conference Series: Materials Science and Engineering* 2020, *845*, 012005. DOI: 10.1088/1757-899X/845/1/012005.

(50) Casey, J. P. *Pulp and Paper: Chemistry and Chemical Technology*; Wiley, 1980.

(51) Mleziva, M. M.; Wang, J. H. 10.23 - Paper. In *Polymer Science: A Comprehensive Reference*, Matyjaszewski, K., Möller, M. Eds.; Elsevier, 2012; pp 397-410.

(52) Larsson, P.; Berglund, L.; Wågberg, L. Highly ductile fibres and sheets by core-shell structuring of the cellulose nanofibrils. *Cellulose* 2014, *21*, 323-333. DOI: 10.1007/s10570-013-0099-9.

(53) Gaspar-Cunha, A.; Covas, J. A.; Sikora, J. Optimization of Polymer Processing: A Review (Part I—Extrusion). *Materials* 2022, *15* (1), 384.

(54) Yazıcı, N.; Kodal, M.; Ozkoc, G. Lab-Scale Twin-Screw Micro-Compounders as a New Rubber-Mixing Tool: 'A Comparison on EPDM/Carbon Black and EPDM/Silica Composites'. *Polymers* 2021, *13*, 4391. DOI: 10.3390/polym13244391.

(55) Orelma, H.; Tanaka, A.; Vuoriluoto, M.; Khakalo, A.; Korpela, A. Manufacture of all-wood sawdust-based particle board using ionic liquid-facilitated fusion process. *Wood Science and Technology* 2021, *55*, 1-19. DOI: 10.1007/s00226-021-01265-x.

(56) Fu, H.; Xu, H.; Liu, Y.; Yang, Z.; Kormakov, S.; Wu, D.; Sun, J. Overview of Injection Molding Technology for Processing Polymers and Their Composites. *ES Materials & Manufacturing* 2020. DOI: 10.30919/esmm5f713.

(57) Dakshinamoorthi, M.; Ghazaly, N.; R, V. Minimization of sink mark defects in injection molding process – Taguchi approach. *International Journal of Engineering, Science and Technology* 2010, *2*. DOI: 10.4314/ijest.v2i2.59133.

(58) Angelloz, C.; Fulchiron, R.; Douillard, A.; Chabert, B.; Fillit, R.; Vautrin, A.; David, L. Crystallization of Isotactic Polypropylene under High Pressure (γ Phase). *Macromolecules* 2000, *33* (11), 4138-4145. DOI: 10.1021/ma991813e.

(59) Pantani, R.; Coccorullo, I.; Speranza, V.; Titomanlio, G. Morphology evolution during injection molding: Effect of packing pressure. *Polymer* 2007, *48* (9), 2778-2790. DOI: https://doi.org/10.1016/j.polymer.2007.03.007.

(60) Wang, J.; Wang, L.; Bian, N.; Wang, D.; Wang, Y.; Zhang, Y.; Li, Q.; Shen, C. Influence of shear history on morphology, microstructure and mechanical properties of micro injection molded parts. *Huagong Xuebao/CIESC Journal* 2015, *66*, 1931-1938. DOI: 10.11949/j.issn.0438-1157.20141661.

(61) Boyer, S. A. E.; Haudin, J.-M. Crystallization of polymers at constant and high cooling rates: A new hot-stage microscopy set-up. *Polymer Testing* 2010, *29* (4), Pages 445-452. DOI: 10.1016/j.polymertesting.2010.02.003

(62) Wingstrand, S. L.; van Drongelen, M.; Mortensen, K.; Graham, R. S.; Huang, Q.; Hassager, O. Influence of Extensional Stress Overshoot on Crystallization of LDPE. *Macromolecules* 2017, *50* (3), 1134-1140. DOI: 10.1021/acs.macromol.6b02543.

(63) Zhou, H. *Computer modeling for injection molding : simulation, optimization, and control*; Wiley, 2013.

(64) Fernandes, C.; Pontes, A.; Viana, J.; Gaspar-Cunha, A. Modeling and Optimization of the Injection-Molding Process: A Review. *Advances in Polymer Technology* 2016, *37*. DOI: 10.1002/adv.21683.

(65) Agarwal, A.; Shaida, B.; Rastogi, M.; Singh, N. B. Food Packaging Materials with Special Reference to Biopolymers-Properties and Applications. *Chemistry Africa* 2023, *6* (1), 117-144. DOI: 10.1007/s42250-022-00446-w.

(66) Commission, E.; Environment, D.-G. f. *Turning the tide on single-use plastics*; Publications Office of the European Union, 2021. DOI: doi/10.2779/800074.

(67) Goring, D. Thermal softening, adhesive properties and glass transitions in lignin, hemicellulose and cellulose. In *Trans. of the IIIrd Fund. Res. Symp. Cambridge, 1965*, 1965; Fundamental Research Committee (FRC), Manchester: pp 555-568.

(68) Salmén, N. L.; Back, E. L. Effect of temperature on stress-strain properties of dry papers. *Svensk papperstidning* 1978, *81*.

(69) Shafizadeh, F.; Bradbury, A. Thermal degradation of cellulose in air and nitrogen at low temperatures. *Journal of applied polymer science* 1979, *23* (5), 1431-1442.

(70) Liu, Y.; Ahmed, S.; Sameen, D. E.; Wang, Y.; Lu, R.; Dai, J.; Li, S.; Qin, W. A review of cellulose and its derivatives in biopolymer-based for food packaging application. *Trends in Food Science & Technology* 2021, *112*, 532-546. DOI: https://doi.org/10.1016/j.tifs.2021.04.016.

(71) Seddiqi, H.; Oliaei, E.; Honarkar, H.; Jin, J.; Geonzon, L. C.; Bacabac, R. G.; Klein-Nulend, J. Cellulose and its derivatives: towards biomedical applications. *Cellulose* 2021, *28* (4), 1893-1931. DOI: 10.1007/s10570-020-03674-w.

(72) Quintana, R.; Persenaire, O.; Bonnaud, L.; Dubois, P. Recent advances in (reactive) melt processing of cellulose acetate and related biodegradable bio-compositions. *Polymer Chemistry* 2012, *3* (3), 591-595, Review. DOI: 10.1039/c1py00421b Scopus.

(73) Olsson, M.; Govender, R.; Diaz, A.; Holler, M.; Menzel, A.; Abrahmsén-Alami, S.; Sadd, M.; Larsson, A.; Matic, A.; Liebi, M. Multiscale X-ray imaging and characterisation of pharmaceutical dosage forms. *International Journal of Pharmaceutics* 2023, *642*, 123200. DOI: https://doi.org/10.1016/j.ijpharm.2023.123200.

(74) M. R. Kantz, H. D. N. J., F. H. Stigale. The skin-core morphology and structure–property relationships in injection-molded polypropylene. *Journal of Applied Polymer Science* 1972, *16*, 1249-1260.

(75) Bernard A.G. Schrauwen, L. E. G., Gerrit W.M. Peters, Han E.H. Meijer. The influence of flow-induced crystallization on the impact toughness of high-density polyethylenev. *Macromolecular Symposia* 2002, *2002*.

(76) Liu, X. H.; Zheng, G. Q.; Jia, Z. H.; Li, S. W.; Liu, C. G.; Zhang, Y.; Shao, C. G.; Dai, K.; Liu, B. C.; Zhang, Q. X.; et al. The hierarchical structure of water-assisted injection molded high density polyethylene: Small angle X-ray scattering study. *Journal of Applied Polymer Science* 2012, *125* (3), 2297-2303. DOI: 10.1002/app.36408.

(77) Wang, L.; Wang, J. H.; Yang, B.; Wang, Y.; Zhang, Q. P.; Yang, M. B.; Feng, J. M. A novel hierarchical crystalline structure of injection-molded bars of linear polymer: co-existence of bending and normal shish-kebab structure. *Colloid and Polymer Science* 2013, *291* (6), 1503-1511. DOI: 10.1007/s00396-012-2887-4.

(78) Bartczak, Z.; Vozniak, A. WAXS/SAXS study of plastic deformation instabilities and lamellae fragmentation in polyethylene. *Polymer* 2019, *177*, 160-177. DOI: https://doi.org/10.1016/j.polymer.2019.05.076.

(79) Deng, B.; Chen, L.; Li, X.; Wang, Z. Influence of Prereserved Shish Crystals on the Structural Evolution of Ultrahigh-Molecular Weight Polyethylene Films during the Hot Stretching Process. *Macromolecules* 2022, *55* (11), 4600-4613. DOI: 10.1021/acs.macromol.2c00343.

(80) Zhao, X.; Liao, T.; Yang, X.; Coates, P.; Whiteside, B.; Barker, D.; Thompson, G.; Jiang, Z.; Men, Y. Mold temperature- and molar mass-dependent structural formation in micro-injection molding of isotactic polypropylene. *Polymer* 2022, *248*, 124797. DOI: https://doi.org/10.1016/j.polymer.2022.124797.

(81) Fernandez, E.; Edeleva, M.; Fiorio, R.; Cardon, L.; D'hooge, D. R. Increasing the Sustainability of the Hybrid Mold Technique through Combined Insert Polymeric Material and Additive Manufacturing Method Design. *Sustainability* 2022, *14* (2), 877.

(82) Somani, R.; Yang, L.; Hsiao, B. Effects of high molecular weight species on shear-induced orientation and crystallization of isotactic polypropylene. *Polymer* 2006, *47*, 5657-5668. DOI: 10.1016/j.polymer.2004.12.066.

(83) Wang, Z.; Mao, Y.-M.; Li, X.-K.; Li, Y.-G.; Jarumaneeroj, C.; Thitisak, B.; Tiyapiboonchaiya, P.; Rungswang, W.; Hsiao, B. The Influence of Ethyl Branch on Formation of Shish-Kebab Crystals in Bimodal Polyethylene under Shear at Low Temperature. *Chinese Journal of Polymer Science* 2021, *39*. DOI: 10.1007/s10118-021-2568-1.

(84) Wang, Z.; Zhu, M.; Song, T.; Li, X.; Hsiao, B. S. Shear-induced crystallization of unimodal/bimodal polyethylene at high temperatures affected by C4 short-branching. *Polymer* 2021, *233*, 124203. DOI: https://doi.org/10.1016/j.polymer.2021.124203.

(85) Kamal, V. T. a. M. R. Morphological Zones and Orientation in Injection-Molded Polyethylene. *Journal of Applied Polymer Science* 1978, *22*, 2341-2355.

(86) Cuvelliez, V. L. a. C. The Effect of the Packing Parameters, Gate Geometry, and Mold Elasticity on the Final Dimensions of a Molded Part. *Polymer Engineering and Science* 1996, *36*, 1961-1971.

(87) Rong Zheng, R. I. T., D. Lee. Wo, Xi-jun Fan, C. Hadinata, F. S. Costa, P. K. Kennedy, P. Zhu, and G. Edward. Modeling of flow-induced crystallization of colored polypropylene in injection molding. *Korea-Australia Rheology Journal* 2010, *22 No 3*.

(88) Costa, G. T. a. F. S. High precision validation of micro injection molding process simulations. *Journal of Manufacturing Processes* 2019, *48*, 236-248.

(89) Elf, P.; Larsson, P. A.; Larsson, A.; Wågberg, L.; Hedenqvist, M. S.; Nilsson, F. Effects of Ring Opening and Chemical Modification on the Properties of Dry and Moist Cellulose—Predictions with Molecular Dynamics Simulations. *Biomacromolecules* 2024, *25* (12), 7581-7593. DOI: 10.1021/acs.biomac.4c00735.

(90) Elf, P.; Özeren, H. D.; Larsson, P. A.; Larsson, A.; Wågberg, L.; Nilsson, R.; Chaiyupatham, P. T.; Hedenqvist, M. S.; Nilsson, F. Molecular Dynamics Simulations of Cellulose and Dialcohol Cellulose under Dry and Moist Conditions. *Biomacromolecules* 2023, *24* (6), 2706-2720. DOI: 10.1021/acs.biomac.3c00156.

(91) Willmott, P. *An introduction to Synchrotron Radiation: Techniques and Applications*; John Wiley & Sons, 2011.

(92) Seibert, J. A.; Boone, J. M. X-Ray Imaging Physics for Nuclear Medicine Technologists. Part 2: X-Ray Interactions and Image Formation. *Journal of Nuclear Medicine Technology* 2005, *33* (1), 3-18.

(93) Hsieh, J. Computed tomography: principles, design, artifacts, and recent advances. 2003.

(94) Mobilio, S.; Boscherini, F.; Meneghini, C. *Synchrotron Radiation: Basics, Methods and Applications*; 2015. DOI: 10.1007/978-3-642-55315-8.

(95) Haehner, G. Near Edge X-Ray Absorption Fine Structure Spectroscopy as a Tool to Probe Electronic and Structural Properties of Thin Organic Films and Liquids. *ChemInform* 2007, *38* (14). DOI: https://doi.org/10.1002/chin.200714280.

(96) Stöhr, J. *NEXAFS spectroscopy*; Springer Science & Business Media, 2013.

(97) Raabe, J.; Tzvetkov, G.; Flechsig, U.; Böge, M.; Jaggi, A.; Sarafimov, B.; Vernooij, M. G. C.; Huthwelker, T.; Ade, H.; Kilcoyne, D.; et al. PolLux: A new facility for soft x-ray spectromicroscopy at the Swiss Light Source. *Review of Scientific Instruments* 2008, *79* (11). DOI: 10.1063/1.3021472 (accessed 2/17/2025).

(98) Watts, B.; Finizio, S.; Raabe, J. Quantifying signal quality in scanning transmission X-ray microscopy. *J Synchrotron Radiat* 2022, *29* (Pt 4), 1054-1064. DOI: 10.1107/s1600577522004210 From NLM.

(99) Karunakaran, C.; Christensen, C. R.; Gaillard, C.; Lahlali, R.; Blair, L. M.; Perumal, V.; Miller, S. S.; Hitchcock, A. P. Introduction of Soft X-Ray Spectromicroscopy as an Advanced Technique for Plant Biopolymers Research. *PLOS ONE* 2015, *10* (3), e0122959. DOI: 10.1371/journal.pone.0122959.

(100) Henke, B. L.; Gullikson, E. M.; Davis, J. C. X-Ray Interactions: Photoabsorption, Scattering, Transmission, and Reflection at E = 50-30,000 eV, Z = 1-92. *Atomic Data and Nuclear Data Tables* 1993, *54* (2), 181-342. DOI: https://doi.org/10.1006/adnd.1993.1013.

(101) Adler, E. Lignin chemistry—past, present and future. *Wood Science and Technology* 1977, *11* (3), 169-218. DOI: 10.1007/BF00365615.

(102) Behrens, S.; Kappler, A.; Obst, M. Linking environmental processes to the in situ functioning of microorganisms by high-resolution secondary ion mass spectrometry (NanoSIMS) and scanning transmission X-ray microscopy (STXM). *Environmental Microbiology* 2012, *14* (11), 2851-2869. DOI: https://doi.org/10.1111/j.1462-2920.2012.02724.x.

(103) J.M.G Cowie, V. A. *Polymer Chemistry and Physics of Modern Materials Third Edition*; CRC Press, 2014.

(104) Virtanen, T.; Penttilä, P. A.; Maloney, T. C.; Grönqvist, S.; Kamppuri, T.; Vehviläinen, M.; Serimaa, R.; Maunu, S. L. Impact of mechanical and enzymatic pretreatments on softwood pulp fiber wall structure studied with NMR spectroscopy and X-ray scattering. *Cellulose* 2015, *22* (3), 1565-1576. DOI: 10.1007/s10570-015-0619-x.

(105) Schmacke, S. Investigations of Polyethylene Materials by Means of X-ray Diffraction Artificial Ageing of Polyethylene Gas Pipes. der Technischen Universität Dortmund, 2010.

(106) Möller, K. M. a. M. *Polymer Science: A Comprehensive Reference*; 2012.

(107) O Bunk, M. B., T H Jensen, R Feidenhans'l, T Binderup, A Menzel and F Pfeiffer. Multimodal x-ray scatter imaging. *New Journal of Physics* 2009, *11*.

(108) Strobl, G. R.; Schneider, M. Direct evaluation of the electron density correlation function of partially crystalline polymers. *Journal of Polymer Science: Polymer Physics Edition* 1980, *18* (6), 1343-1359. DOI: https://doi.org/10.1002/pol.1980.180180614.

(109) Ruland, W. The evaluation of the small-angle scattering of lamellar two-phase systems by means of interface distribution functions. *Colloid and Polymer Science* 1977, *255* (5), 417-427. DOI: 10.1007/BF01536457.

(110) Goderis, B.; Reynaers, H.; Koch, M. H. J.; Mathot, V. B. F. Use of SAXS and linear correlation functions for the determination of the crystallinity and morphology of semi-crystalline polymers. Application to linear polyethylene. *Journal of Polymer Science Part B: Polymer Physics* 1999, *37* (14), 1715-1738. DOI: https://doi.org/10.1002/(SICI)1099-0488(19990715)37:14.

(111) Singh, H. S. a. Y. *The SAXS Guide*; Anton Paar GmbH, 2017.

(112) Hashimoto, T.; Kawamura, T.; Harada, M.; Tanaka, H. Small-Angle Scattering from Hexagonally Packed Cylindrical Particles with Paracrystalline Distortion. *Macromolecules* 1994, *27* (11), 3063-3072. DOI: 10.1021/ma00089a025.

(113) Penttilä, P.; Rautkari, L.; Österberg, M.; Schweins, R. Small-angle scattering model for efficient characterization of wood nanostructure and moisture behaviour. *Journal of Applied Crystallography* 2019, *52*. DOI: 10.1107/S1600576719002012.

(114) Segal, L.; Creely, J. J.; Martin, A. E.; Conrad, C. M. An Empirical Method for Estimating the Degree of Crystallinity of Native Cellulose Using the X-Ray Diffractometer. *Textile Research Journal* 1959, *29* (10), 786-794. DOI: 10.1177/004051755902901003.

(115) French, A. D. Increment in evolution of cellulose crystallinity analysis. *Cellulose* 2020, *27* (10), 5445-5448. DOI: 10.1007/s10570-020-03172-z.

(116) Agarwal, U. P.; Ralph, S. A.; Reiner, R. S.; Moore, R. K.; Baez, C. Impacts of fiber orientation and milling on observed crystallinity in jack pine. *Wood science and technology* 2014, *48* (6), 1213-1227.

(117) Park, S.; Baker, J. O.; Himmel, M. E.; Parilla, P. A.; Johnson, D. K. Cellulose crystallinity index: measurement techniques and their impact on interpreting cellulase performance. *Biotechnology for Biofuels* 2010, *3* (1). DOI: Artn 10 10.1186/1754-6834-3-10.

(118) Thygesen, A.; Oddershede, J.; Lilholt, H.; Thomsen, A. B.; Ståhl, K. On the determination of crystallinity and cellulose content in plant fibres. *Cellulose* 2005, *12* (6), 563.

(119) He, J.; Cui, S.; Wang, S. y. Preparation and crystalline analysis of high-grade bamboo dissolving pulp for cellulose acetate. *J. Appl. Polym. Sci.* 2008, *107* (2), 1029-1038.

(120) Hult, E.-L.; Iversen, T.; Sugiyama, J. Characterization of the supermolecular structure of cellulose in wood pulp fibres. *Cellulose* 2003, *10* (2), 103-110.

(121) Garvey, C. J.; Parker, I. H.; Simon, G. P. On the interpretation of X-ray diffraction powder patterns in terms of the nanostructure of cellulose I fibres. *Macromolecular Chemistry and Physics* 2005, *206* (15), 1568-1575.

(122) Teeäär, R.; Serimaa, R.; Paakkari, T. Crystallinity of cellulose, as determined by CP/MAS NMR and XRD methods. *Polymer Bulletin* 1987, *17* (3), 231-237.

(123) Rodrigues Filho, G.; de Assunçao, R. M.; Vieira, J. G.; Meireles, C. d. S.; Cerqueira, D. A.; da Silva Barud, H.; Ribeiro, S. J.; Messaddeq, Y. Characterization of methylcellulose produced from sugar cane bagasse cellulose: Crystallinity and thermal properties. *Polymer degradation and stability* 2007, *92* (2), 205-210.

(124) Holzwarth, U.; Gibson, N. The Scherrer equation versus the 'Debye-Scherrer equation'. *Nature Nanotechnology* 2011, *6* (9), 534-534. DOI: 10.1038/nnano.2011.145.

(125) Chatterjee, A. K. 8 - X-Ray Diffraction. In *Handbook of Analytical Techniques in Concrete Science and Technology*, Ramachandran, V. S., Beaudoin, J. J. Eds.; William Andrew Publishing, 2001; pp 275-332.

(126) O'Connor, D. G.; Findley, W. N. Influence of normal stress on creep in tension and compression of polyethylene and rigid polyvinyl chloride copolymer. *Polymer Engineering and Science* 1962, *2*, 273-284.

(127) Sauer, J. A.; Mears, D.; Pae, K. D. Effects of hydrostatic pressure on the mechanical behaviour of polytetrafluoroethylene and polycarbonate. *European Polymer Journal - EUR POLYM J* 1970, *6*, 1015-1032. DOI: 10.1016/0014-3057(70)90034-0.

(128) Colak, O.; Düşünceli, N. Modeling Viscoelastic and Viscoplastic Behavior of High Density Polyethylene (HDPE). *Journal of Engineering Materials and Technology-transactions of The Asme - J ENG MATER TECHNOL* 2006, *128*. DOI: 10.1115/1.2345449.

(129) Pawlak, A.; Galeski, A. Plastic Deformation of Crystalline Polymers: The Role of Cavitation and Crystal Plasticity. *Macromolecules* 2005, *38* (23), 9688-9697. DOI: 10.1021/ma050842o.

(130) Clausen, A. H.; Polanco-Loria, M. A.; Berstad, T.; Hopperstad, S. A CONSTITUTIVE MODEL FOR THERMOPLASTICS WITH SOME APPLICATIONS.

(131) Arieby, R.; Mrabet, K.; Terfas, O.; Laurent, C.; Rahouadj, R. Anisotropic mechanical behavior of semi-crystalline polymers: Characterization and modeling of non-monotonic loading including damage. *Journal of Applied Polymer Science* 2016, *134*. DOI: 10.1002/app.44468.

(132) Martin Kroon, E. A., Elin Persson Jutemar, ; Viktor Petersson, L. P., Michael Dorn, Par Olsson Anisotropic Elastic-Viscoplastic Properties at Finite Strains of Injection-Moulded Low- Density Polyethylene. *Experimental Mechanics* 2017.

(133) Takeshi Okano, A. K. Structural variation of native cellulose related to its source. *Biopolymers* 1986.

(134) Büyüksarı, Ü.; As, N.; Dündar, T. Mechanical Properties of Earlywood and Latewood Sections of Scots Pine Wood. *Bioresources* 2017, *12*, 4004-4012.

(135) Wang, D.; Fu, F.; Lin, L. Molecular-level characterization of changes in the mechanical properties of wood in response to thermal treatment. *Cellulose* 2022, *29* (6), 3131-3142. DOI: 10.1007/s10570-022-04471-3.

(136) Zhou, L.; Ke, K.; Yang, M.-B.; Yang, W. Recent progress on chemical modification of cellulose for high mechanical-performance Poly(lactic acid)/Cellulose composite: A review. *Composites Communications* 2021, *23*, 100548. DOI: https://doi.org/10.1016/j.coco.2020.100548.

(137) Haward, S. J.; Toda-Peters, K.; Shen, A. Q. Steady viscoelastic flow around high-aspect-ratio, low-blockage-ratio microfluidic cylinders. *Journal of Non-Newtonian Fluid Mechanics* 2018, *254*, 23-35. DOI: https://doi.org/10.1016/j.jnnfm.2018.02.009.

(138) Larsson, P.; Wågberg, L. Towards natural-fibre-based thermoplastic films produced by conventional papermaking. *Green Chemistry* 2016, *18*. DOI: 10.1039/C5GC03068D.

(139) Hosseini, S.; Venkatesh, A.; Boldizar, A.; Westman, G. Molybdenum disulphide—A traditional external lubricant that shows interesting interphase properties in pulp-based composites. *Polymer Composites* 2021, *42* (9), 4884-4896. DOI: https://doi.org/10.1002/pc.26197.

(140) Kangas, H.; Suurnäkki, A.; Kleen, M. Modification of the surface chemistry of TMP with enzymes. *Nordic Pulp and Paper Research Journal* 2007, *22*, 415-423. DOI: 10.3183/NPPRJ-2007-22-04-p415-423.

(141) Späth, A.; Meyer, M.; Semmler, S.; Fink, R. H. Microspectroscopic soft X-ray analysis of keratin based biofibers. *Micron* 2015, *70*, 34-40. DOI: 10.1016/j.micron.2014.12.003.

(142) Lehmann, J.; Liang, B.; Solomon, D.; Lerotic, M.; Luizão, F.; Kinyangi, J.; Schäfer, T.; Wirick, S.; Jacobsen, C. Near-edge X-ray absorption fine structure (NEXAFS) spectroscopy for mapping nano-scale distribution of organic carbon forms in soil: Application to black carbon particles. *Global Biogeochemical Cycles* 2005, *19* (1). DOI: https://doi.org/10.1029/2004GB002435.

(143) Noguchi, T.; Takase, M.; Matsumoto, R.; Kebukawa, Y.; Suga, H.; Kondo, M.; Takahashi, Y.; Takeichi, Y.; Yabuta, H. An Another Protocol to Make Sulfur Embedded Ultrathin Sections of Extraterrestrial Small Samples. *Life* 2020, *10* (8), 135.

(144) Steudel, R.; Eckert, B.; Steudel, Y.; Wong, M.; Krossing, I.; Kleinjan, W.; Keizer, A.; Janssen, A. *Elemental Sulfur and Sulfur-Rich Compounds, Part 1*; 2003. DOI: 10.1007/b12115.

(145) Frommherz, U.; Raabe, J.; Watts, B.; Stefani, R.; Ellenberger, U. Higher Order Suppressor (HOS) for the PolLux Microspectroscope Beamline at the Swiss Light Source SLS. *AIP Conference Proceedings* 2010, *1234* (1), 429-432. DOI: 10.1063/1.3463232 (accessed 5/9/2025).

(146) Lerotic, M.; Mak, R.; Wirick, S.; Meirer, F.; Jacobsen, C. MANTiS: a program for the analysis of X-ray spectromicroscopy data. *J Synchrotron Radiat* 2014, *21* (Pt 5), 1206-1212. DOI: 10.1107/s1600577514013964 From NLM.

(147) Penttilä, P. A.; Altgen, M.; Awais, M.; Österberg, M.; Rautkari, L.; Schweins, R. Bundling of cellulose microfibrils in native and polyethylene glycol-containing wood cell walls revealed by small-angle neutron scattering. *Scientific Reports* 2020, *10* (1), 20844. DOI: 10.1038/s41598-020-77755-y.

(148) Larsson, P. T.; Stevanic-Srndovic, J.; Roth, S. V.; Söderberg, D. Interpreting SAXS data recorded on cellulose rich pulps. *Cellulose* 2022, *29* (1), 117-131. DOI: 10.1007/s10570-021-04291-x.

(149) Wang, Y.; Shi, Y.; Shao, W.; Ren, Y.; Dong, W.; Zhang, F.; Liu, L. Z. Crystallization, Structures, and Properties of Different Polyolefins with Similar Grafting Degree of Maleic Anhydride. *Polymers (Basel)* 2020, *12* (3). DOI: 10.3390/polym12030675 From NLM.

(150) Li, D.; Zhou, L.; Wang, X.; He, L.; Yang, X. Effect of Crystallinity of Polyethylene with Different Densities on Breakdown Strength and Conductance Property. *Materials (Basel)* 2019, *12* (11), 1746. DOI: 10.3390/ma12111746 PubMed.

(151) Fernandes, A. N.; Thomas, L. H.; Altaner, C. M.; Callow, P.; Forsyth, V. T.; Apperley, D. C.; Kennedy, C. J.; Jarvis, M. C. Nanostructure of cellulose microfibrils in spruce wood. *Proceedings of the National Academy of Sciences* 2011, *108* (47), E1195-E1203. DOI: doi:10.1073/pnas.1108942108.

(152) Jakob, H. F.; Fengel, D.; Tschegg, S. E.; Fratzl, P. The Elementary Cellulose Fibril in Picea abies: Comparison of Transmission Electron Microscopy, Small-Angle X-ray Scattering, and Wide-Angle X-ray Scattering Results. *Macromolecules* 1995, *28* (26), 8782-8787. DOI: 10.1021/ma00130a010.

(153) O'Sullivan, A. C. Cellulose: the structure slowly unravels. *Cellulose* 1997, *4* (3), 173-207. DOI: 10.1023/A:1018431705579.

(154) Keller, A.; O'Connor, A. Large Periods in Polyethylene: the Origin of Low-Angle X-ray Scattering. *Nature* 1957, *180* (4597), 1289-1290. DOI: 10.1038/1801289a0.
(155) Leung, W. M. Studies of low molecular weight polyethylene single crystals by differential scanning calorimetry. *Colloid and Polymer Science* 1985, *263* (10), 818-821. DOI: 10.1007/BF01412959.

(156) van Drongelen, M.; Cavallo, D.; Balzano, L.; Portale, G.; Vittorias, I.; Bras, W.; Alfonso, G. C.; Peters, G. Structure Development of Low-Density Polyethylenes During Film Blowing: A Real-Time Wide-Angle X-ray Diffraction Study. *Macromolecular Materials and Engineering* 2014, *299*. DOI: 10.1002/mame.201400161.

(157) Larsson, P. A.; Berglund, L. A.; Wågberg, L. Highly ductile fibres and sheets by core-shell structuring of the cellulose nanofibrils. *Cellulose* 2014, *21* (1), 323-333. DOI: 10.1007/s10570-013-0099-9.

(158) Larsson, P. A.; Gimåker, M.; Wågberg, L. The influence of periodate oxidation on the moisture sorptivity and dimensional stability of paper. *Cellulose* 2008, *15* (6), 837-847. DOI: 10.1007/s10570-008-9243-3.

(159) Jiang, J.; Liu, X.; Lian, M.; Pan, Y.; Chen, Q.; Liu, H.; Zheng, G.; Guo, Z.; Schubert, D. W.; Shen, C.; et al. Self-reinforcing and toughening isotactic polypropylene via melt sequential injection molding. *Polymer Testing* 2018, *67*, 183-189. DOI: https://doi.org/10.1016/j.polymertesting.2018.03.005.

(160) Zhou, M.; Li, X.-p.; Jin, M.; Xia, C.; Shen, K.-z.; Zhang, J. Simultaneously improving the tensile and impact properties of isotactic polypropylene with the cooperation of co-PP and β-nucleating agent through pressure vibration injection molding. *Chinese Journal of Polymer Science* 2016, *34*, 1001-1013. DOI: 10.1007/s10118-016-1814-4.

(161) Guo, H.; Rinaldi, R. G.; Broudin, M.; Tayakout, S.; Lame, O. Anisotropic deformation and failure behaviors of the necked HDPE materials induced by oligo-cyclic loading. *Polymer* 2021, *234*, 124232. DOI: https://doi.org/10.1016/j.polymer.2021.124232.

(162) Derakhshandeh, M.; Hatzikiriakos, S. G. Flow-induced crystallization of high-density polyethylene: the effects of shear and uniaxial extension. *Rheologica Acta* 2012, *51* (4), 315-327. DOI: 10.1007/s00397-011-0605-7.

(163) Zhang, X.-X.; Yang, S.-G.; Hua, W.-Q.; Lin, J.-M.; Lei, J.; Bian, F.-G.; Xu, L.; Li, Z.-M. Role of pressure in flow-induced shish-kabab in binary blend of long- and short-chain Polyethylenes. *POLYMER CRYSTALLIZATION* 2019, *2* (3), e10059. DOI: https://doi.org/10.1002/pcr2.10059.

(164) Janeschitz-Kriegl, H.; Ratajski, E.; Stadlbauer, M. Flow as an effective promotor of nucleation in polymer melts: a quantitative evaluation. *Rheologica Acta* 2003, *42* (4), 355-364. DOI: 10.1007/s00397-002-0247-x.

(165) Zhang, X.; Jacobsen, C.; Lindaas, S.; Williams, S. Exposure strategies for polymethyl methacrylate from in situ x-ray absorption near edge structure spectroscopy. *Journal of Vacuum Science & Technology B: Microelectronics and Nanometer Structures Processing, Measurement, and Phenomena* 1995, *13* (4), 1477-1483. DOI: 10.1116/1.588175 (accessed 3/3/2025).